Development of a Low-Pressure Ionization Chamber for Rare Isotope Experiments at IRIS

by

Patrick Fortier

A Thesis Submitted to
Saint Mary's University, Halifax, Nova Scotia
in Partial Fulfillment of the Requirements for
the Degree of Master of Science in Applied Science

August 28, Halifax, Nova Scotia

© Patrick Fortier, 2013

Approved: Dr. Rituparna Kanungo
Supervisor

Approved: Dr. Luigi Gallo
Committee Member

Approved: Dr. Adam Sarty
Committee Member

Approved: Dr. David Hornidge
External Examiner

Approved: Dr. Cristian Suteanu
Graduate Studies Representative

Date: August 28, 2013.

Acknowledgments

I send my sincerest thanks to my supervisor, Dr. Rituparna Kanungo, who taught me more than words can ever describe, from nuclear physics to more life lessons than I would care to count. I look forward to working with you in the future.

Many thanks to my distinguished committee members, Dr. Adam Sarty and Dr. Luigi Gallo, for their patience and collaboration in the completion of this work. Also to Dr. David Hornidge, for his help as my external examiner.

This project could not have been completed without the funding, office-space, and myriad of other aids from Saint Mary's University. For all their help, as well, I thank TRIUMF for the use of their facilities, servers, and everything else they had to offer (including the occasional free hamburger). I thank the entire IRIS group, whose contribution to my work has been vital to its completion, especially Alisher Sanetullaev, Grant Sheffer, Robert Openshaw, Reiner Kreuken, Greg Hackman, and Peter Gumplinger whose expertise and answers to my myriad of questions cannot go unnoticed.

I must thank my brother, Simon, whose guidance, wisdom, and levity was truly ineffable. And I owe a great to debt to my parents, whose support, love, and help financially, nutritionally, vehicularly, medically, and in so many other ways was invaluable.

Finally, I would be remiss if I did send my deepest thanks to Anneya (Broseph) Golob, who always had a couch, philosophical rhetoric, and advice; Diego, who offered me (poor) competition on late nights to keep my blood flowing; Moya, who sat by me even on the hottest days, always offering at the very least a pillow, and all my friends and family, who are too numerous to name here, who offered their help, advice, time, or just friendship throughout this whole experience.

Contents

List of Figures

List of Tables

Abstract

Development of a Low-Pressure Ionization Chamber for Rare Isotope Experiments at IRIS

by Patrick Fortier

The ISAC charged particle reaction spectroscopy station (IRIS), a new experimental facility at TRIUMF, is developed to study light and heavy proton- and neutron-rich nuclei. Due to the production processes of these nuclei, besides the nucleus of interest, contaminants with the same mass number may be present. To identify these contaminants, IRIS employs a low-pressure ionization chamber (IC), which tags the atomic number of the particles in the beam as they pass through the IC prior to interacting with the reaction target; a first in a low energy facility (<15A MeV). The IRIS IC uses a coplanar anode system with sixteen independent anodes. Its characteristics were studied and optimized throughout this work by using a pulser and ^{241}Am alpha source and two stable beams (^{18}O, ^{40}Ar). After parameter optimization, the results show that the IRIS IC has the capability to distinguish isobars at $Z = \pm 1$ for the beams studied.

August 28, 2013

Chapter 1

Introduction

Nuclear physics is a science driven by advancements in technology. Novel technologies can allow for higher precision measurements, which are indispensable to the discovery of previously unknown structures and features. The development and use of these technologies is integral to the advancement of science and we stand to learn a great deal from such investments. Current theories of the basic constituents of matter, and more specifically nucleon-nucleon interactions are largely empirical and can vary widely from one situation to another; no analytical solutions to these problems exist. This includes the formation and stability of nuclei, the structure and distribution of the nucleons within the nucleus, and most prominently, the interaction dynamics behind the strong nuclear force, the force necessary for protons and neutrons to bind to one another. Though two of the four fundamental forces are well understood, the forces governing the smallest parts of our universe are still under investigation. Much of nuclear physics is centered on understanding these forces and their fundamental interactions within matter. It is with innovative facilities at the forefront of technology that many new discoveries will likely come.

1.1 Scientific motivation

The discovery of quantum mechanics in the early twentieth century brought forth a revolution in our understanding of microscopic structures and laid the foundation of contemporary nuclear physics. Nuclear physics is the study of the structure and interactions of the elementary particles that constitute the nuclei that serve as the building blocks for all baryonic matter. It has been the subject of much focus and intrigue since Henri Becquerel discovered radioactivity in the late nineteenth century (Becquerel 1901). This is likely to do with its myriad of applications in various fields from power generation to medical imaging to weapons technology, and its vast complexity, especially at a fundamental level.

Though the dominant force behind nucleon-nucleon interactions is the strong force, both the weak force and electromagnetism contribute as well. Gravity is too weak to have an effect on nuclear interactions, except in the case of nucleosynthesis where it supplies much of the thermal energy necessary to generate nuclear fusion in the core of stars. It is interesting to note that the strong force between nucleons is a remnant of the force that binds quarks together, similar to how the Van der Waals force is a remnant of Coulombic force in atoms. This implies that the force binding nucleons to one another is rather weak compared to that which binds the quarks within nucleons (Casten & Sherrill 2000).

A considerable amount of both theoretical and experimental work has gone into studying these issues. The early work in the field of nuclear physics conducted in the former half of the twentieth century were the scattering experiments performed by Ernest Rutherford. In these experiments Rutherford accelerated α-particles at a gold foil and observed their scattering cross section (Rutherford 1911). Today, this is known rather aptly as Rutherford scattering. Continued work on scattering cross sections has contributed to much of our knowledge of nuclei and their constituent nucleons. Theoretical models of the nuclear interaction potential have been compared with experimental data in order to

understand the behaviour of the forces between nucleons. Despite many decades of work, however, physicists have yet to define an analytic form for the strong force as they have done for both gravitation and electrodynamics. Whether or not a form of that nature even exists is still an unanswered question. It is with this in mind that many aspects of contemporary nuclear physics focus on finding how nucleons interact with one another in order to better describe and gain more complete understanding of the interaction potential of the strong force and building its connection to quantum chromodynamics, the theory responsible for describing the interaction of the quarks and gluons within hadrons. This often requires looking beyond stable nuclei to the extremes of nuclear existence and "exotic nuclei". Many of the current generation of particle accelerator facilities are dedicated to exploring the properties of these exotic nuclei, as they offer a promising outlook towards the complete discovery of the nature of the strong force.

One of the most interesting properties that bears the signature of the strong force is nuclear shell structure, which has puzzled researchers since it was discovered. Analogous to the electrons in an atom, nucleons within the atomic nucleus have been shown to exhibit a shell structure, wherein nucleons tend to arrange themselves into distinct, quantized energy levels. The idea of nucleons in orbital shells is a purely quantum idea and has no classical analogue, thus the shell model was not always believed to be true; for more information on the models preceding the shell model, such as the liquid drop model, most introductory nuclear physics textbooks provide reasonable summaries. Please refer to Dunlap (2004) for a qualitative overview or Heyde (2004) for a more in depth mathematical treatise of the nuclear shell model. Nuclear shell gaps (the amount of nucleons within a particular shell) are referred to as magic numbers, as the most stable nuclei consist of a "magic number" of nucleons (in both protons and neutrons). Interestingly, these magic numbers are seen in the arrangement of both electrons and nucleons.

Magic numbers, however are not as straightforward as one would hope, as there is evidence of magic number shifts when nuclei are very neutron- or proton-rich with respect to their stable isobars and isotopes (Kanungo 2004; Tanihata 1996, 2001; Casten & Sherrill 2000). Magic numbers are not the only mystery in nuclear physics that could lead to a greater understanding of fundamental nuclear structure, however. In general, nuclei far from stability, known as exotic nuclei (section 1.2), have presented several puzzling features that many scientists are currently trying to understand. Also, as these exotic nuclei are key not only to our understanding of nucleosynthesis and various fields of nuclear astrophysics, but to our overall understanding of nuclear structure, they have become increasingly pertinent in the nuclear science conducted today.

1.2   Exotic nuclei

In studying the limits of nuclear stability one is able to more clearly examine how the nuclear force acts. Nuclei at or near the edge of stability, called the drip line, the point at which an added nucleon will simply "drip" out from a nucleus, give the unique opportunity of studying how nucleons arrange themselves within the nucleus and at what point and why they enter their drip line. This concept is analogous to performing stress tests on the structure of a building, as one must be aware of how the materials react in all conditions in order to fully understand their behaviour. Casten & Sherrill (2000) define exotic nuclei in one of three ways: a nucleus that has one or more neutrons or protons than its known stable isotope, which is essentially a nucleus with an extreme ratio of neutrons to protons (N/Z) with respect to its stable counterparts; a nucleus that exhibits radioactive features not found in its stable counterparts; a nucleus that has a short half life but is important due to its astrophysical significance. Using the chart of nuclides, which is the nuclear physicist's
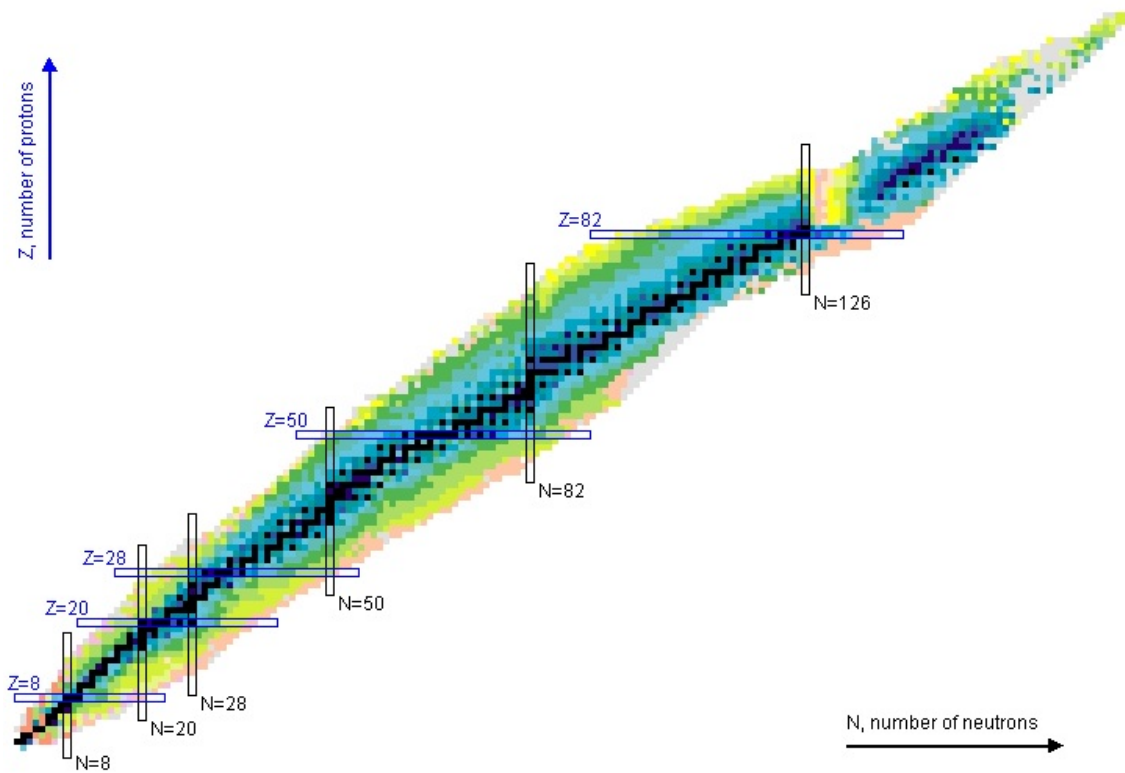
Figure 1.1: The chart of nuclides (Alejandro Sonzogni 2013). Shown on the abscissa is the number of protons (Z) in a particular nucleus, while the ordinate shows the number of neutrons (N). The different colours of each cell indicate the type of decay that nucleus undergoes. The cells under the labels $N = x$ and $Z = y$ show the locations of proton and neutron magic numbers, respectively. Image courtesy of Brookhaven National Laboratory.

analogue to the periodic table of elements, shown in figure 1.1, one can see how few stable nuclei exist (shown in black) as compared to unstable (other colours).

As can be deduced from their often extremely short half-lives, exotic nuclei, except in the cases of certain astrophysical phenomena, are very rarely found in nature, and certainly not in the quantities necessary for experiment. The exotic nuclei used for study must be created by accelerated beams from reactions on stable nuclei. These nuclei are generally produced by means of compound nucleus or spallation reactions for proton-rich nuclei and fragmentation of heavy-ion beams for neutron-rich nuclei (Sherrill & Morrissey 2004;

Veselsky & Souliotis 2011). Moreover, though proton-rich nuclei have been studied fairly in depth for some time, neutron-rich nuclei have not seen the same treatment and we only have knowledge of the neutron drip line up to isotopes of oxygen (Casten & Sherrill 2000; Veselsky & Souliotis 2011), which ends at ^{24}O (Kanungo et al. 2009). Interestingly, this is theoretically predicted, as is shown by Hagen et al. (2012). This lack of understanding leaves room for a wide variety of experimentation and as technology progresses it is becoming easier to create beams of these neutron- and proton-rich nuclei, which will allow nuclear physicists to probe highly exotic nuclear structures like neutron skins and halos, which occur at the bounds of β-stability and of which very little is currently understood. For more information on neutron halos and skins, some of the most interesting exotic nuclei, please refer to *et alia* Bazin et al. (1998); Casten & Sherrill (2000); Dobrovolsky et al. (2006); Kanungo (2004); Tanihata (1996); Tanihata et al. (1985); Lagoyannis et al. (2001).

1.3 Ionization chambers

One of the challenging aspects to overcome in nuclear physics is the ability to observe the particles one wishes to study. This difficulty comes largely from the size of nuclei, which are on the order of 10^{-15} m, putting them well beyond the observational limits of even the most advanced electron and atomic force microscopes. Therefore, the only way to "see" these particles is through the energy signatures they leave behind in radiation detectors. Every radiation detector works on the simple principle that a quantum of radiation passing through it will deposit some or all of its energy within the detector, thus allowing one to observe the deposited radiation by means of the subsequent generation of an electronic signal. Though many types of these detectors exist, this thesis will focus on ionization chambers, as they provide the central subject on which it is based.

In principle, ionization chambers are some of the simplest radiation detectors still in use today, especially when compared to the advanced semiconductor and scintillator detectors available. The ionization chamber, hereafter IC, works off the basic principle of atomic ionization. In the simplest terms, an IC is just a positively charged anode and a negatively charged cathode, which create an electric field within a chamber filled with a gas that is capable of being easily ionized. Thus when a quantum of radiation enters the IC and ionizes the gas to create an ion pair, due the electric field in the gas, the positively charged ion drifts to the cathode, while the negatively charged electron drifts to the anode. This creates a signal, which is then sent out from the IC to electronics to then be processed (Rossi & Staub 1949; Wilkinson 1950; Price & Price 1964).

There are many factors that go into ionization chambers and the classification of their characteristics. An excellent resource for this is Knoll (2010). The specific type of IC used for this work is detailed in section 2.3. Theoretically, they can be quite complex despite their inherently simple design. The goal of this project is to characterize and optimize an IC used for the purpose of high precision particle identification with a low-energy beam before it strikes a target. This IC has been designed with the purpose of being able to isobarically filter beams to a resolution of $Z = \pm 1$ in order to allow for studies on heavy exotic nuclei that have never before been possible. Chapter 2 outlines the IRIS facility with an especially detailed description of the ionization chamber. Chapter 3 details the experiments that were used in this study of the ionization chamber including alpha source tests and the use of stable beams. Chapter 4 explicitly describes the methods and procedures of analysis using the data from these experiments and their subsequent results.

Chapter 2

IRIS

The ISAC chaRged partIcle reaction Spectroscopy station (IRIS) has been designed to study direct reactions with rare isotope beams (for information on direct reactions, please refer to Satchler (1983)). The IRIS facility was officially commissioned in 2012 as part of the ISAC II experimental hall at TRIUMF. Its main scientific goals involve probing the structure and excitation of exotic neutron- and proton-rich nuclei. IRIS' predicted ability to do so is aided, in part, by its multi-sampling ionization chamber, which is located upstream from the target and is used for isobaric separation, as well as its unique target system. The target itself is novel in the sense that it is a solid pure hydrogen. This specialized target will be used mainly to study $^{A}X(p,d)^{A-1}X$ and $^{A}X(d,p)^{A+1}X$ reactions as well as inelastic collisions (p,p'), two neutron transfer (p,t), and proton transfer reactions (d, ^{3}He). This will be done mainly with exotic beams of energies $\geq 5A$ MeV. Using the ionization chamber for isobaric filtering, IRIS will be able to study heavy exotic neutron-rich nuclei, such as unstable isotopes of Sn and Ca. Figure 2.1 shows a computer rendering of the IRIS beam line which includes the scattering chamber that houses the target and main detector arrays, as well as the ionization chamber, which sits slightly upstream.
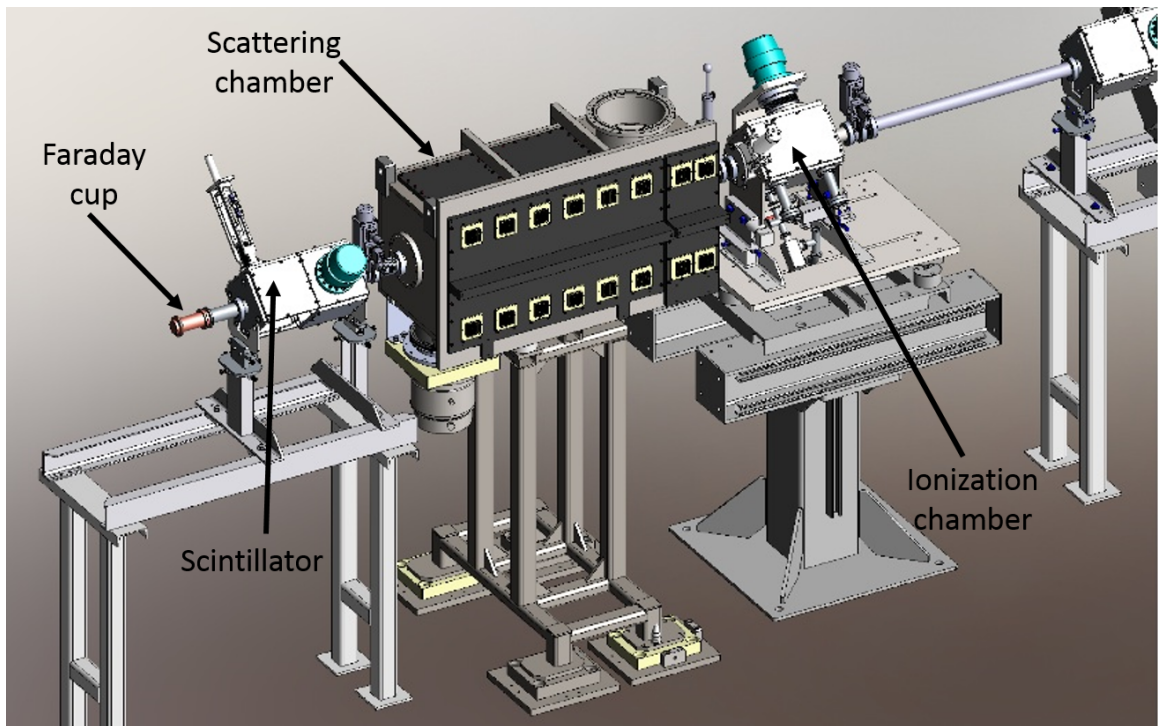
Figure 2.1: A computer rendering of the IRIS beam line. From left to right one can see the Faraday cup and scintillator detector (used as a beam dump and for detecting the beam after it passes through the solid hydrogen target and silver foil, respectively), the scattering chamber, which houses the solid hydrogen target and main detector arrays, and the ionization chamber, used for isobaric filtering of the beam.

IRIS has a breadth of scientific goals, the motivation behind which is similar to those listed in section 1.1. These are mainly to address fundamental changes in nuclear structure as well as the synthesis of new elements using nucleon transfer reactions. Through these transfer reactions, IRIS will be able to measure the spin, angular distributions of outgoing particles, l values of nuclear orbitals (the magnitude of the angular momentum), the effects of excess neutrons on nuclear structure, and low lying dipole resonances in proton and neutron-rich nuclei, especially those with neutron skins and halos. All of this will help to explore nuclei of astrophysical significance and the theories behind fundamental nucleon interactions, while contributing to our knowledge of shell closures and magic number shifts. Figure 2.2 shows a picture of the IRIS beam line.

2.1 Detector array

IRIS employs a YY1 silicon strip detector array, which uses silicon strip detectors, as shown in figure 2.3 (see appendix B for a full list of acronyms and terms). An annular array of cesium-iodide scintillator plates in conjunction with an annular array of the silicon strip detectors, which are shown in figure 2.3, form the $E - \Delta E$ detector, wherein the particles pass through the silicon detectors depositing a portion of their energy (ΔE) and then stop in the CsI detector (E), which lies slightly downstream. There is also room for a second annular array of silicon strip detectors upstream from the target for back scattering. The radial setup of these detectors allows one to reconstruct the Q-value spectrum from the scattering angle and energy distributions and provides kinematic loci necessary for identifying changes in nuclear structure.

A fourth silicon detector array, the S3 detector, is placed farther downstream from the target than the $E - \Delta E$ array. While the $E - \Delta E$ array is used to detect and measure the
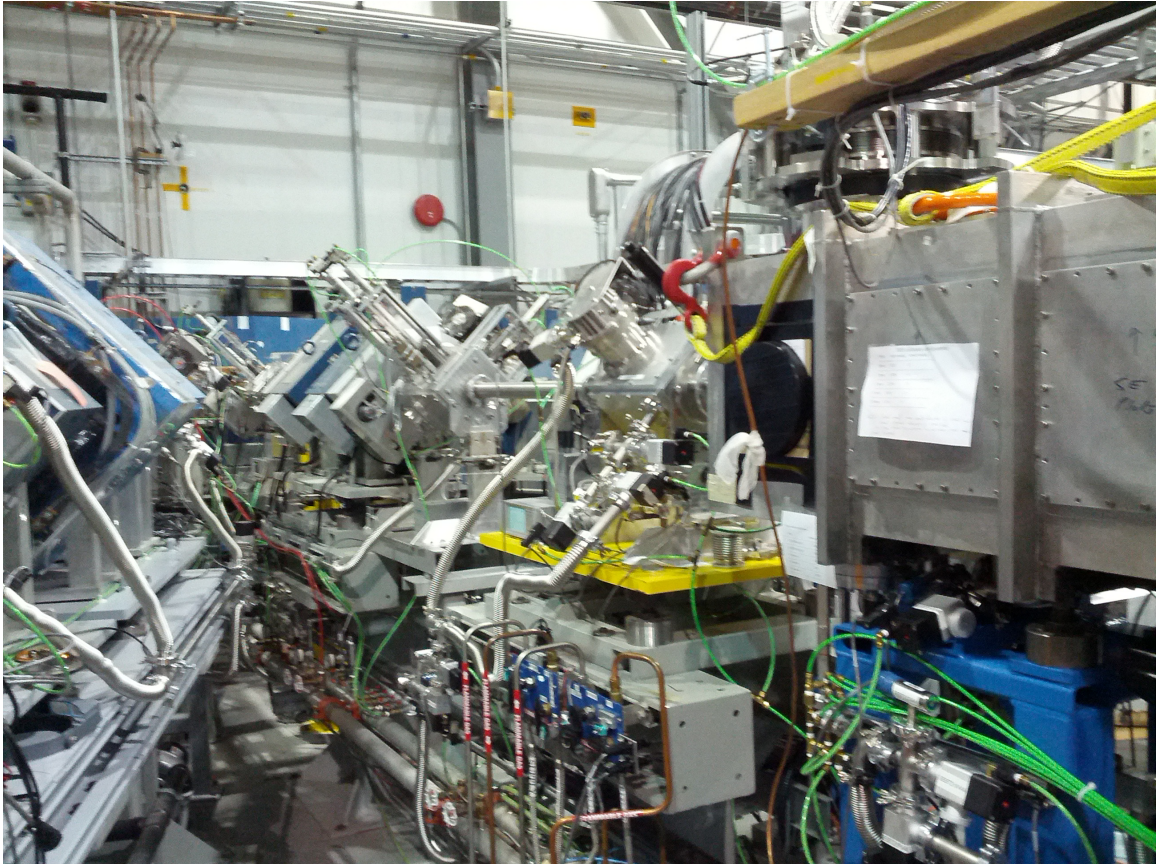
Figure 2.2: A view looking down the IRIS beam line. In the foreground on the right is the scattering chamber, which houses the detector arrays and the solid hydrogen target, followed by the ionization chamber. In the background, one can see the dipole magnets, which are used to alter the position of the beam by making fine adjustments to its trajectory.
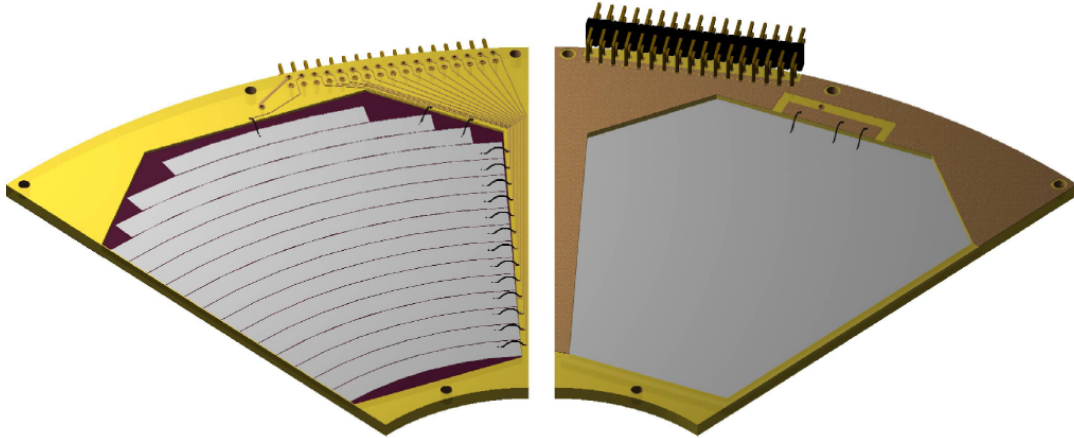
Figure 2.3: A rendering of the silicon strip detectors, which are part of the YY1 annular detector array. Eight of these together complete and circle and subsequently constitute the ΔE portion of the $E - \Delta E$ detector. The image on the left is the front of the detector (the face hit by the particle), whereas the image on the right is the back. They are segmented into rings to allow for accurate ϕ distributions to be measured. Each sector allows for measurements in θ.

light, highly scattered particles in the predominantly (p,d) and (d,p) reactions (the protons and deuterons), the S3 detector is placed so as to interact with the heavy reaction products, which are unlikely to deviate by a large θ. The S3 is a singular annulus (as opposed to eight separate pieces) split into sector and rings. A rendering showing the complete detector array in the scattering chamber is shown in figure 2.4.

2.2 Solid hydrogen target

IRIS employs a novel target system by using a cryogenically cooled, solid hydrogen target (SHT). This system, as opposed to other solid targets containing hydrogen, which generally involve polymer foils and solid hydrocarbons, allows for the high reaction rates of a solid target while filtering out unwanted reaction channels attributed to the molecular targets' non-hydrogen constituents such as carbon and oxygen. Though the density of the
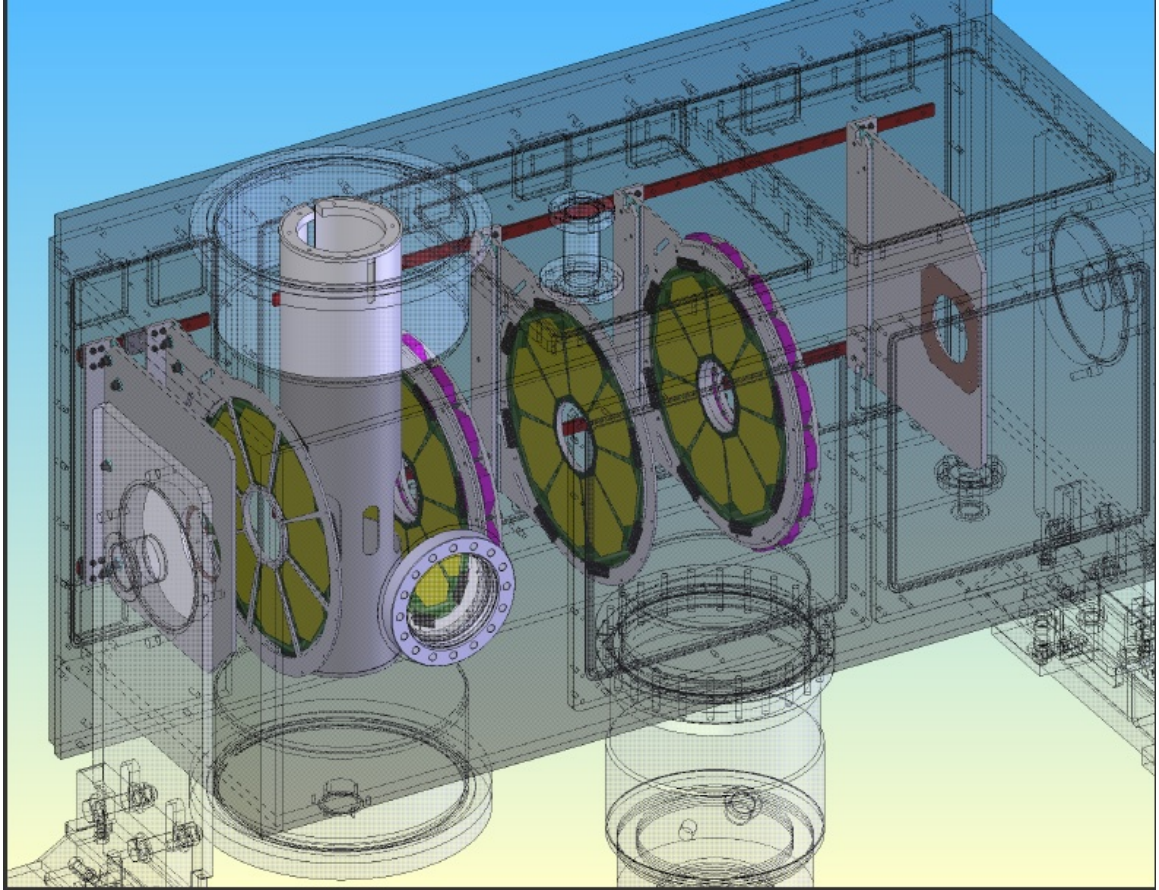
Figure 2.4: All four detectors are displayed in this computer rendering of the IRIS scattering chamber. On the left side of the image is the upstream silicon strip detector. The large cylinder to its right is the solid hydrogen target housing (see section 2.2), followed by the YY1 and CsI $E - \Delta E$ array, and finally the S3 detector for heavy reaction products.

SHT is 0.086 g/cm^3 and the density of solid CH$_2$is 0.89 g/cm^3, excluding the reactions off carbon is important enough to make the SHT a worthwhile investment. A gaseous hydrogen target at 10 atm, on the other hand, has a density of 0.0008988 g/cm^3, which is significantly less. This is especially important when dealing with the low intensity beams that are often associated with highly exotic nuclei. As the main focus of IRIS is to study (d,p) and (p,d) reactions, the SHT is ideal.

The SHT is formed by condensing gaseous, pure hydrogen onto a thin silver foil (roughly 5 μm) cooled to 4 K. Silver is used for its thermal properties and the fact that the energy loss and energy straggling from the reactions in the foil do not greatly affect the physical goals IRIS is hoping to achieve by the use of the SHT itself. The SHT is thin ($<$ 100 μm) and can be formed from deuterium or hydrogen. The SHT, along with the IRIS ionization chamber make IRIS a unique, world class facility, employing novel, never-before-used technologies for the progress of its scientific goals.

2.3   IRIS ionization chamber

Due to the nature of their creation process, which are described in section 1.2, heavy radioactive ion beams often carry contaminants. These contaminants can be prevalent enough as to comprise up to 90% of the nuclei within the particle beam and can make identifying the proper reaction channel difficult. The purpose of the IRIS ionization chamber (IC) is thus to detect the Z values of the constituent particles within the beam before it reaches the target in order to determine the beam contaminants so that one can filter out the unwanted reaction channels. Under optimal operating conditions it is theorized that the IC may be able to detect differences in nuclei of $Z = \pm 1$, which can often encompass many of the contaminants in a particle beam due to the nature of the spallation
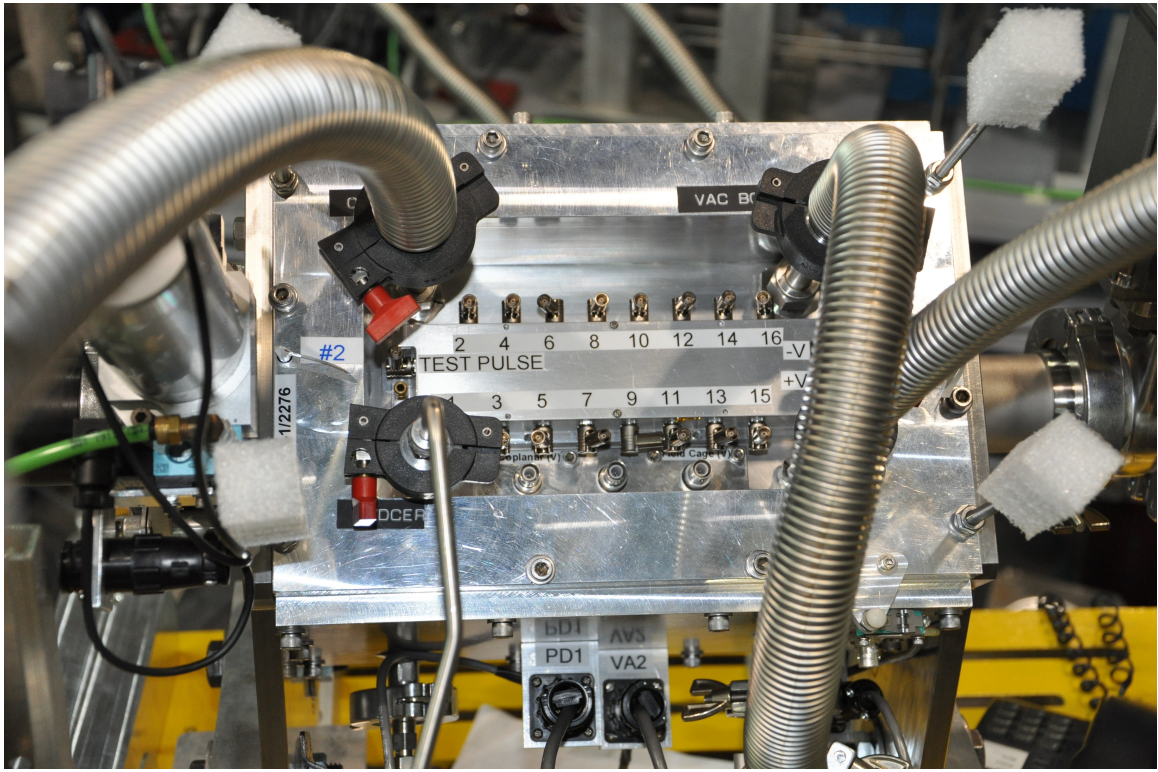
Figure 2.5: The IC installed in the IRIS beam line. Here, it is sitting upstream from the scattering chamber so that the beam first passes through the IC before hitting the target. The large pipes connected to the chamber box are for gas flow (section 2.3.5) and the numbered connectors each refer to a single preamplifier output, whereupon each preamplifier is connected to an individual anode (see section 2.3.1 for an in depth explanation).

and fragmentation techniques used to create these heavy, radioactive ion beams. Referring to figure 2.1, one can see that the IC is placed upstream from the scattering chamber in order to sample and collect information from the beam before reaching the target. Figure 2.5 shows the IC as it sits in the beam line, whereas figure 2.6 shows the exterior of the chamber itself, attached to its flange, prior to installation.

Though ionization chambers with a similar purpose of isobaric tagging exist in some high energy facilities, the design challenges of the IRIS IC are in the sense that the beam energies in the ISAC facility are orders of magnitude lower than what would be found in
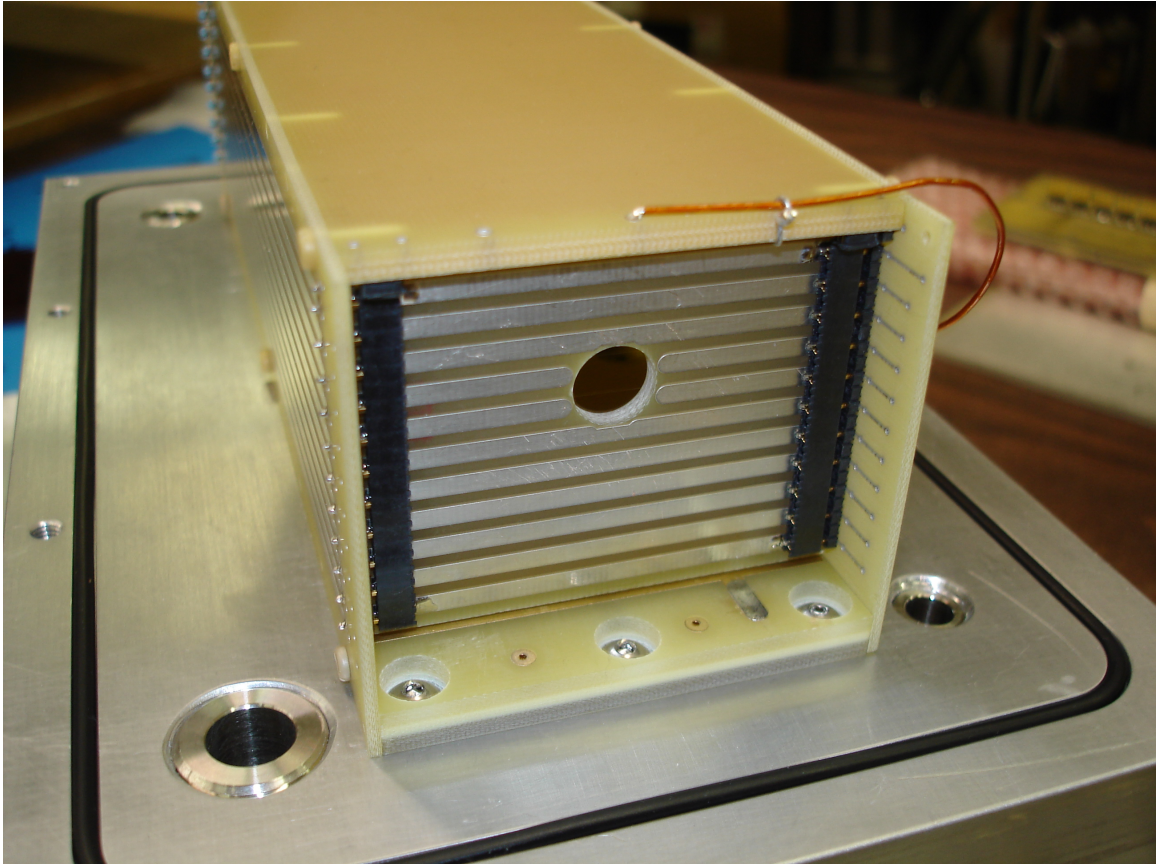
Figure 2.6: The exterior of the IRIS ionization chamber mounted to its diagnostic box flange before installation. The hole in the center of the chamber is for the entrance window (there is thus another hole on the opposing side of the chamber for the exit window) and the metal strips running along the IC make up the field cage (section 2.3.4.1).

a typical high energy accelerator. Thus it must identify nuclei with similar Z values while extracting a minimal amount of energy from the particle beam so as not to interfere with the physics at the SHT. In the following sections, the design and operating parameters will be explored, explaining how this is possible.

2.3.1 Overview

The design of the IC can be broken down into six major elements: the coplanar anode, the field cage, the multi-sampling anode pads, the entrance and exit windows and the low pressure design of the box itself, the fill gas and gas flow system, and the electronics. The design of the chamber itself is fairly simple; it is a rectangular prism measuring 195 mm $\times$ 62 mm, by length and width, respectively. The chamber is constructed from a G10 plate with various metals used for the field cage, cathode, anode pads, and coplanar anode, all of which will be detailed in the following sections. Mounted in line with the anode pads, the 6 mm annuli cut out on either side of the chamber house the entrance and exit windows, which sit above the anode strip that lies along the floor of the chamber. Figure 2.7 (Sheffer 2013) shows a schematic diagram of the inside of the IC from a top view perspective, while figure 2.8 shows a rendering of the IC installed in its diagnostic box flange. Both these figures outline key components of the IC as well as its dimensions and shape.

2.3.2 Low pressure design

As the IRIS IC is dealing with fairly low energy particles, it is crucial to minimize energy losses by particles traversing the IC so that the physics at the SHT is not changed. The energy loss within the IC is thus of great concern. A typical, lighter ion that passes through the chamber may have less than 100 MeV of total kinetic energy and in the case of the offline testing with alpha particles there may be only 4 or 5 MeV of total kinetic energy
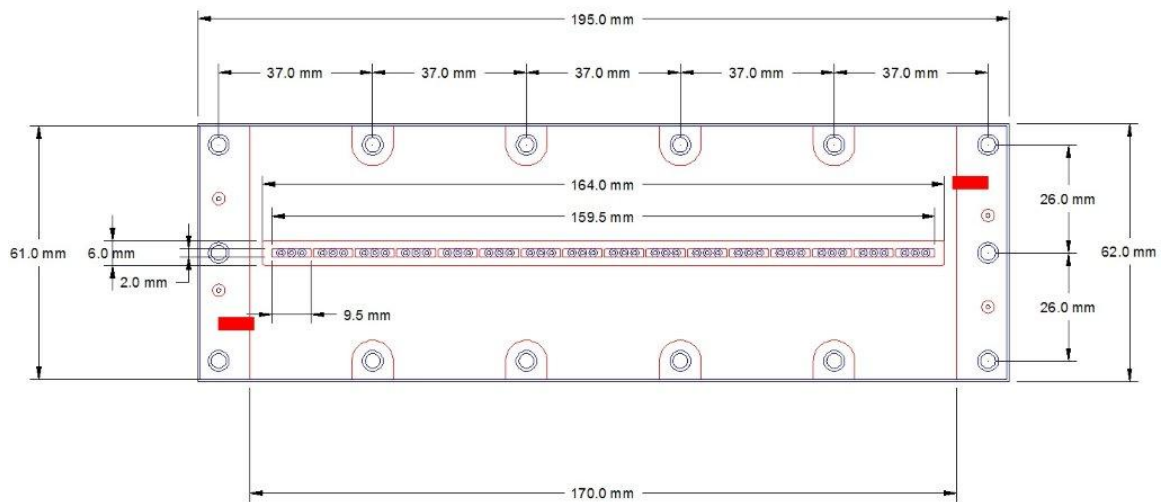
Figure 2.7: A schematic of the IRIS IC, created by its chief designer Grant Sheffer, showing the dimensions of the chamber and its associated components, drawn from a top view perspective. The most important dimensions to note, beyond the size of the chamber itself, are the distance from the edge of the chamber to the first and last anodes (30 mm) and the length of the anode strip (164 mm), which contains the 16 individual anode pads, as these have the largest effect on the operation of the IC (Sheffer 2013).

Diagnostic Box Flange

Low Pressure Gas Box

IC Readout Pad

IC Field Cage

Gas Inlet Manifold

Silicon Nitride Window

Electrical Insulator Gasket
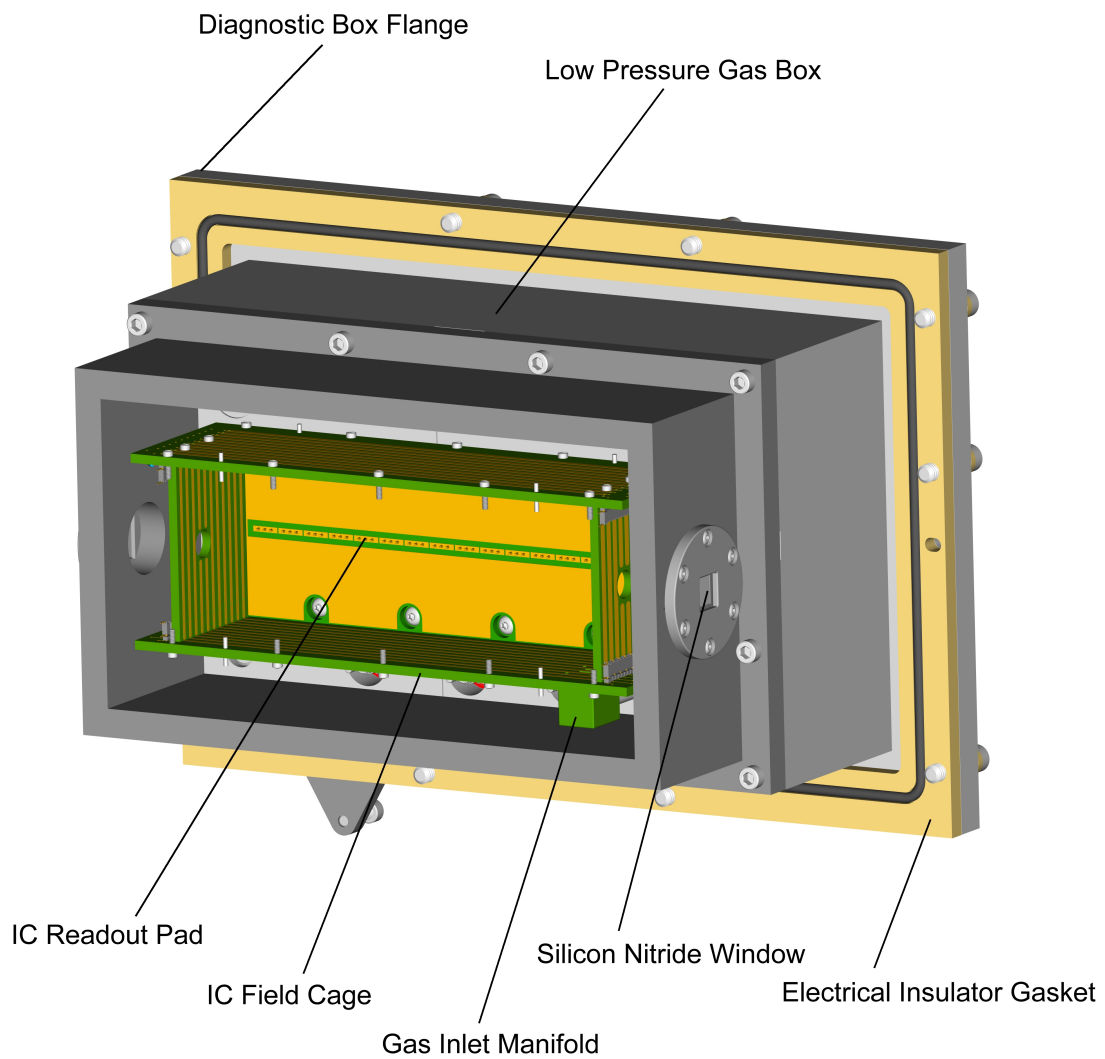
Figure 2.8: A computer rendering of the IRIS IC attached the to diagnostic box flange, created by its chief designer Grant Sheffer. Labeled are the main components of the IC (Sheffer 2013).

available. This means that in order for an ion to pass through the chamber with minimal energy loss, so that it can strike the target largely undisturbed, the IC has to operate by collecting, in extreme cases, only about 1 MeV across its entirety. The main concern for this is, of course, that the fill gas must be maintained at a low pressure while still allowing for a signal to noise ratio high enough to determine individual events and make the necessary measurements within the chamber.

This brought upon several challenges: the entrance and exit windows had to be extremely thin and not particularly dense while maintaining their integrity at low pressures, and that the typical gas pressure inside the chamber was to be on the order of 20 Torr, which requires several intricate systems in place, described in the following sections (in practical operation, the IC has been used with gas pressures of 10 Torr and 19.5 Torr). The flow gas chosen is isobutane for its ionization properties and the windows in use are either the ultra-thin silicon-nitride (Si_3Ni_4) windows at 30 nm or 50 nm, or the thicker and more durable Mylar windows at 900 nm. In the experiments detailed below, the Mylar windows were chosen for their durability as the Si_3Ni_4 would break under pressure spikes in the gas flow system. The Si_3Ni_4 windows, however, are rated to take pressures at up to 25 Torr, while the Mylar windows can withstand more than twice that amount. These pressure spikes have since been fixed and thus in future experiments it is likely that Si_3Ni_4 windows will be used, as they significantly reduce the energy loss in the incoming particle beam (with a 10*A* MeV beam of ^{40}Ar, for example, 1.51 MeV is lost in the 900 nm Mylar entrance window, while only 0.18 MeV is lost in the 50 nm Si_3Ni_4; a difference of nearly 840%).

2.3.3 Multi-anode configuration

As well as using extremely low gas pressures, the IRIS IC has also been designed to have a multi-sampling anode system of 16 independent anode pads that form an anode

strip across the center of the chamber along the axis of the beam travel (refer to figures 2.7 and 2.8). Each of the 16 anodes are 9.5 mm long and separated by a 0.5 mm gap. This has been implemented for various reasons: to reduce pile-up, to allow one to observe possible unwanted nuclear reactions taking place within the chamber, to allow for simple measurements of the relative energy loss across the chamber for a given ion, and to allow one to vary the number of anodes across the chamber by coupling any number of the anodes together. The last of which has been done in order to increase or decrease the signal output of a given preamplifier, depending on the charge of the incident radiation and the gas pressure. Therefore, though the anodes are technically independent, they are capable of being physically coupled together in order to make any combination of the 16 anodes available. The anodes are coupled together via jumpers which physically attach two anodes together by conducting wire, creating a single, larger anode consisting of the smaller anode pads, which is then connected to a single preamplifier for signal processing. The IC will be typically set to the maximum number of anodes that will still give a distinguishable signal to noise ratio, as in post processing this allows for the largest signal when the anode signals are added event-by-event. Figure 2.9 is a diagram of the anodes within the IC and their numerical labels, which will be used to reference the various sections of the IC.

Coupling the anodes together is a simple process that can be performed *in situ*, meaning that the IC does not need to be removed from the beam line while these changes are made. Figure 2.10 shows the part of the IC that can be removed in order to change the anode configuration. Once any number of anodes are coupled together, only a single preamplifier is connected to that set of anodes to process the signal. Thus each preamp receives a signal of a single anode multiplied by how many anodes are coupled together and attached to that particular preamp. This is very useful for the IRIS IC, as there are explicit restrictions as to how much energy can be taken from the the particle beam in order to avoid effecting the
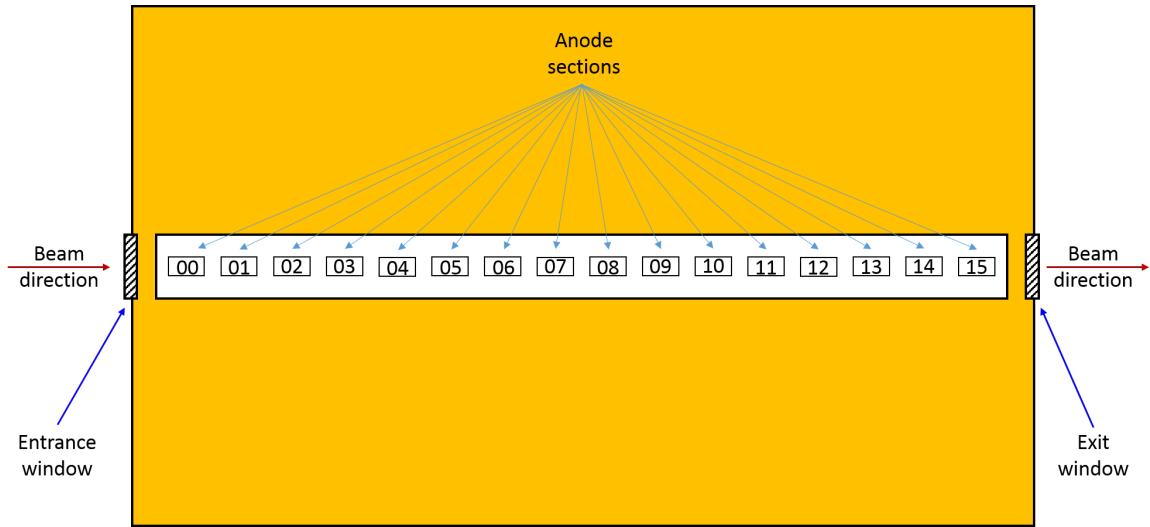
Figure 2.9: A simple diagram showing the 16 anodes in the IC and their numerical labels, which will be referenced throughout.

physics downstream. Thus, when using light nuclei in the incident particle beam one can simply couple more anodes together and maintain the multi-sampling system but increase the signal by as much as eight times. The signal output given by a particular preamplifier should change proportionally to how many anodes are coupled together. By coupling two anodes together, for example, the single anode they produce is collecting the charge of the two anodes but only sending to a single preamplifier. It should be noted that the IC is generally configured symmetrically, unlike what is shown in the example in figure 2.10, so that the signals across all anodes from any given event can be easily added and compared to one another.

2.3.4 Coplanar anode design

Typically, in ionization chambers of this nature, a Frisch grid (Frisch 1944) design is implemented in order to help collection of the ionized electrons. This is due to the dependence on both the position at which the ions are created within the chamber and
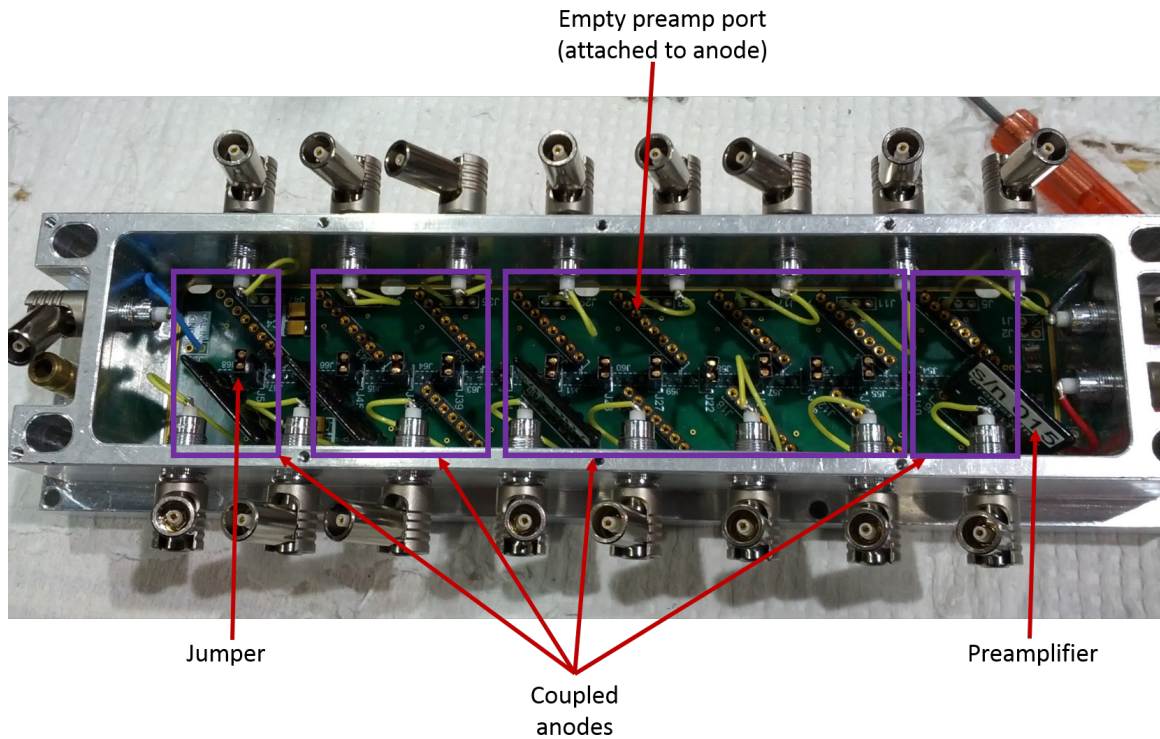
Figure 2.10: The part of the IC that can be removed in order to change the anode configuration. The black jumpers, which are placed on the pins in between the preamplifier slots, are used to physically connect one anode to another. This, in essence, creates a single, larger anode. Each of these large anodes then has a single preamplifier connected to it. In this image, from left to right, there are two pairs of two anodes coupled together, followed by four anodes coupled together, and finally the last eight anodes are connected via the jumpers. As only one preamplifier is needed for each anode, there are only four preamplifiers in this setup.

the pulse amplitude in standard electron sensitive ion chambers. An IC works on the basic principle that as a particle passes through the chamber, it ionizes atoms in the fill-gas, which are then collected by the anode and cathode to produce a signal. As a simple IC consists of only an anode and cathode, this can become a problem in a high rate situation or if the position of the particle beam is slightly offset, among other things. Given the potential difference between the anode and the cathode, the negatively charged electrons naturally drift toward the positively charged anode and the positively charged ions drift toward the negatively charged cathode. Without an added component to aid in electron drift, it is easy to see that these basic ion chambers can be highly sensitive to the position of the beam as well as the amount and rate of ionization in the chamber that produces the signal.

A solution to this problem is to add what is known as a Frisch grid. A Frisch grid's purpose is to mitigate the position dependence of the pulse amplitude by adding a charged grid between the anode and the cathode. This grid is held at an intermediate potential between the anode and the cathode such that the electrons are attracted to it. In order to properly function it must be transparent to electrons, however, as they must pass through the grid on their path towards the anode. Figure 2.11 (Knoll 2010) shows simple circuit diagram detailing the implementation of Frisch grid system in a basic IC. In simplest terms, when a particle enters the chamber and ionizes atoms in the fill-gas, the corresponding ionized electrons, which are responsible for producing the signal, begin to accelerate towards the Frisch grid. Once they reach the grid, however, they experience the stronger positive potential from the anode, which is used to collect the electrons and produces the initial, measurable signal. The electrons then drift through the electron transparent Frisch grid to be collected at the anode. For more information on Frisch grids, please refer to *et alia* Frisch (1944).

One downside of Frisch grids, however, is that they are susceptible to small vibrations
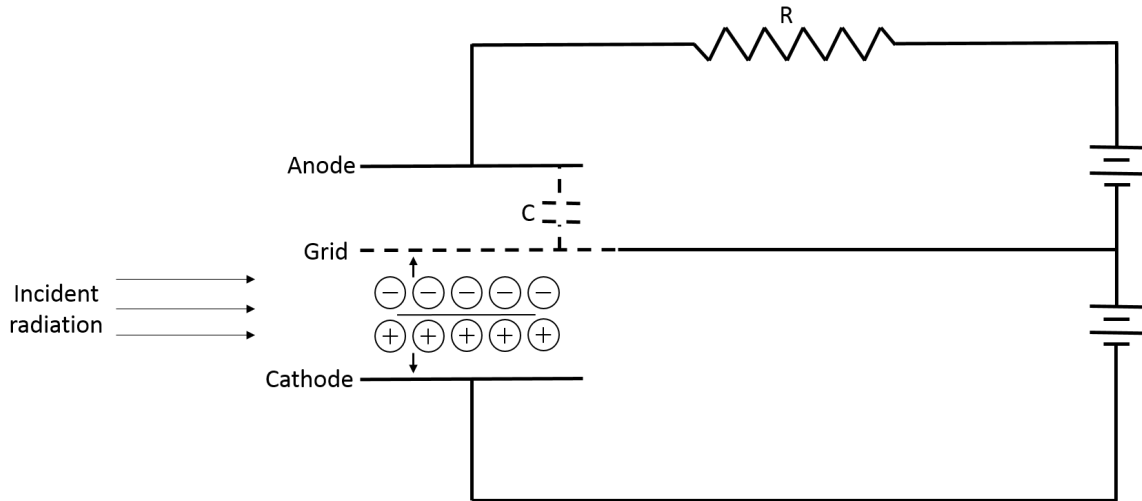
Figure 2.11: A circuit diagram of a basic Frisch grid. The incident radiation ionizes atoms which are then split into negatively charged electrons and their corresponding positively charged ions. The electrons first accelerate towards the positively charged Frisch grid, before passing through it and continuing to accelerate towards the more positive anode wherein they are collected to produce an electrical signal. This diagram is based off a figure found in Knoll (2010).

which could impede the charge collection process. These vibrations are known as microphonics and they can, when dealing with extremely small signals, effect the performance of the IC. These microphonics can be produced by nearly anything, including the gas flow systems inherent to the operation of the IC. Because of the low pressure, small pulse amplitude design of the IRIS IC, a Frisch grid may produce issues with the signal collection process. In order to mitigate the possibility of this issue, the IRIS IC was designed without a Frisch grid. In order to compensate for this, it instead uses a similar system designed to accentuate the benefits provided by a Frisch grid while eliminating its potential problems. This system uses a coplanar anode, which focuses electrons onto an anode strip located in the center of the chamber, and a field cage to increase their drift velocity toward it, similar to a Frisch grid. This coplanar design, as it uses solid metal plates attached to the chamber and not a fragile, electron-transparent grid, is not sensitive

to microphonics as a Frisch grid may be and is thus ideal for the purposes of the IRIS IC.

It should be noted, however, that the coplanar anode design only works well in the IRIS system because the ISOL beam characteristics are such that the beam has very small size and angle while passing through the ionization chamber. Due to this, the anode strips can be quite narrow in the transverse direction to the zero degree beam axis, covering the entire path of the beam. Were radiations to traverse the entirety of the chamber, ionization would take place throughout the the volume of the IC and the coplanar anode would not be capable of focusing them onto the anode pads correctly. This principle will be explained in greater detail in the following sections.

The two main components of this system, the field cage (detailed in section 2.3.4.1), and the coplanar anode (detailed in section 2.3.4.2) are fairly simple in design, with the purpose of the field cage being to facilitate the transverse diffusion of the electrons as they drift to toward the anode pads by means of an electric field gradient, and the coplanar anode being to create a focal electric field that concentrates the electrons onto the central anode strip. Each of these components has a separate voltage source and can thus be controlled independently in order to optimize ratio of field cage bias to coplanar bias voltage (see section 4.6) for a given circumstance.

2.3.4.1   Field cage

The field cage (FC), is a negatively charged cage made up of metal strips that run around the perimeter of the chamber. Its purpose is to create an electric field gradient within the IC that accelerates the ionized electrons in the direction of the anode strip. The field cage works by using 11 segmented metallic strips which run from the cathode to the coplanar anode (see figure 2.12). An initial negative potential difference is applied to the cathode, and through a series of resistors the voltage is fed through each subsequent level of the field
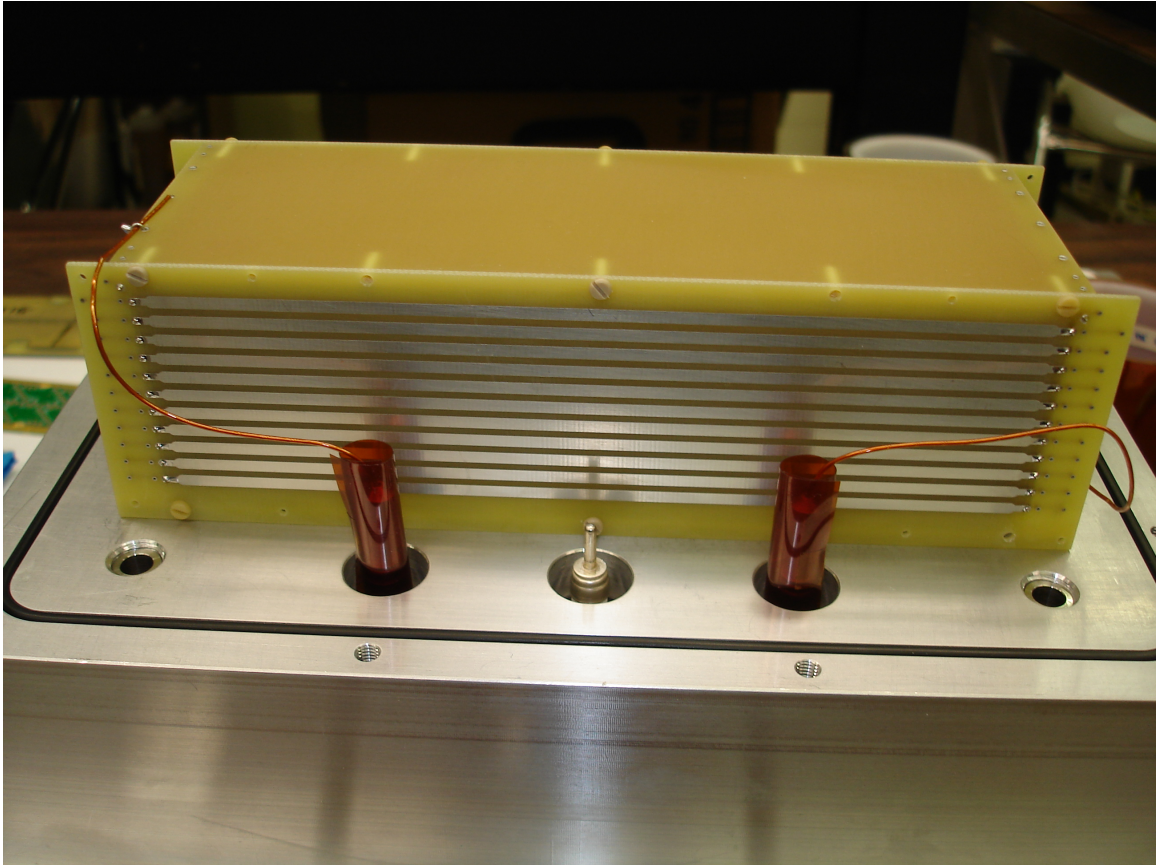
Figure 2.12: Each of the eleven metal strips, which are separated by a resistor, seen on the chamber, combine to make up the field cage. The copper wires on either end of the IC are the independent voltage supplies for the field cage and coplanar anode. The purpose of the field cage is to create a graduated drift field more negatively than the anode itself to accelerate the electrons toward the anode strip.

cage. This creates an electric field gradient with decreasingly negative potential throughout the chamber. The electrons then follow the electric field lines created by the field cage downward toward the anode strip.

The electric field gradient created by the field cage is a very effective way of moving the electrons in the direction of the anode strip. Figure 2.13 is a schematic circuit diagram showing a basic field cage design. As one can see, however, the field cage only moves the electrons in the right direction. The field cage alone does not have the ability to force

electrons onto the anode strip, and thus were it only for the field cage, the signal at the anodes from any given quanta of radiation would be considerably reduced, especially in the event of an offset beam. Even though the beam is positioned directly over the anode pads, ionization can take place outside the area directly above the anode strip. This can be caused by numerous factors and would reduce signal at the anodes. To address this problem, a coplanar anode is used alongside the field cage.

2.3.4.2 Coplanar anode

The coplanar anode (CA) is a large, negatively charged metal plate surrounding the anode strip (figure 2.14). Aided by the field cage, which causes the electrons to drift towards it, the purpose of the CA is to focus the electrons onto the anode strip at its center. The CA is wired independently of the field cage and cathode and is charged negatively compared to the anode, but significantly less negatively than the field cage or the cathode. With the CA and field cage working in tandem, ionized electrons are accelerated downward (by the field cage) and then focused into the central anode strip (by the CA). It is easy to see how this system, which consists only of components attached to the walls of the IC, would be less sensitive to microphonics than the gridded system necessary in a Frisch design.

The CA, with respect to the anode strip, can be modeled as an infinite, negatively charged plane. It works by forming an electric field whose lines fall into the anode pads (figure 2.15). Simulations of the coplanar anode show it focusing 100% of ionized electrons onto the anode pads even when the incoming particle beam is offset by several millimetres. Figure 2.16 shows these Monte Carlo simulations run in GARFIELD (CERN 2010), a drift-chamber simulation program, with a beam offset of 3mm (Gumplinger 2013). In this figure it is easy to see how well the CA focuses the electrons onto the anode pads, while also showing the basics of how the CA works. Though the field lines within the chamber
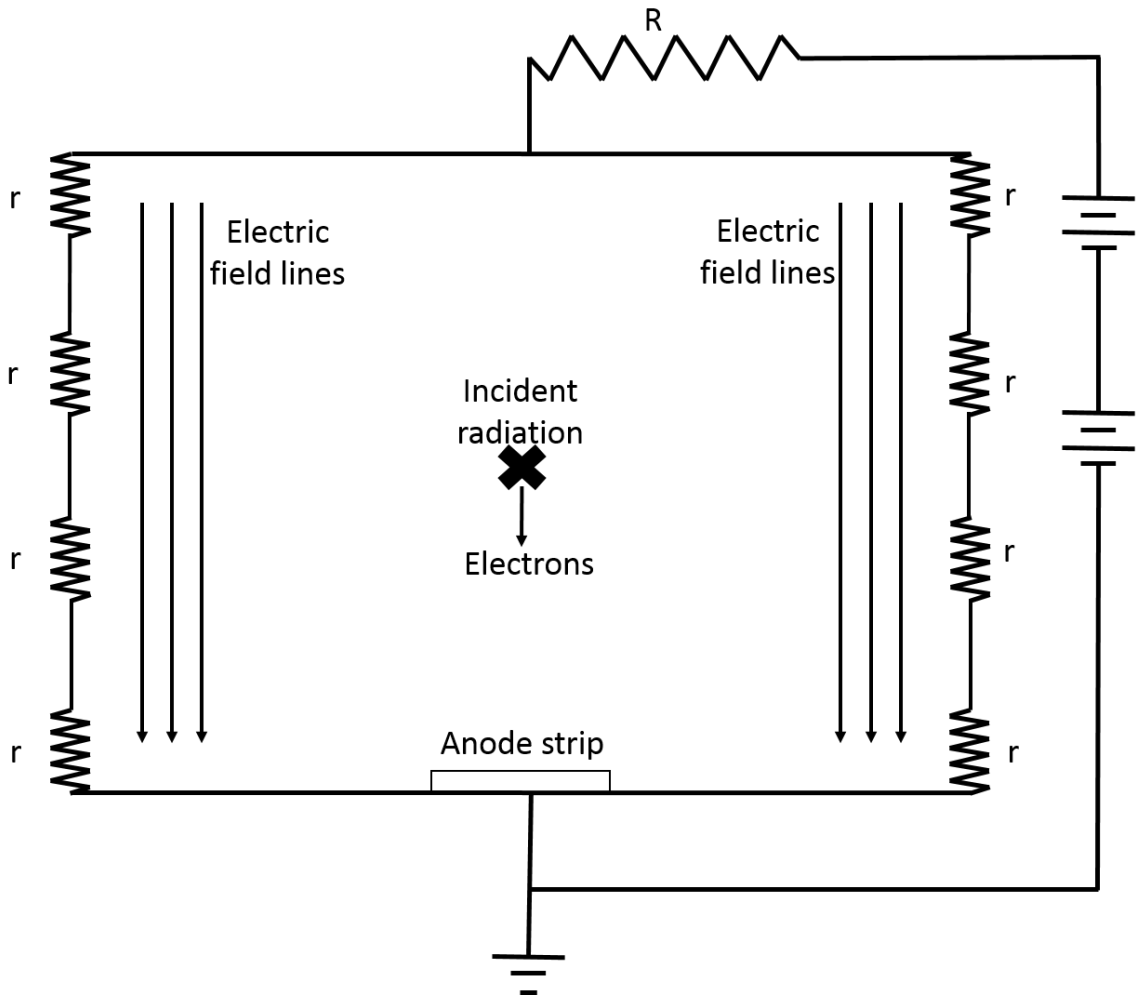
Figure 2.13: The field cage uses a series of resistors to make an electric field gradient from the cathode to the anode, thus accelerating the ionized electrons toward the anode. This simple circuit diagram explains how a basic field cage works within an IC.
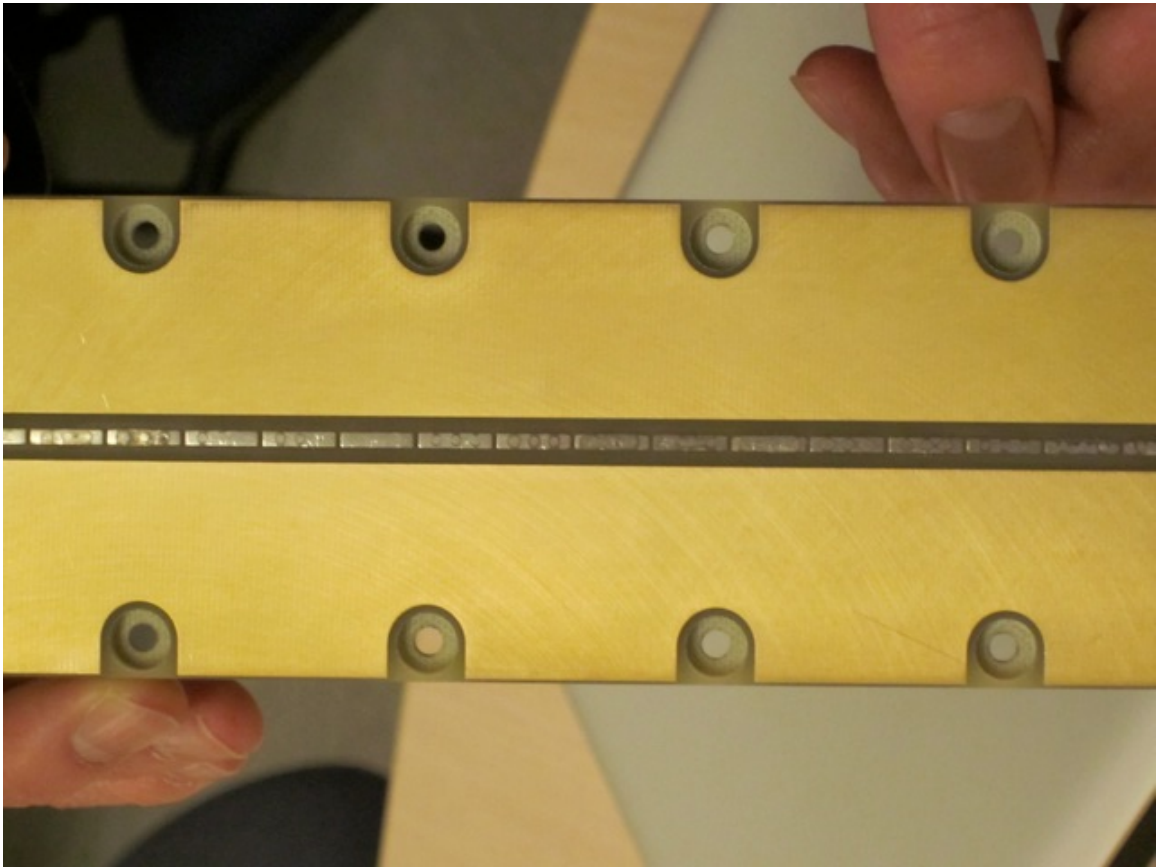
Figure 2.14: The coplanar anode is the golden plate surrounding the anode strip in the center. It is used to focus the electrons onto the anode pads.

with both the field cage and CA operating are complex, one can deduce that if the CA has a potential that is on the order of the field cage then the fields will interfere with one another, potentially destroying the electric field gradient created by the field cage, while also negating the effects of the CA, thus impairing the electron collection process. This has been both simulated using GARFIELD and experimentally tested, the results of which are shown in sections 4.4, 4.5, and 4.6.

2.3.5 Gas flow

Figure 2.17 shows the electronically regulated IRIS gas flow system used for the IC. With such low pressures, the amount of isobutane gas flowing through the IC is critical, since if it were too high the electron drift could be disturbed by the gas turbulence and if too low the gas could stagnate, hindering the recombination process. Typically, when running at 19.5 Torr, the gas system flows about 90 cm^3 per hour through the IC. The flammability of isobutane is not much of an issue as the IC operates at pressures that are below the range of flammability and the chamber itself is surrounded by a vacuum. Safety precautions are nevertheless taken in order to reduce the chance that a fire could start, if ever a leak were to occur.

2.3.6 Electronics

An integral part of the signal collection from all the detectors used for IRIS are the electronics systems. Figure 2.18 shows a basic diagram of how the electronics get the signal from the IC to the final data acquisition (DAQ) system. The signal is first collected by the anode and sent the preamplifier, which begins processing the signal. As mentioned above, each anode has its own separate preamp, and thus each anode produces a separate, processed signal. CREMAT preamplifiers are used on the IRIS IC (CREMAT 2013). The
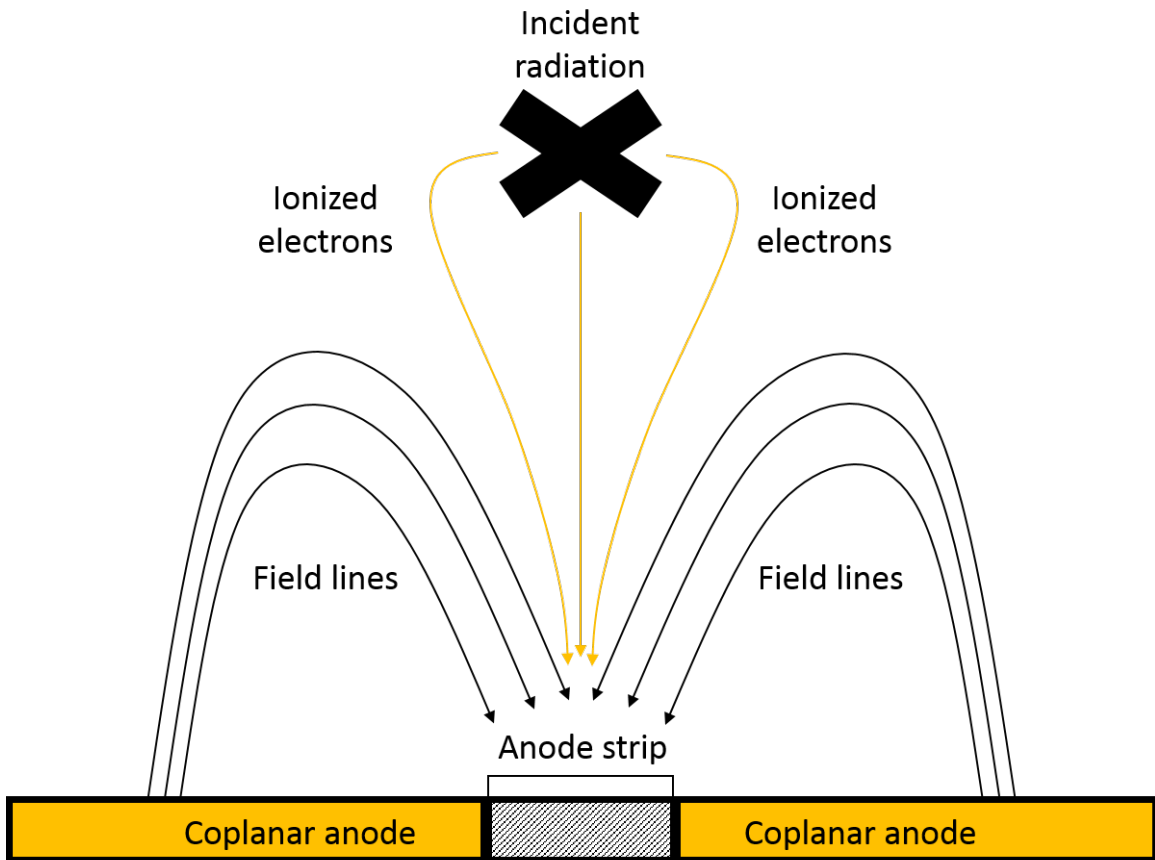
Figure 2.15: This simple, cross-sectional diagram of the coplanar anode surrounding the anode strip shows the direction of the electric field lines created by the applied bias voltage and their effect as they focus the ionized electrons onto the anode strip at its center. This is only a rough representation of the coplanar anode created to allow one to understand how it works to a first order approximation. As during operation the field can be complex, this diagram is not necessarily representative of the way in which the CA works while the IC is operating.
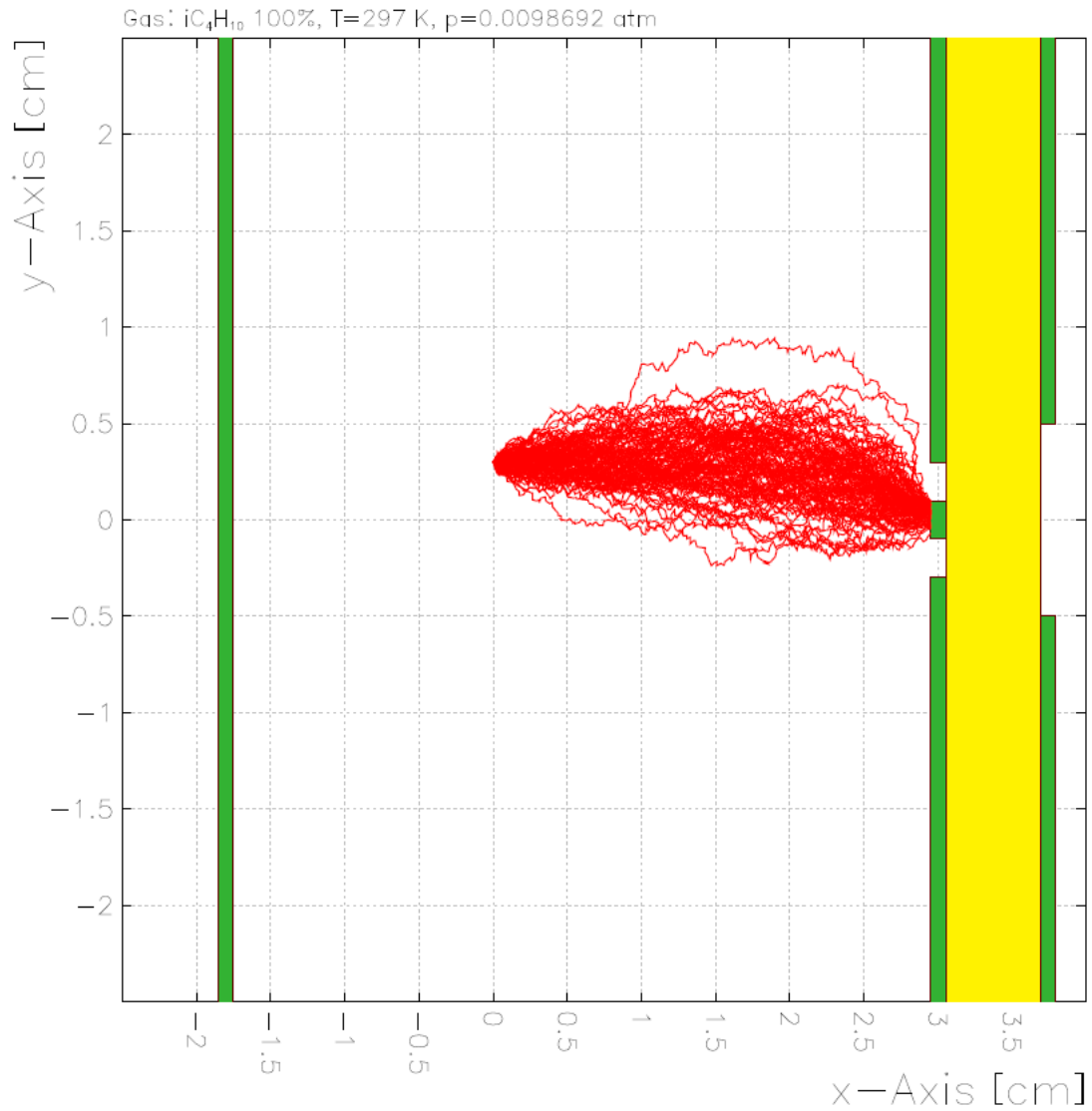
Figure 2.16: This simulation, performed by Peter Gumplinger, and run in GARFIELD, shows that even with an offset beam, the electrons (represented by the red lines) still drift onto the anode pads with the aid of the coplanar anode (in this case 100% of electrons fell onto the anode pad). Several hundred electrons were simulated within the chamber, using isobutane as the fill gas at a pressure of 7.5 Torr (Gumplinger 2013).
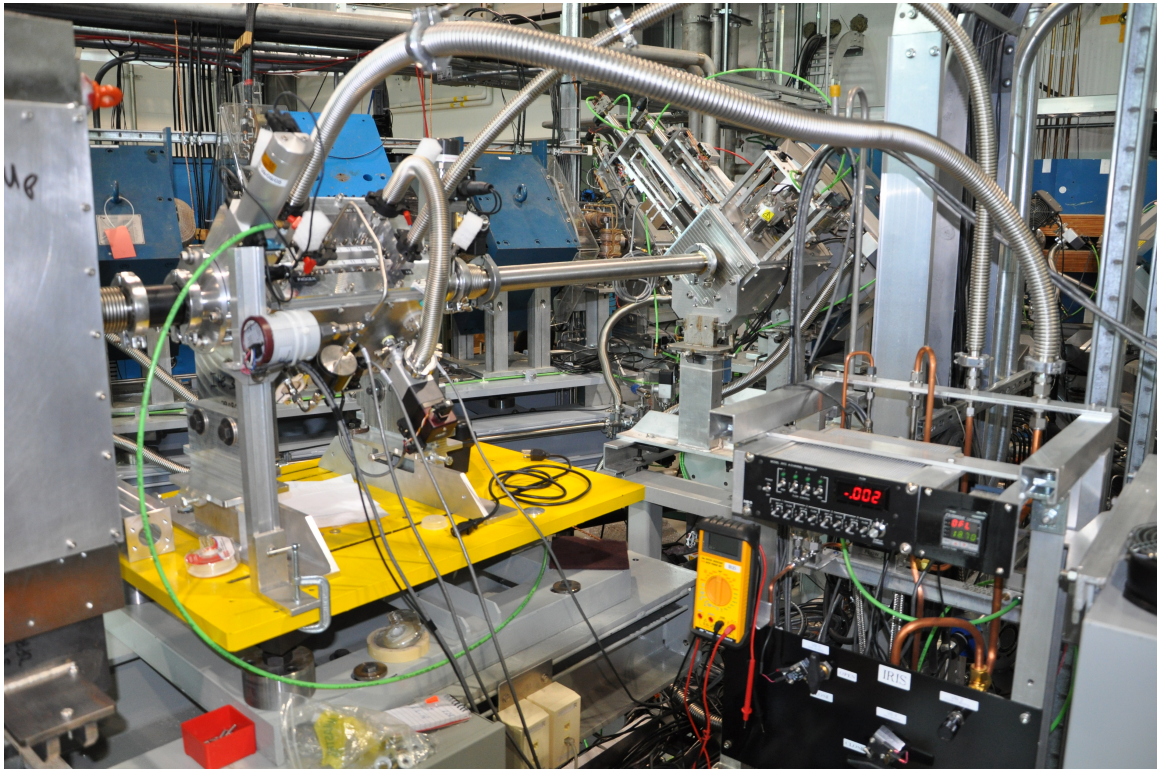
Figure 2.17: The gas flow system at IRIS. The IC, which is on the left, is fed through the pipes attached to it by isobutane which is regulated by the gas control system on the right, which shows the current gas pressure in a red, digital readout. The pressure sensor within the gas-flow system itself and is external to the IC.
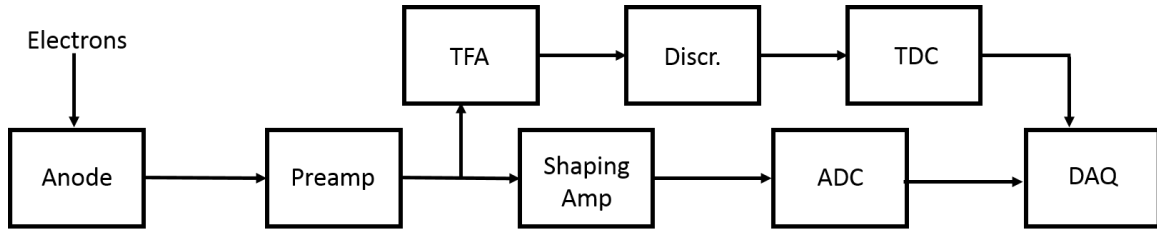
Figure 2.18: This simplified diagram shows how the signal gets from the IC to the final data acquisition (DAQ) system. Starting with the initial electrons produced by the ionization of isobutane, the signal is collected at the anode and immediately goes into the preamplifier. From there, the signal is split in two ways: the shaping amplifier, analog to digital converter (ADC), DAQ; timing filtering amplifier (TFA), discriminator, time to digital converter (TDC), DAQ.

signal then travels to the Mesytec MSCF-16 16-channel shaping amplifier (Mesytec 2013b), which allows for shaping times of 0.25 μs, 0.5 μs, 1 μs, and 2 μs. Once the pulse has been amplified and shaped into a semi-Gaussian by the shaper, it travels to the Mesytec MADC-32 (Mesytec 2013a) analog to digital converter (ADC), and finally to the DAQ. The MADC-32 can be set up to 10 μs, with a fine adjustment in order to achieve the gate width of necessary size. In addition, the signal is sent from the preamplifiers to a timing filtering amplifier (TFA), discriminator, time to digital converter (TDC), and then to the DAQ.

Chapter 3

Experiments

The characterization study of the IRIS IC was done in three major steps. Each of these experiments, detailed in sections 3.1, 3.2, and 3.3, consisted of a large amount of raw data, which was then analysed. The results of those analyses are displayed in chapter 4.

3.1 Alpha source tests

The offline studies conducted on the IRIS IC were done using a 5 MBq ^{241}Am source that emits 5.486 MeV alpha particles. This was then collimated to create approximately 10 signals per second in the IC. The IRIS system allows the IC to have multiple triggering conditions including a self trigger, wherein the signal sent to preamplifiers of the IC directly triggers the ADC gate, a silicon surface barrier detector (SSB) set in place specifically for these offline tests on the IC, or any of the IRIS detectors. During these offline studies, there was no target in place so the scattering angle of the alpha particle was essentially zero (ignoring the negligible scatter off the windows and within the IC itself), meaning that none of the main IRIS detectors would have seen the particle and thus could not be used for a trigger condition. It should be noted, however, that regardless of the condition of the SHT,
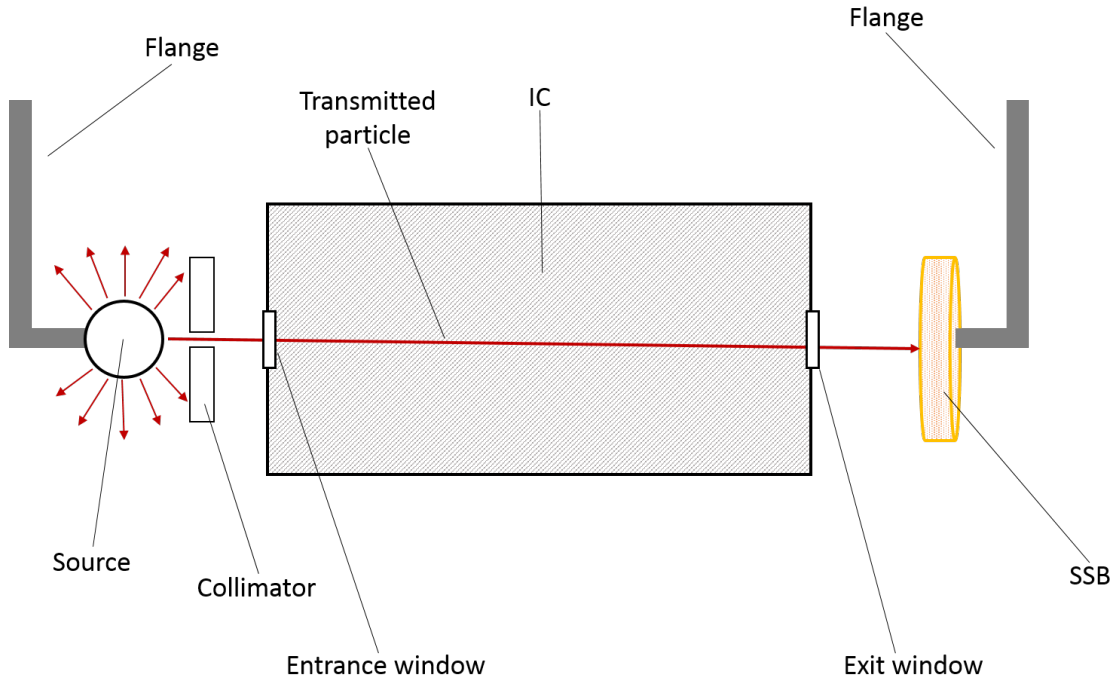
Figure 3.1: During offline studies, the 5 MBq ^{241}Am source was connected to an flange which could be swung in to or out of alignment with the entrance and exit windows. A silicon surface barrier detector (SSB), which was also connected to swinging flange, was used as a trigger for the ADC gate. The source was collimated such that only particles directly passing over the anode the strip were allowed to enter the IC.

the alpha source used for the IC is not meant to scatter off the target. For the most part, the SSB, which was placed directly in line with the entrance and exit windows was used to stop the alpha particle and create the signal to trigger the ADC gate. In certain instances, however, a self-trigger was used. A diagram of the offline IC experimental setup is shown in figure 3.1.

The ^{241}Am alpha source at 5.486 MeV, though at a much lower energy than the IC will typically experience in a particle beam, was used to study and measure various features in order to aid in the optimization and characterization of the IC before beams were sent through. This is essential, as beam time is rare compared to the ability to perform offline

tests, causing adequate preparation to be imperative. The alpha source is located on an arm which can be swung in or out of line with the IC using a simple, mechanical lever. When a particle beam is being accelerated toward the IC, the arm must be swung out, as it would otherwise block the beam. Directly opposite the alpha source across the IC is the SSB, which must also be moved out of the direct beam line so as not to interfere with the passage of the beam to the SHT.

The alpha source was used to measure the effects of shaping time, the anode configuration, the ADC gate width, and the field cage bias voltage. All these studies were run at an isobutane gas pressure of 19.5 Torr. For the field cage bias voltage, the range of voltages used with the ^{241}Am alpha source was small (-280 V to -380 V) compared to that taken with a beam as the alpha source data was not used to test the effects of the field cage on energy resolution. The MADC-32 opened the gate when triggered by the SSB or IC. It was observed that length of time that the ADC gate was open had an influence on peak position and energy resolution, thus measurements of the signal output from the IC were made using multiple gate widths (from 1 μs to 10 μs in 1 μs intervals). Though the MADC-32 is capable of doing so, we were unable to set the ADC gate lower than 1 μs as it acts as the gate for the entire IRIS data collection system, and less than 1 μs would results in signals from other detectors, such as the YY1 array and the CsI detector, arriving outside the gate. The Mesytec MSCF-16 shaper allows for 4 different shaping time settings: 0.25 μs, 0.5 μs, 1 μs, and 2 μs. The particular shaping time used was shown to have an effect on the overall energy resolution of the signal output by the IC. Using the the ^{241}Am alpha source this effect was measured in order to find the optimal shaping time with respect to energy resolution. For the anode configuration, as the IC is capable of being set from one anode with all 16 anode pads coupled together, down to 16 individual anodes in a single strip, the ^{241}Am alpha source was used for every symmetric configuration (one anode, two anodes,

four anodes, eight anodes, and 16 anodes). This was to test the minimum energy necessary to give a large enough signal to noise ratio in any given configuration, whether individual anodes would give similar signals, the possible gain differences in the preamplifiers, how the signal amplitude changed as a function of anode configuration (one would expect it to change linearly with the amount of anodes used; see section 2.3.3), do preliminary energy calibration, and test if there were any discrepancies between anodes and whether or not the possible discrepancies were dependent upon the position of the anode within the IC. The ^{241}Am alpha source, however, being of such low energy, could only provide results that required confirmation from further measurements from beams with heavier and more energetic particles. The results of all such studies are shown in chapter 4.

3.2 ^{18}O experiment

Of the two beams used to study the IC, the first was a 5.7A MeV ^{18}O beam. As each ^{18}O ion held 102.9 MeV of kinetic energy, as opposed to the 5.5 MeV carried by the ^{241}Am alpha source, and because this was a particle beam (over which there was complete control with respect to energy and rate), the breadth of characteristics we were able to study was far greater. The measurements made with the ^{241}Am alpha source were still performed, however. Moreover, using the comparison between the ^{18}O and alpha source, energy dependence could also be observed. It should be noted that the ^{18}O beam had different triggering conditions than the ^{241}Am alpha source. The IC SSB would block the beam from reaching the SHT, the trigger condition for the ADC gate to open for the system was the YY1 array and S3 detector. As this detector is external from the IC, however, it did not present any physical difference over the SSB, which was used with the alpha source. Using a particle beam as opposed to the alpha source, the average rates were significantly higher

(generally on the order of several thousand particles per second passing through the IC for the particle beam as opposed to 10 per second for the alpha source), but were well within the limits of the IC, which can read-out at over 1 MHz.

The ^{18}O beam was used to measure the effects of shaping time in order to confirm the results of the alpha source runs (the shaper was set to 0.25 μs, 0.5 μs, 1 μs, and 2 μs). Similar to the ^{241}Am alpha source as well, the 5.7A MeV ^{18}O beam was also used to measure the effects of the width of the ADC gate (which was set to 1 μs, 2 μs, 4 μs, and 10 μs), and anode configuration (the IC was set to one anode, two anodes, and four anodes). Unlike the ^{241}Am alpha source, however, the ^{18}O beam was used for a wider range of field cage voltages (-250 V, which was used for 10 Torr, -400 V, -500 V, and -600 V, which were used for 19.5 Torr), and with each field cage voltage setting, several voltages were taken set on the coplanar anode. These points were plotted as they were taken until there were at least two points on either side of the minimum value of energy resolution (see section 4.1 for an explanation of energy resolution). The coplanar anode requires a significantly smaller applied bias than the field cage and the ratio of coplanar anode to field cage bias was generally kept below 2:1. The minimum voltage tested for the coplanar anode, on the other hand, was -35 V. As simulations, which had a theoretical optimal coplanar anode to field cage bias voltage ratio (see section 4.6), had been run prior to experiments, this was a test of the validity of those simulations as well as to find the physical, optimal ratio. The ^{18}O beam was also used to measure pressure dependence, by varying the pressure from the standard 19.5 Torr down to 10 Torr. When the pressure is the lowered, the coplanar anode and field cage bias must be changed 1:1 in accordance with the ratio of pressures (thus if at 20 Torr the IC was being operated at FC $= -600$ V, CA $= -100$ V, then at 10 Torr we must adjust the voltages to FC $= -300$ V, CA $= -50$ V in order to, theoretically, have the same effect) and leaving the field cage or coplanar bias too high brings risk of a spark and

possible damage to the IC electronics. The adjusted gas pressures also allowed for studies of the minimum amount deposition necessary within the IC to produce a signal above the noise. The beam was set at 5000 counts per second except during rate test on the SHT, in which it was set as low as 250 counts per second. ^{18}O was not used for rate dependence tests.

3.3 ^{40}Ar experiment

The second beam used to make measurements in the IC was a 7A MeV ^{40}Ar beam. The main difference between the ^{40}Ar and the ^{18}O beam is the fact that argon has over twice the Z value of oxygen (18 as compared to 8 for argon and oxygen, respectively) and thus the energy deposited in the IC per atom is significantly higher. This allows for much greater pulse amplitudes, which in turn allows for observations of much the same phenomena but with a greater precision. The same setup and triggering conditions were used for ^{40}Ar as for ^{18}O. Measurements were thus made on shaping time, ADC gate width, anode configuration, the effect of field cage bias voltage, the effect of coplanar bias voltage, pressure dependence, and rate dependence. As such, much the same tests were done with ^{40}Ar as with ^{18}O: shaping time was tested at 0.25 μs, 0.5 μs, 1 μs, and 2 μs, ADC gate width was set to 1 μs, 2 μs, 4 μs, and 10 μs, anode configurations used were one anode, two anodes, four anodes, and eight anodes, field cage bias voltages were set to -200 V, -250 V, and -300 V for 10 Torr, and -400 V, -500 V, and -600 V for 19.5 Torr, coplanar bias voltages were set between -35 V and slightly over half of the field cage voltage (therefore, the coplanar anode bias voltage was dependent of the field cage bias), pressure was set to 19.5 Torr and 10 Torr, and the beam rate was set to 50 counts per second, 250 counts per second, 4000 counts per second, 10000 counts per second, and 20000 counts per second for

rate dependence studies.

3.4 Pulser tests

A pulser was used to test the preamplifiers in the IC, as the pulser sends its signal directly to the preamplifiers and bypasses the anodes completely. The pulser was operated from 500 pulses per second to 10000 pulses per second and was used to measure the effects of the ADC gate width by testing whether or not a noticeable shift in peak position was something that was purely within the electronics or if there was a physical cause (see section 4.8 for more information). The pulser was also used in offline testing for optimization purposes.

Chapter 4

Data Collection and Analysis

4.1   Analysis procedures

Every ADC channel produces an individual data set which can then be analyzed. This means, as the IC has 16 anodes, that it is possible to have up to 16 separate data sets for each event. This data is then compiled to generate a ROOT file, which contains the event-by-event ADC information and can be accessed via ROOT in order to produce spectral histograms. Using ROOT's library of fitting functions, one can then fit a Gaussian distribution to a histogram of each ADC's response and extract the mean (μ) and standard deviation (σ), from which the full-width-half-max (FWHM) and energy resolution can be calculated. ROOT uses a standard definition of a Gaussian,

$$f(x) = p_0 \exp\left(- \frac{1}{2}(\frac{(x - p_1)}{p_2})^2 \right),$$ (4.1)

where p_0, p_1, and p_2 are fitting parameters ($\frac{1}{\sqrt{2\pi}\sigma}$, μ, and σ, respectively) chosen automatically by the software to achieve the best, least squares fit. Figure 4.1 shows a standard Gaussian fit to a sample set of data collected from the IC. A point of note is that

adc15	
Entries	84151
Mean	650.9
RMS	18.31
Integral	8.027e+04
χ^2 / ndf	551.4 / 244
Constant	1973 ± 8.7
Mean	650.4 ± 0.1
Sigma	16.12 ± 0.04
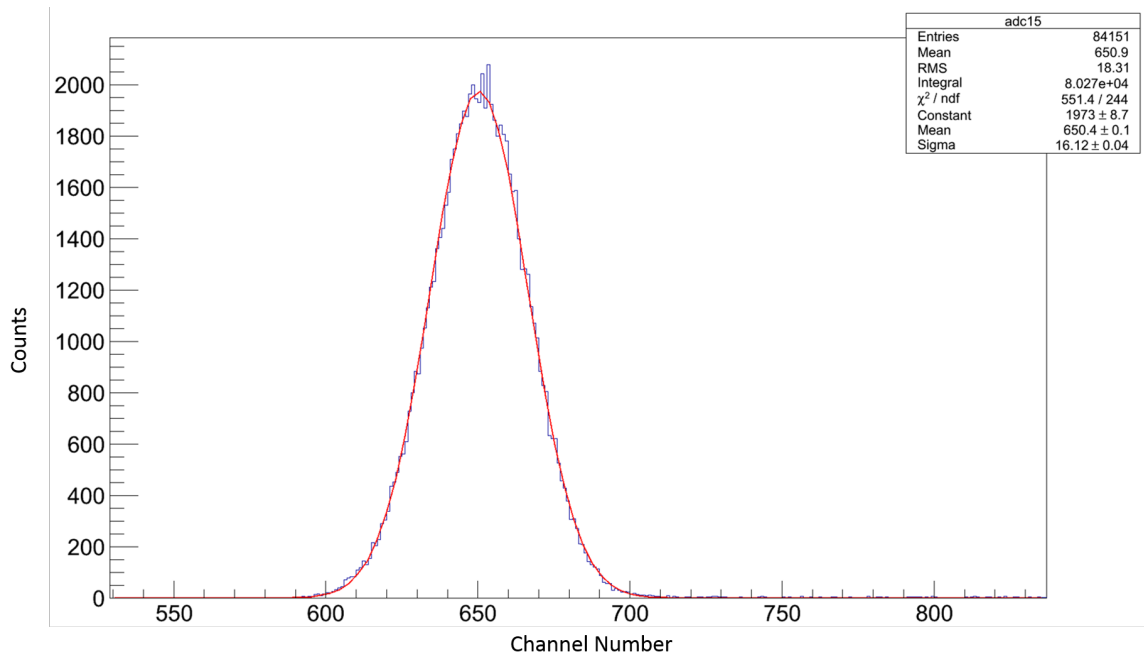
Figure 4.1: A standard Gaussian fit to a sample set of data taken from one of the ADC channels in the IC. On the abscissa are counts, while on the ordinate is the corresponding channel number, which is directly proportional to energy. The fit parameters, in which both μ and σ and their associated error are shown, are displayed in the upper right-hand corner of the of the figure. Upon a simple inspection of this fit, which is representative of most of the energy spectra produced by the IC, and its uncertainties, it is evident that a standard Gaussian provides and adequate fit for most purposes.

the raw data may not precisely follow Gaussian distributions and have a fairly complex functional form. In most cases, however, the distribution of data is very normal and a standard Gaussian provides a sufficient fit. A sample spectrum with an abscissa in both a linear and a log scale is shown in figure 4.2. As with all the spectra that will be shown henceforth, on the abscissa are counts while the ordinate shows channel number, which is directly proportional to the energy deposited within the IC. In the case of these spectra, and most future measurements other than those specifically measuring energy loss, channel to energy conversion is unnecessary as the relative differences between channels is sufficient.

The Gaussian is fit to the data through ROOT's basic fitting functions. The fit parameters
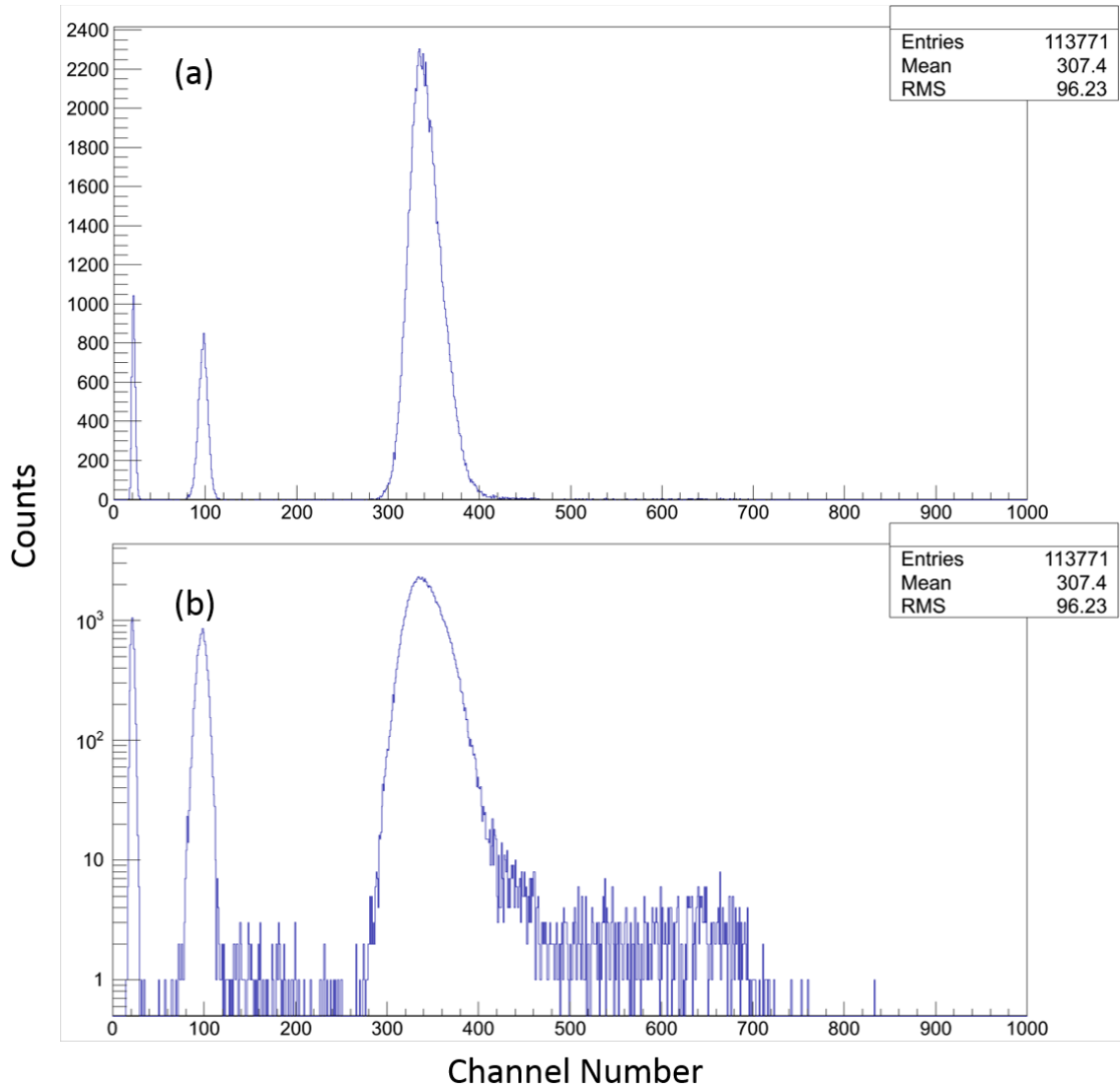
Figure 4.2: While both figures (a) and (b) are displaying the same data, (a) is on a linear scale on the abscissa while (b) is shown on a log scale. The advantages of the log scale are that small peaks that may have been hidden otherwise are now visible. For example, though it is hidden on the linear scale, the secondary peak caused by pile-up is visible in the log scale.

(μ, σ) and their respective errors $(\Delta\mu, \Delta\sigma)$ are extracted from the fit and subsequently used to calculate the percent energy resolution. The FWHM and percent energy resolution are calculated by

$$\sigma \times 2.3548 = FWHM$$
$$100 \times \frac{FWHM}{\mu} = \xi,$$

(4.2)

where energy resolution is given by ξ. This value is then plotted as a data point against the parameter in question. In most cases, several points calculated in this manner are plotted in order to see a trend in the data.

Though in most cases with the ^{241}Am alpha source and the ^{18}O beam a Gaussian precisely fits the histogram (figure 4.1), with much of the ^{40}Ar data and while at the extremes of coplanar to field cage bias voltage (section 4.5) this was not the case. This problem, of trying to fit to the extremes of field cage to coplanar anode bias voltage is shown in figure 4.3. While a Gaussian fit can show a relative mean position, it does not get an exact fit. The technique shown in figure 4.4, whereby the energy resolution is calculated by using a FWHM by taking the point at which the counts are at a maximum and calculating the corresponding channel number when the counts are equal to the maximum counts divided by two. It is likely that some form of deconvolution of a Landau function and a normal distribution is necessary to obtain exact values of energy resolution in these extreme cases. For the purpose of this study, however, that is not necessary as the energy resolution falls well above the minimum value regardless of the way in which it was calculated. This is evident from the shape of the spectrum, which includes a highly asymmetric curve as well as a large tail, and the physics of the electric field created by the coplanar anode, which is likely too low or too high to focus the electrons onto the anode pads properly. In the case of ^{40}Ar, whose data is believed to be skewed from energy straggling as well as asymmetrical

broadening due to issues with the ADC (these points will be discussed further in sections 4.2 and 4.8, respectively), a lognormal function tends to fit in cases where a standard Gaussian does not. Evidently, as there is significant skewing and broadening of the distribution it would be expected that the resolution would decrease at least somewhat when compared to the normal spectra produced by ^{18}O. These fits were all done through standard ROOT fitting procedures.

ROOT defines its lognormal fit as

$$f(x, m_0, k) = \frac{1}{\sqrt{2\pi}} (ln(k) \times x) \left(\exp \frac{-ln^2(x/m_0)}{2ln^2(k)} \right), \tag{4.3}$$

where $-k = log(\sigma)$ and $-m_0 = \mu$. These are the fit parameters that can be manually chosen or set automatically by software. In most cases, however, as we are only interested in relative peak positions and signal widths under various conditions, fitting with a standard Gaussian is sufficient. With the extreme cases, as the data are so skewed compared to normal, it is clear that the percent energy resolution has been dramatically affected (section 4.5).

4.1.1 Uncertainty calculation on fits

ROOT calculates the goodness of fit on its Gaussian fits using the chi-square method, and applies corresponding calculated uncertainties to the mean and standard deviation. It calculates chi-squared between the fitting function (in this case a Gaussian) and the data. Using the method shown in equation 4.2, the percent energy resolution is calculated and the uncertainty is propagated throughout. In general, the uncertainty in the mean was small such that it was deemed negligible and ignored in the final error calculation. The uncertainty on the energy resolution is thus calculated as
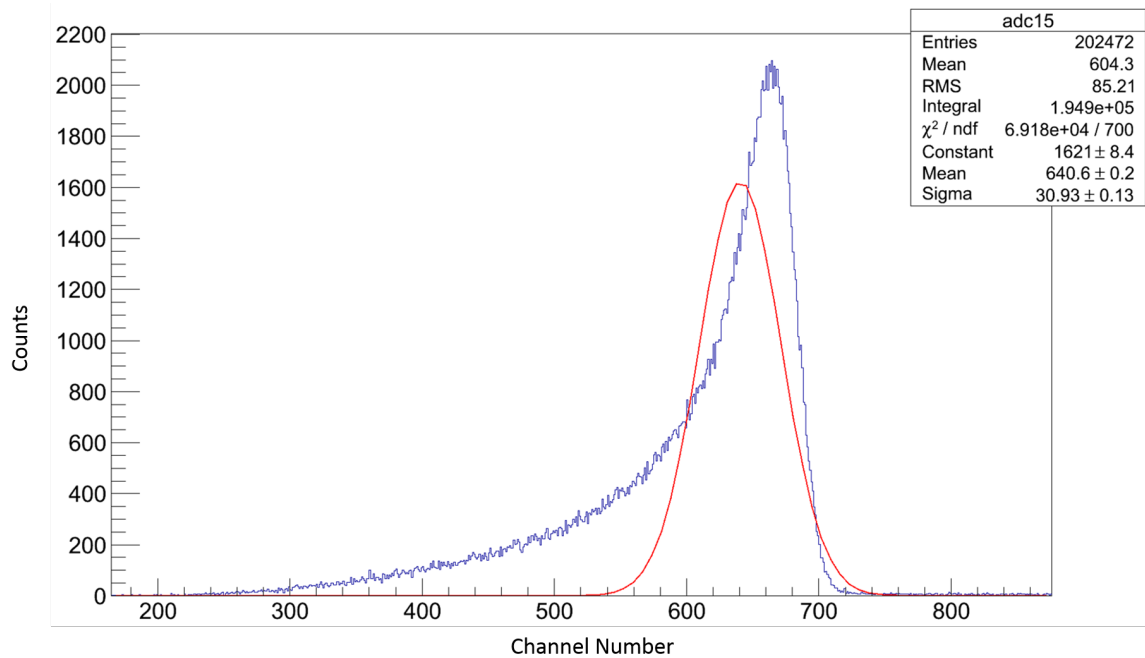
Figure 4.3: Using the same fit techniques as in figure 4.1, a Gaussian fit is applied to a data set taken from when the ratio of coplanar to field cage bias voltage was at an extreme. Evidently, this no longer follows a standard normal distribution and the energy resolution has been severely lowered.
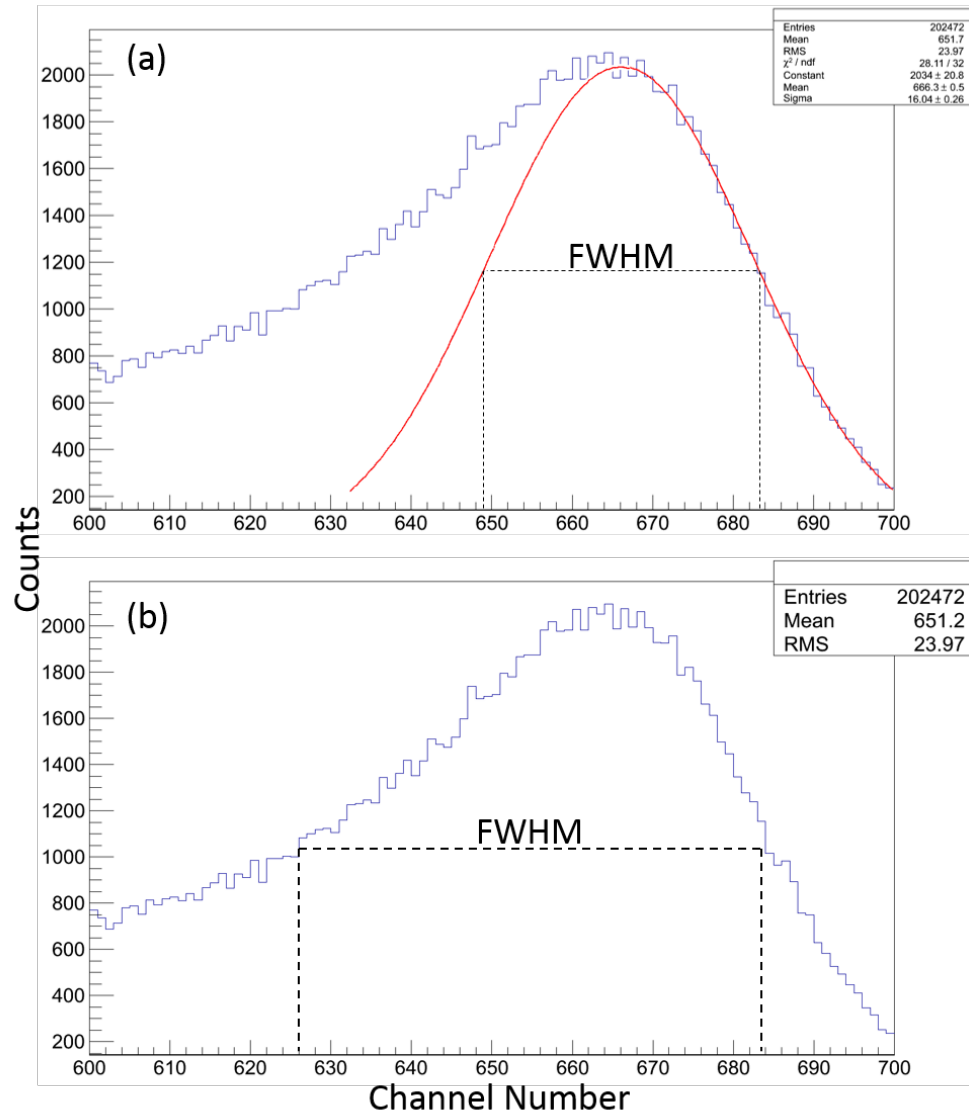
Figure 4.4: Fitting to spectra at extreme ratios of field cage to coplanar bias voltage can be done by taking the point at which the counts are at a maximum and calculating the corresponding channel number when the counts are equal to the maximum counts divided by two. From this the FWHM and energy resolution can be calculated. Figure (a) shows the part of the distribution that is Gaussian. Fitting to only this would not take into account the asymmetry or low energy tail and thus figure (b) is used instead wherein the FWHM is calculated simply finding the full height and width of the curve. Therefore (a) is not used to calculate the fit as it is only fit over a select range and is not indicative of the true FWHM. In (b), the peak maximum is found by averaging over the highest channels (the amount of which is based off the width of the peak) and full width is is simply measured at half that value. The uncertainty in the averaging is propagated throughout.

$$\Delta\xi = \xi \times 2.35\sqrt{(\frac{\Delta\sigma}{\sigma})^2}, \tag{4.4}$$

instead of the full uncertainty calculation,

$$\Delta\xi = \xi \times \left(2.35\sqrt{(\frac{\Delta\sigma}{\sigma})^2} + \sqrt{(\frac{\Delta\mu}{\mu})^2} \right) \tag{4.5}$$

wherein the $\Delta\mu$ terms can be approximated to 0, as is often the case. Through this calculation, the typical values of uncertainty, which are solely calculated from the statistical uncertainties on the fits, are on the order of 0.01%, which is generally too small to be seen in the plots shown below.

Table A.3 in appendix A displays the full breadth of quantities that measure uncertainty for a select group of fits. This includes the goodness of fit parameters χ^2 and reduced χ^2. In many of these cases the χ^2 value is high (> 2) compared to the uncertainty in both μ and σ, which is often on the order of 0.1%. The issues with χ^2 are likely due to how root handles low-statistic bins. It appears that when ROOT calculates χ^2 on bins with near zero data it causes an error, thus meaning that the goodness of fit is likely a poor indicator of the actual quality of the fit and should be ignored.

4.1.2 Energy loss

Knowledge of how much of a particle's energy is lost in the IC is integral to our ability to operate it properly; if too much energy is lost then it can affect the physics at the SHT and if too little energy is deposited in the IC, then it will be unable to classify the constituent particles of the beam, especially if many contaminants with similar Z values are present. Table A.1 contains information on the energy loss in each section of the IC as well as the total energy lost in both MeV and percentage of their initial kinetic energy for the three ions

used in these experiments (^{241}Am alpha source at 5.486 MeV, ^{18}O at 5.7A MeV, and ^{40}Ar at 7A MeV) at 19.5 Torr. Table A.2 contains the same information except at a pressure of 10 Torr. Both of these tables use values calculated using the Bethe formula, shown in equation 4.6 (Knoll 2010), through the program LISE++ (Tarasov & Bazin 2008). The Bethe formula describes the linear stopping power of a charged particle within any medium.

$$S = -\frac{dE}{dx}$$
$$-\frac{dE}{dx} = \frac{4\pi e^4 z^2}{m_0 v^2} N B \tag{4.6}$$
$$B \equiv Z \left[ln\left(\frac{2m_0 v^2}{I}\right) - ln\left(1 - \frac{v^2}{c^2}\right) - \frac{v^2}{c^2} \right]$$

In equation 4.6, v is the velocity and z is the atomic number of the incoming particle, while N, Z, and I are the number density, atomic number, and average excitation and ionization potential of the absorber atom, respectively. e and m_0 are the electron charge and mass and c is the speed of light in a vacuum. E is the energy of the charged particle while x is the range over which it travels. This makes the stopping power S equivalent to $\frac{dE}{dx}$, the differential energy loss across a distance x in a medium.

What is important to note in both of these tables is the energy loss over a single anode, as that is indicative of the size of the signal that anode is collecting. Experimentally, there is a considerable dead zone between the entrance and exit windows and the first and last anode, however, which is likely caused by a fringe effect with the electric fields generated by the coplanar anode and field cage (see section 4.3 for more details). What should also be noted is the energy lost at each anode gap (the spacing between anode pads), as that energy is likely split between adjacent anodes. The exact behaviour at both the gaps and between the windows and anodes, however, is unknown and must be simulated in the future.

Evidently, individual anodes are sensitive enough to only require a fraction of an MeV to give a signal above the noise, which peaks at around channel 22. The ^{241}Am alpha

source did not give a signal above the noise in a 16 anode configuration at 19.5 Torr, yet did show a distinguishable signal in an eight anode configuration, giving a likely threshold for a minimum energy that can be deposited in the chamber to obtain an appreciable signal to noise ratio. After adding the anode gap to each adjacent anode, the average energy deposited by the alpha source over an anode at 19.5 Torr was 0.068 MeV. This makes a likely approximate minimum threshold for energy deposited per anode to be around 0.13 MeV, significantly lower than the deposited energy per anode of either the ^{18}O or ^{40}Ar beam at 19.5 Torr and close to ^{18}O at 10 Torr (though neither the ^{18}O nor ^{40}Ar beam were not run in a 16 anode configuration).

4.2 Contributions to σ broadening

Ideally, each spectra produced by the IC would be a delta function at the channel corresponding to the energy loss of the charged particle passing through. In practice, however, this is not the case. Due to the discrete nature of the incoming radiation and the signals that it produces, which are proportional to the amount of ion pairs created, there are inherent statistical fluctuations in the energy deposited by each quantum of radiation as well as a wide range of other contributing factors that lead to a broader FWHM and a worse energy resolution. The following sections outline the main factors in the broadening of the distributions produced by the IC.

4.2.1 Noise contribution

The electrical noise can be discerned from observing the broadening of a pulser signal sent through the preamplifiers to the DAQ. Pulser tests were run in eight and four anode configurations, and the noise condition was shown to decrease as a function of the amount
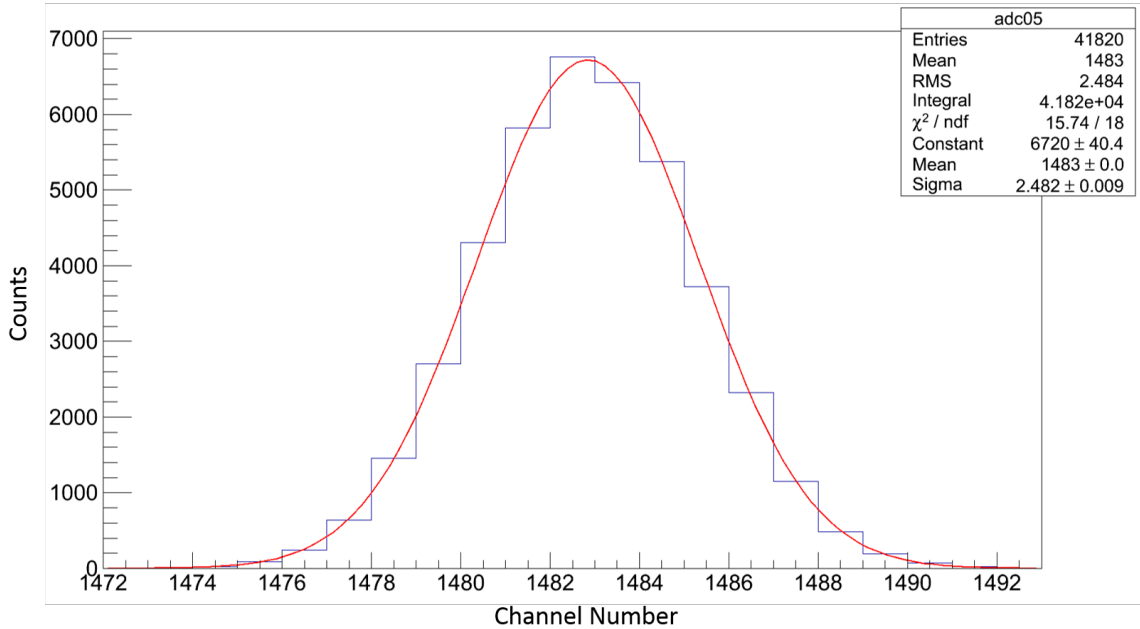
Figure 4.5: Taken using the pulser in an eight anode configuration, the data shows that the distribution produced by the pulser as it pulsed the CREMAT preamplifiers. The distribution here represent the electronic noise in the signal processing system for the IRIS IC.

of anodes coupled together (when looking at a single section as opposed to adding the sections event-by-event). For the eight anode configuration, among the eight anodes there was an average mean of 1490 ± 45 channels with a σ of 2.6 ± 0.2 channels. This amounts to an average energy resolution of $0.41\pm0.04\%$. With a four anode configuration, there was an average mean of 2932 ± 14 channels with a σ of 3.35 ± 0.06 channels. The average energy resolution is thus $0.269\pm0.006\%$. It should be noted that the statistical uncertainty of the fitted functions in both the mean and standard deviation were so low as to be negligible (figure 4.5).

From this information one can extrapolate the electrical noise conditions at each anode

configuration. This amounts, essentially, to the size of σ and FWHM. This shows that the electrical noise contribution to the overall broadening is small, at about 3 channels. It is important to note that this is only an approximation, as this data was taken prior to the experiment and noise conditions often change it is not necessarily indicative of the noise conditions during the actual runs. It is likely that there are other factors that broaden the distributions significantly.

4.2.2   Energy straggling

Energy straggling is caused by inherent statistical fluctuation in the energy deposited by an incoming particle due to the stochastic nature of particle interactions. It is thus an irreducible quantity and often has a major broadening effect on σ. The nature of energy straggling means that with heavier particles containing more protons it will have a more pronounced effect on increasing σ. The energy straggling component was calculated using LISE++ (Tarasov & Bazin 2008) and compared to the measured energy loss distributions and corresponding σ for both ^{18}O and ^{40}Ar. It should be noted that the measurements and subsequent calculations were done for an eight anode configuration, and due to the charge collection problems at the outer anodes (see section 4.3.2), only the inner 12 anodes were considered.

Energy calibration for ^{18}O, when taking into account only the inner 12 anodes and the beam passing through the entrance window and the first section of the IC, gave a channel to energy conversion of 0.005807 MeV/channel. The total measured σ was 0.12 MeV, while the total calculated energy straggling contribution to σ was 0.08 MeV. For ^{40}Ar, the energy calibration showed 0.007285 MeV/channel, the total calculated energy straggling contribution to σ was 0.16 MeV with a total measured σ of 0.37 MeV. Both ^{18}O and ^{40}Ar measurements were taken with optimal IC running conditions (ideal IC settings are

explained in greater detail in sections 4.4,4.5, and 4.6) in an eight anode configuration with the signals from each anode added event-by-event.

Though the absolute effect of energy straggling on σ increased from ^{18}O to ^{40}Ar, the relative contribution of energy straggling to the total σ decreased (with ^{18}O energy straggling accounted for 67% of σ, while in ^{40}Ar energy straggling accounted for 43% of σ). The totalσ is a combination of various factors, as shown in equation 4.7.

$$\sigma_{total} = \sqrt{\sigma_{noise}^2 + \sigma_{straggling}^2 + \sigma_{other}^2} \tag{4.7}$$

This reduces the relative contribution of energy straggling to the total σ even further. It thus clear that while energy straggling contributes a significant portion of σ, there are other factors which are increasing σ, especially as the mass and charge of the ions increases.

4.2.3 Other possible contributors

The nature of major contributions to sigma beyond electrical noise and energy straggling are, as of yet, unknown, and further study is necessary to determine, and possibly work to reduce, these sources of broadening. With the information at hand, one can only speculate as to the nature of the processes, be they physical or electrical, that are causing the majority of the broadening. Certainly, once the charge collection problems are better understood (section 4.3.2), this task will be simpler.

4.3 Multi-anode configuration

The IRIS IC's ability to physically couple between one and sixteen of its anode pads (see section 2.3.3) was utilized in order to study whether or not the anode configuration affected the charge collection and signal output. The IC was configured from between one

and 16 anodes for the ^{241}Am alpha source, one and eight anodes for the ^{40}Ar, and one and four for the ^{18}O. Evidently, in a single anode configuration the signal was largest when using the ^{40}Ar beam as it has the largest Z (and Q) and thus produces the most ionization within the chamber. This is shown in figure 4.6, which is a comparison of the signals collected by each of the three different sources used in the IC with a single anode configuration. It should be noted that peak positions shown in figure 4.6 may differ slightly by the expected proportionality factor of $\frac{z^2}{v^2}$, as the voltage settings, especially for the alpha source, were not at the exact same ratios.

While running measurements with the 5.486 MeV ^{241}Am alpha source, the IC was set up in all possible symmetric anode configurations (one anode, two anodes, four anodes, eight anodes, 16 anodes). This was to test the detection efficiency of the IC and the minimum possible deposited energy values that gave a signal that was measurable above the noise. All of these tests were done at 19.5 Torr. With the 16 anode configuration the signal was too close to the pedestal in order to do a sufficient analysis (figure 4.7), while the eight through one anode configurations, though small, showed a signal that was above the noise. Measurements with the ^{18}O and ^{40}Ar beams were done in configurations of one, two, and four anodes and one, four, and eight anodes, respectively. Both of the particle beams' output spectra were well above noise levels in all configurations, which allowed for analysis and further studies.

4.3.1 Energy deposition

Calculated with LISE++ (Tarasov & Bazin 2008) at 19.5 Torr, the 5.486 MeV ^{241}Am alpha source, after passing through the 900 nm Mylar entrance window, deposits a total of 1.25 MeV across the IC (table A.1). This amounts to an average of 0.068 MeV deposited per anode pad after the gaps between the windows and the anodes are taken into account
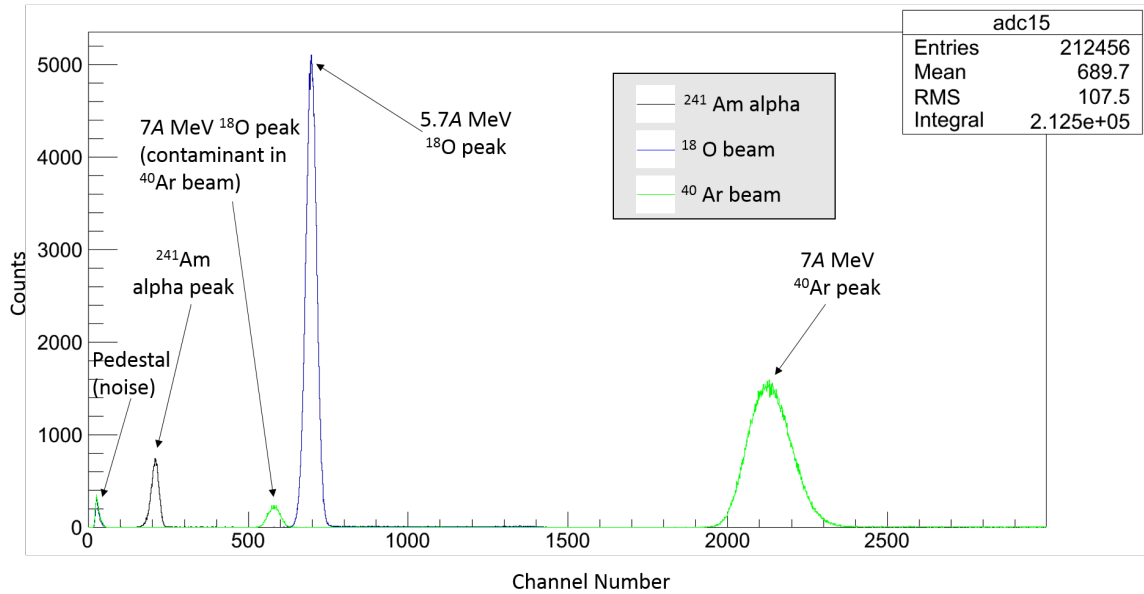
Figure 4.6: A comparison of the peak positions of the ^{241}Am alpha source and the ^{40}Ar and ^{18}O beams using a single anode configuration and optimal IC settings (optimal settings will be discussed in greater length in sections 4.4, 4.5, and 4.6). The height of any particular peak is a function of the beam rate and time and thus it is the position on the abscissa that is most important. From right to left, increasing in energy, is the ^{241}Am alpha source (black), followed by ^{18}O (blue), and finally ^{40}Ar (green). The first peak, which has all three colours overlayed, is the pedestal, while the small green peak next the ^{18}O peak is an oxygen contaminant in the argon beam (see section 4.7). The ^{18}O beam at 7A MeV is at a lower energy than the ^{18}O beam at 5.7A MeV due to the $\frac{1}{v^2}$ dependence in the Bethe formula (equation 4.6).

and assuming that every electron that is ionized is collected by the 9.5 mm anode pads. This signal appears to be below the acceptable lower limit for a signal from a single anode as it was lost in the noise (figure 4.7). In contrast, however, by simply coupling two anodes together and changing to an eight anode configuration, the average energy deposited per pad doubles to 0.136 MeV, which increases the signal to a level well above the noise (see the eight anode configuration in figure 4.8). It should be noted, however, that the averaging calculations applied to determine energy deposition per anode are not wholly accurate; the reason for this inaccuracy is explained in subsection 4.3.2. As the number of anodes coupled together are doubled so too does the signal they receive and subsequently output. The noise, however, stays constant regardless of anode configuration, thus explaining one of the major advantages of having the ability to physically couple anodes together. Figure 4.8 shows a comparison of the ^{241}Am alpha spectra at different anode configurations. Here the noise has been subtracted out through a peak-pedestal subtraction so that only the spectra created by the energy deposited by the alpha source can be seen.

With the 5.72A MeV ^{18}O beam, one, two, and four anode configurations were used at a pressure of 19.5 Torr and only a one anode configuration at 10 Torr. As the total energy loss inside the IC for the 5.72A MeV ^{18}O beam at 19.5 Torr was 5.72 MeV, as opposed to 1.25 MeV for the 5.456 MeV ^{241}Am alpha source (table A.1), each anode pad was subject to a significantly higher amount of ionization (0.31 MeV/anode pad, which is nearly five times greater than the energy per pad of the alpha source). Figure 4.9 compares the signals of the alpha source and the ^{18}O beam with a single anode configuration. From this one can easily see the difference in the energy deposited between the two sources.

The 7A MeV ^{40}Ar beam was run with the IC in configurations with pads coupled to form one anode, two anode, four anode, and eight anode sections. The ^{40}Ar beam deposited significantly more energy within the chamber than the other two sources used, which is
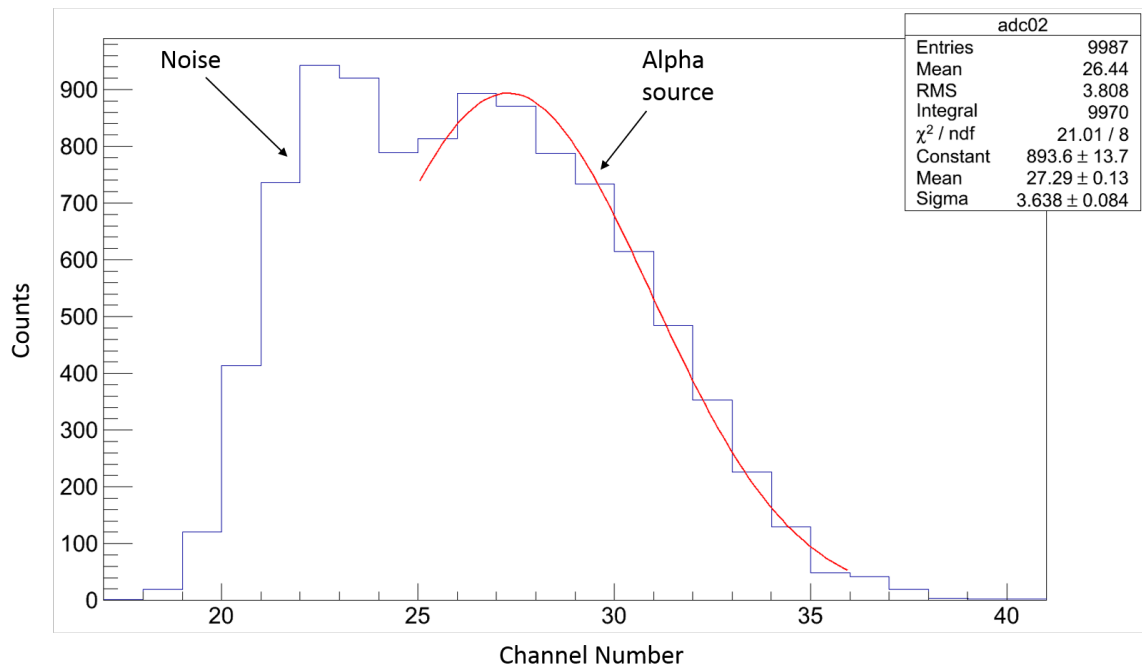
Figure 4.7: Taken using the ^{241}Am alpha source in a 16 anode configuration, the data shows that the distribution produced by the alpha source within the IC at many of the anodes is too close to the noise to be useful.
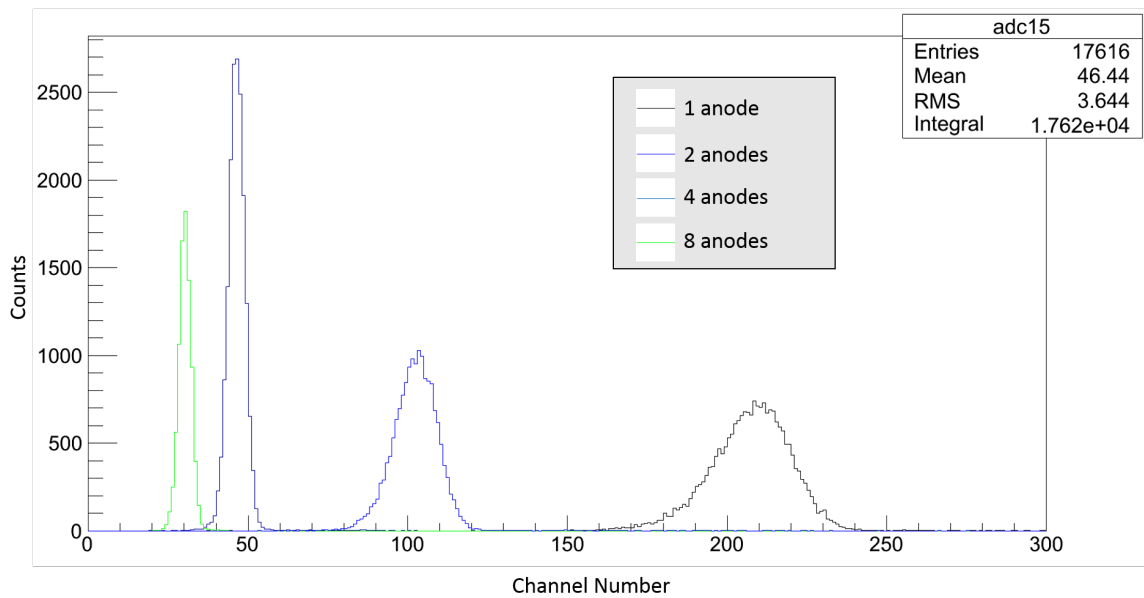
Figure 4.8: A comparison of the peak positions of the ^{241}Am alpha source with various anode configurations, from a single preamplifier output. From right to left the configurations are eight anode (green), four anode (dark blue), two anode (light blue), one anode (black). The reason as to why their peak positions are not exactly double one another is explained in section 4.3.2.
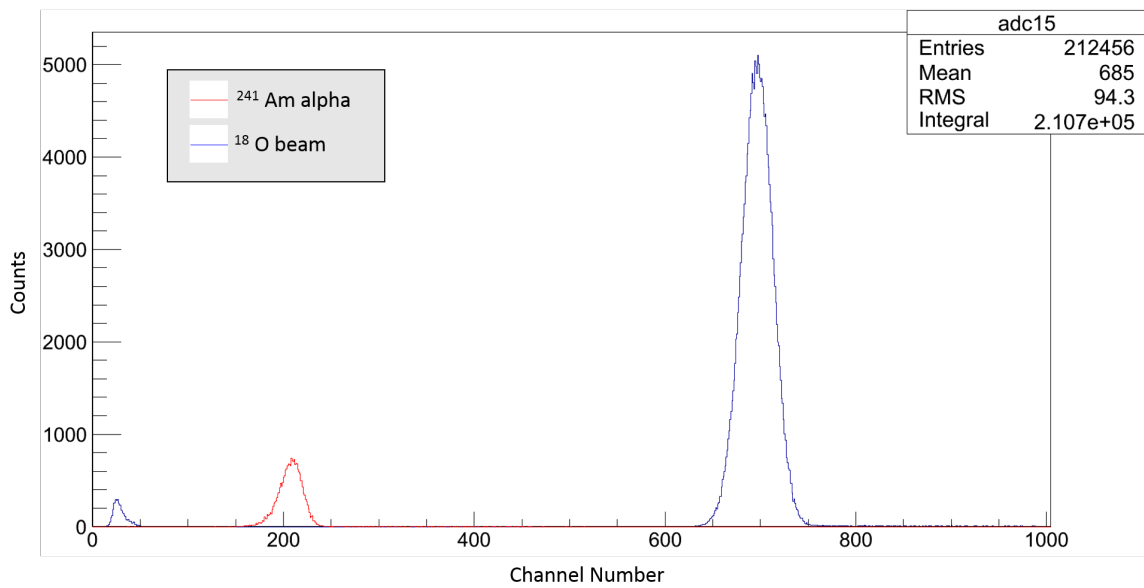
Figure 4.9: A comparison of the signal strength produced by the ^{241}Am alpha source and ^{18}O beam with a single anode configuration. The ^{18}O beam is the higher energy peak (blue), and the ^{241}Am alpha source is the much lower energy (red) peak. The blue peak left of the alpha peak is pedestal (noise). One should note that the height of the peak is determined by the integral of counts over time, while the position of the peak on the abscissa determines the energy deposited.

obvious when comparing an alpha particle (2 protons) to oxygen (8 protons) to argon (18 protons) and the fact that energy deposition within the IC is proportional to the square of the Z value of an ion (equation 4.6). Thus we were able to run ^{40}Ar at both 19.5 Torr and 10 Torr with high signal to noise ratios in all configurations. At 19.5 Torr the total energy loss within the IC for ^{40}Ar at $7A$ MeV is 19.32 MeV, while at 10 Torr the total loss is 9.81 MeV. Thus even at 10 Torr, the energy loss through the chamber in ^{40}Ar was nearly twice as great as ^{18}O at 19.5 Torr. The average energy deposited is 1.13 MeV/anode pad at 19.5 Torr and 0.57 MeV/anode pad at 10 Torr (refer to appendix A for tables of the full energy loss across the IC).

4.3.2 Charge collection discrepancy

One would expect the anode configuration to have little effect on the total charge collection, especially when the signal can be added event-by-event across all anodes. This was not the case, however, as there appears to be an extensive discrepancy in the charge collected by the two outermost anodes (anode 00 and anode 15) when compared the 14 innermost anodes. This is shown in figure 4.10, where in an eight anode configuration and with an ^{40}Ar beam, the peak positions of the outermost anodes are significantly shifted downward in energy, indicating that there is some sort of problem with the charge collection, even when gain differences in the individual preamplifiers are taken into account. A major problem this causes is that when using configurations involving the two outermost anodes the signal amplitude does not double, as it should, when the number of coupled anodes are halved. As this only happens at the two outermost anodes, it was important to run a pulser test in order to check if this was a problem with the electronics or something physically happening within the IC causing this unforeseen discrepancy in charge collection at the outer anodes.

The pulser data taken is shown in figure 4.11, in which the pulser was used to send signals to the preamplifiers directly. This data is useful in determining the cause of the discrepancy between anodes as it bypasses them completely. As can be seen from figure 4.11, the pulser showed no disparity between preamplifier outputs beyond the expected gain differences, especially when compared to figure 4.10. The gain differences in preamplifiers may account for up to a 10% variance between the pulse amplitude output by an individual anode, whereas the outer two anodes are, in some cases, off by over 50% (in an eight anode configuration) from the inner ones. It is thus postulated that the signal discrepancy between anodes is likely due to a fringe effect in the electric field caused by the field cage and coplanar anode's interacting electric fields. Further investigation, in particular with each anode read out, is necessary in order to understand this problem more clearly, however. Nevertheless, results substantiating the fringe field hypothesis are shown in section 4.6 wherein the energy resolution as a function of the ratio of the bias voltages between the coplanar anode and field cage are explored. In figure 4.10, it is interesting to note that the lower-energy distributions of the outer anodes are not exactly half of the inner anodes. This lends more credence to the idea that it is a fringe field effect, and makes it unlikely that the anodes are not working altogether, though it is still possible that they are malfunctioning in some way that we are unable to detect beyond this signature. This discrepancy is also shown in the the theoretical peak position versus measured peak position plots (figure 4.12) when comparing differing anode configurations.

4.3.3 Added anodes

Event-by-event addition of the signals output by individual (or coupled) anodes was done in order to compare the various anode configurations. Figure 4.13 shows a comparison between a single anode and added multi-anode configuration. As one can see, the results
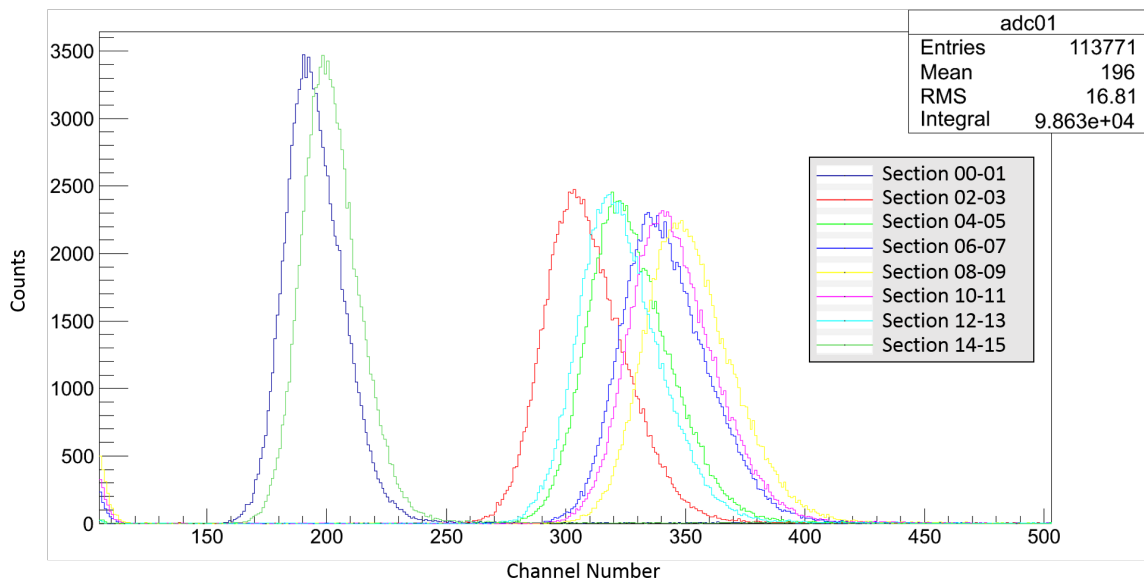
Figure 4.10: Taken with an ^{40}Ar beam at 5.72A MeV in an eight anode configuration, the outer anodes (in this figure section 01-02 and section 14-15, which are dark blue and dark green, respectively) have a significantly smaller signal than the inner anodes. The reason for the broadening of the higher energy peaks is from the greater amount of electrons collected.
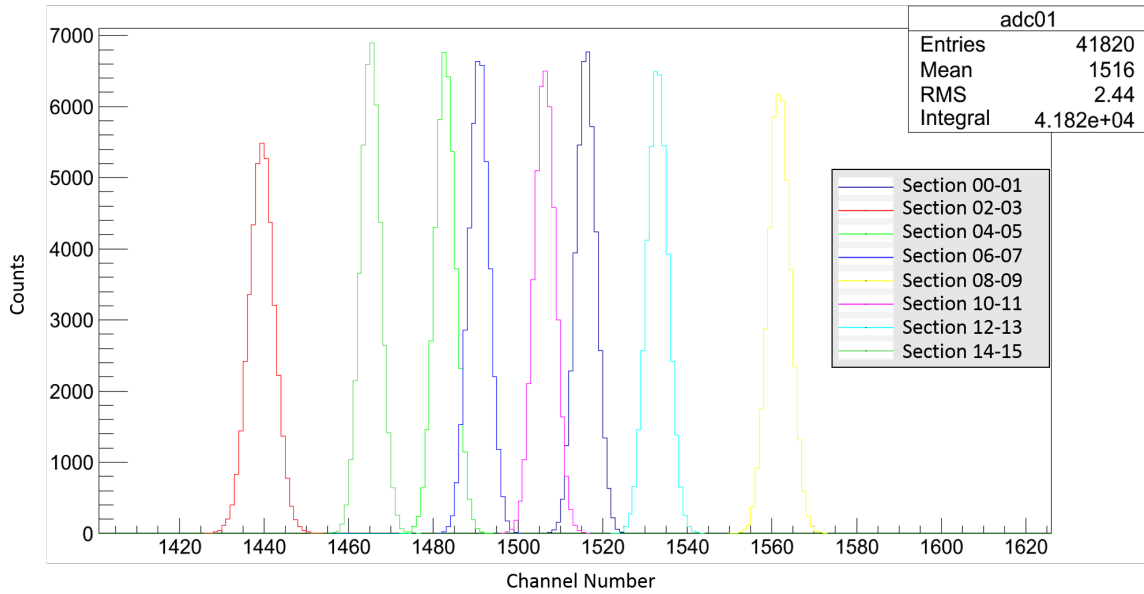
Figure 4.11: The pulser, which was used to send a signal directly to the preamplifiers, thus bypassing the charge collection process and anodes completely, shows that the signal discrepancies at the outer anodes is unlikely an issue with the electronics in the anodes as the pulser signal shows up equally through all preamplifiers; there are slight gain differences in the preamplifiers, which accounts for the 5%-10% shifts in peak position (as opposed to over 50% in figure 4.10) and is why the individual spectra are not all lying on top of one another. The signals from section 00-01 (dark blue) and section 14-15 (dark green) are in the center of the pack here, as opposed to being stark outliers as they are in figure 4.10.
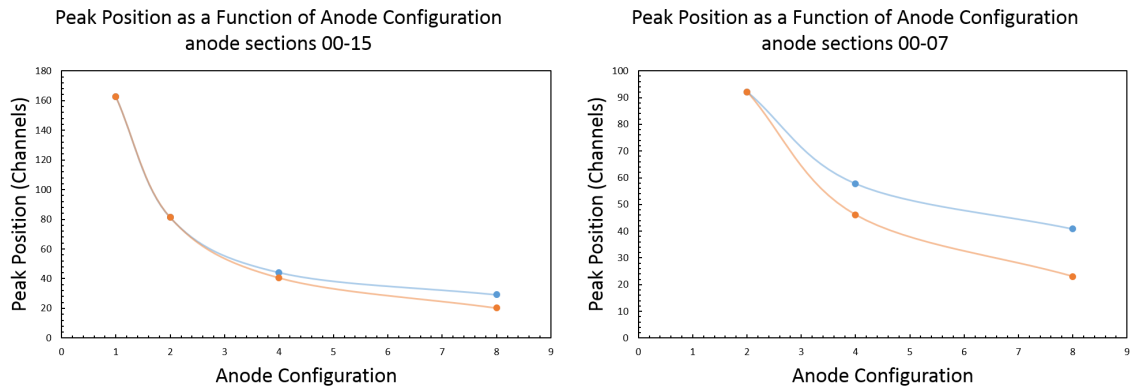
Figure 4.12: Mutli-anode configurations show a discrepancy in theoretical and actual peak positions. The blue line shows what the theoretical peak position should be (when calculated from the same starting point; hence why they start at the same value), while the orange line shows the measured peak positions. This difference is due to the charge collection discrepancy in the outer anodes. This was calculated simply by dividing the initial signal with one anode by the ratio of the total amount of anodes available to the number of anodes coupled together (for eight anodes the signal was divided by $16/8 = 2$, etc.) The reason as to why section 00-15 fits the theoretical curve significantly better than for sections 00-07 is that when section 00-07 is put into multi-anode configurations, the ratio of the loss from the outer anodes (anode 00 and anode 15) is larger compared that with twice as many anodes (section 00-15). This data was taken using the ^{241}Am alpha source.

are fairly consistent between the two peaks after pedestal subtraction. In both cases the outermost anodes are exhibiting the collection problems discussed above, which would explain the consistency amongst the results of multiple added anodes and a single anode. In figure 4.13, the difference in peak position (of approximately 100 channels) comes from gain differences in preamplifiers. In a single anode configuration there is only one preamplifier, yet for eight anodes there are eight preamplifiers, some of which have a higher gain, which causes the sum of the histograms to be slightly higher. This causes a decrease in the overall percent energy resolution (increase in energy resolution) as a function of the number of anodes that are added together, as shown in figure 4.14, in which voltage parameters are held at optimal settings for all points and only the anode configuration is changing. This better energy resolution is likely due to both capacitance matching between the multiple preamplifiers and the anodes and gain increases. It should be noted that the gain of individual preamplifiers cannot be adjusted.

4.3.4 Correlation study between anodes

In order to study the correlation between anodes and observe any possible discrepancies, the signals produced by the various anodes were plotted against one another in order to produce two-dimensional histograms. If the anodes were perfectly correlated, the corresponding histogram would be a circle centered around the (equivalent) mean positions of signals produced by each anode. Figure 4.15 shows a 2-dimensional plot of anodes 03 and 07 against one another. This was taken with the ^{18}O beam at a field cage bias voltage of -500 V and a coplanar anode bias voltage of -87 V (experimentally determined to be optimal conditions for ^{18}O at 19.5 Torr) in a four anode configuration. The colour on the z-axis represents the number of events per pixel, from few (violet) to many (red). As the points lie essentially along the line $y \approx x$, this indicates highly correlated anodes (beyond
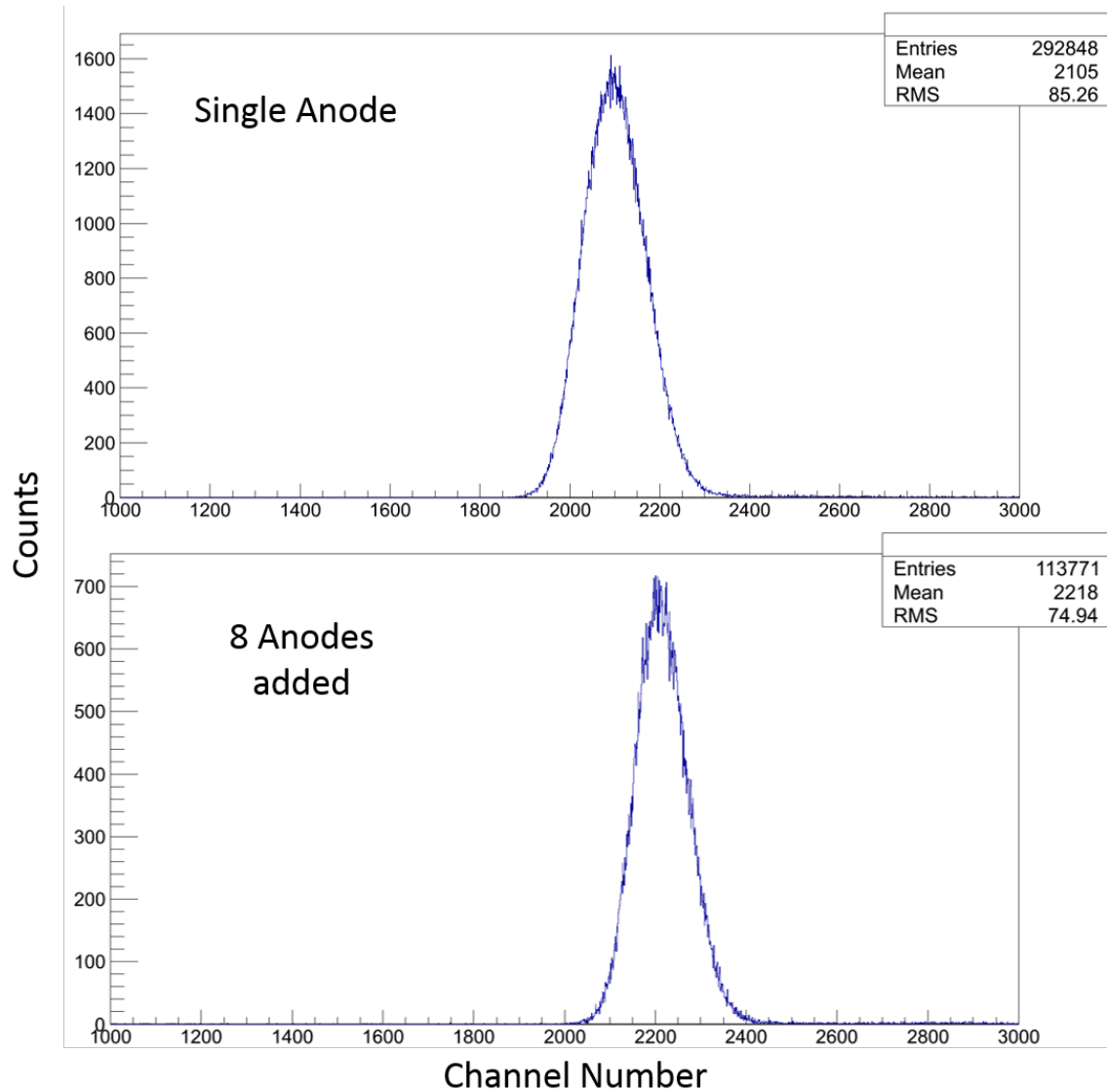
Figure 4.13: Taken with the ^{40}Ar beam at 7A MeV with a field cage bias voltage of -600 V and coplanar anode bias voltage of -110 V, a comparison of 8 anodes added together event-by-event (bottom) and a single anode (top). The slightly higher pulse amplitude from the added anodes comes from gain differences between preamplifiers as eight separate preamplifiers are being used here as opposed to the single one used above.
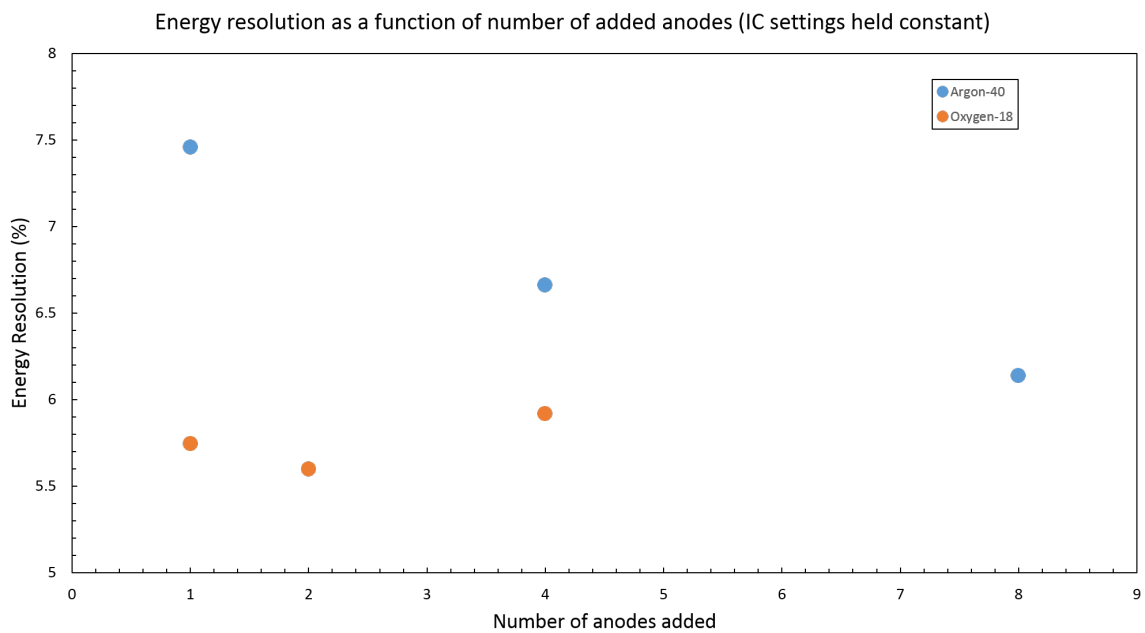
Figure 4.14: With the IC settings held constant, the resolution generally increases with the number of anodes added, except for the outlier point in ^{18}O. This shows that, when possible, the IC should operate with as many anodes as possible, as the percent energy resolution decreases roughly linearly as a function of the anode configuration.

negligible energy loss between anode pads). The reason that the histogram is elliptical and not perfectly circular is both that the mean positions of the two anodes do not exactly match up and that neither anode is producing a perfectly Gaussian shape, which is due to gain differences in preamplifiers as well as a slight difference between the energy deposited in the anodes caused by energy loss over the length IC. In figure 4.15, as there is not a second cluster of points centered at twice the value of the main cluster, it indicates that there is little to no pile-up. And as there are no outlying points beyond the line $y \approx x$, it shows that there no unwanted reactions taking place inside the IC. Figure 4.16 is the same plot as in figure 4.15 except with the ^{40}Ar beam set to a field cage bias voltage of -600 V and a coplanar anode bias voltage of -110 V (experimentally determined to be optimal conditions for ^{40}Ar at 19.5 Torr). There are several differences between the two plots that should be noted: there is significantly more pile-up in the ^{40}Ar plot, as shown by the long tail, which could be due both to a higher beam rate and the higher amount of ionization in the chamber. There are also two major clusters in figure 4.16 (as opposed to the one in figure 4.15), the smaller of which is the ^{18}O contamination (section 4.7). The correlation between the anodes is not as good with ^{40}Ar as it is with ^{18}O, either. This is due to a multitude of reasons which includes broadening due to ADC peak addition (section 4.8), more energy loss between anodes, and a higher amount of energy straggling because of a greater Z value.

4.4 Field cage bias voltage

As explained in section 2.3.4.1, the field cage is responsible for creating the electric field gradient that accelerates the ionized electrons toward the anode pads. According to the IC designers, at the pressure regime in which the IC was being operated, one can safely
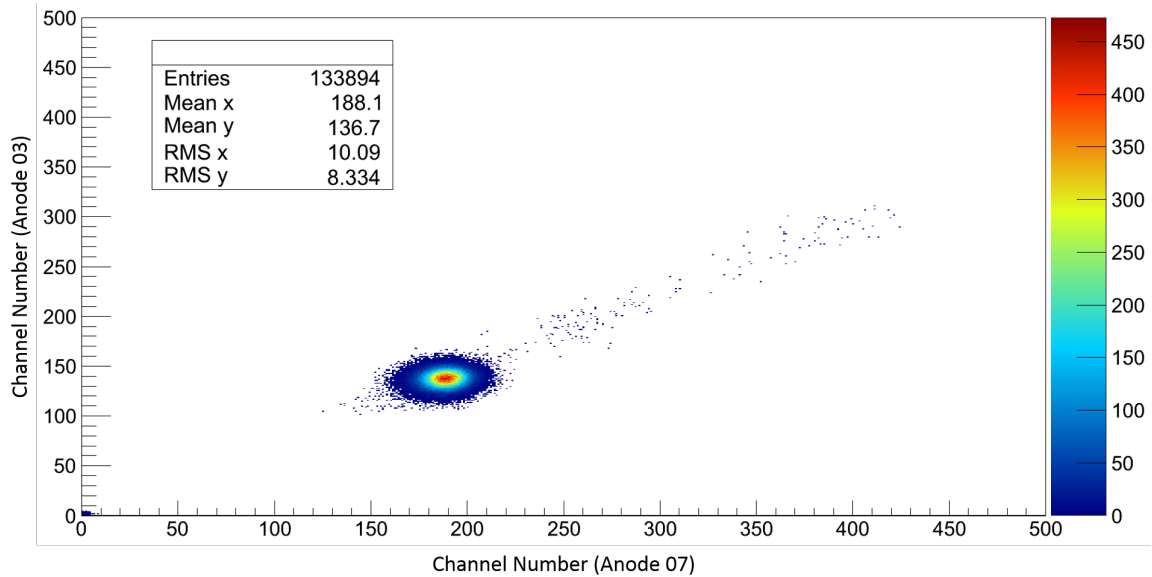
Figure 4.15: Taken with a 5.7*A* MeV ^{18}O beam, a 2-dimensional histogram of anodes 03 (abscissa) and 07 (ordinate) plotted against one another. The z-axis, represented by the colour scale, shows the number of events per pixel. This shows a near perfect correlation between the anodes as well as minimal pile-up and no reactions in the chamber.

bias the field cage with fairly high voltages before the risk of a spark between the high voltage connectors and ground, which could potentially damage the preamplifiers, becomes an issue. For our purposes, however, the maximum bias voltage was set to -600V as that was sufficient for the tests that were conducted and it reduced risk of a possible spark or damage. The main reason for running the field cage bias at this relatively "low" voltage is that with isobutane there is a broad minimum in the transverse diffusion vs E/P (electric field/pressure) plots, that lies between E/P $= 700$ V/760 Torr (0.92 V/Torr) and E/P $= 3000$ V/760 Torr (3.94 V/Torr) (Shultz 1976). Essentially, this states that increasing field cage bias beyond a point (which will depend on the pressure) should have little effect on the energy resolution and only increase the speed at which the ions drift across the IC toward the anode pads. It should be noted that the safe field cage and coplanar biases are pressure dependent, which means at a lower pressure, a lower field cage bias must be applied.
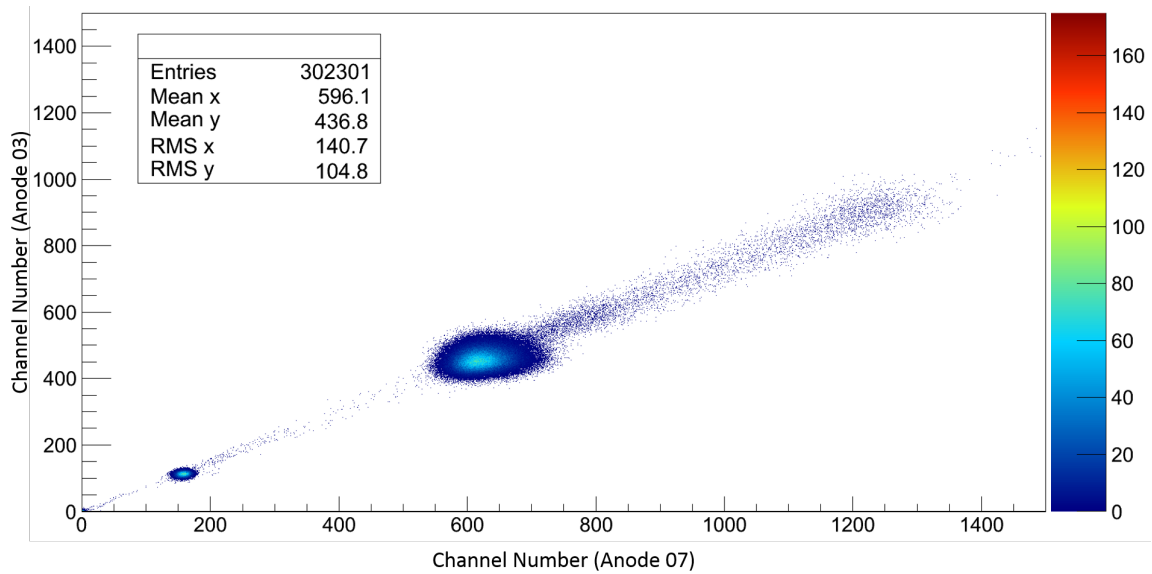
Figure 4.16: Taken with a 7*A* MeV ^{40}Ar beam, a 2-dimensional histogram of anodes 03 (abscissa) and 07 (ordinate) plotted against one another. The z-axis, represented by the colour scale, shows the number of events per pixel. Here, the main cluster (centered roughly at channel 600) is produced by ^{40}Ar while the smaller cluster at channel 160 is the ^{18}O contamination (section 4.7). This shows significantly more pileup as when compared to the ^{18}O plot and its less regular shape shows a worse correlation in peak position and size than the ^{18}O alone, likely caused by broadening due to ADC peak addition (section 4.8), more energy loss between anodes, and a higher amount of energy straggling because of a greater Z value.

Therefore, changing the field cage bias voltage did not significantly impact the energy resolution of the detector unless it was biased either with a voltage relatively close to that of the coplanar anode bias voltage or a bias that was too small for it to create the necessary electric field gradient to allow for the electron transport. The field cage bias voltage did, however, have a small effect on the energy resolution, which was measured and calculated in order to find an optimal value. Interestingly, the effect of the field cage bias, though small, did change with the beam species. At 19.5 Torr, the field cage was biased to -400 V, -500 V, and -600 V. Plotted in figure 4.17 are the best resolutions achieved for each field cage voltage setting by adjusting the coplanar anode for both ^{18}O and ^{40}Ar. The trend here is a roughly linear decrease in percent energy resolution as a function of field cage bias voltage. The change in resolution, however, is so small as to be negligible on a practical scale as the difference in resolution when changing the bias voltage by 50% (from -400 V to -600 V) is only about 0.05%. With an optimal energy resolution close to 5% for ^{18}O and 7% for ^{40}Ar, the IC is insensitive to such a small variance. There is little difference between ^{18}O and ^{40}Ar other than lower resolution in the ^{18}O data (in this plot, the ^{18}O data was taken using a two anode configuration as opposed to the single anode configuration used with the ^{40}Ar data). As to why the ^{18}O data does not follow the linear trend seen in ^{40}Ar is unknown; it likely has to do with an unoptimized coplanar anode bias voltage, however.

4.5   Coplanar anode bias voltage

The physics of both the coplanar anode and the field cage dictates that as long as the field cage is at a high enough bias voltage to move the electrons in the right direction, the major contributing factor to the overall energy resolution of the IC should be the coplanar anode. Therefore, varying the bias voltage of the coplanar anode should have a large impact
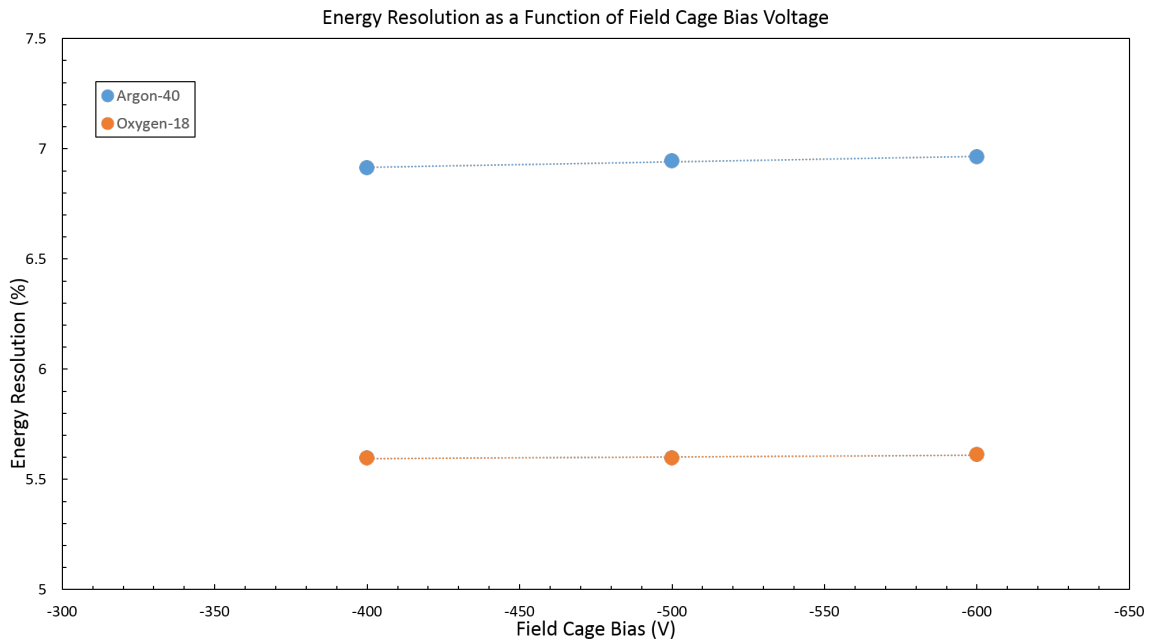
Figure 4.17: The effect of field cage bias voltage on energy resolution was measured using various beam species. It was varied between -400 V and -600 V, with the best results generally being at the highest voltages. The orange data set represents the oxygen beam with two anodes added, while the blue data set represents argon with a single anode. Here to coplanar bias voltage was chosen so as to give the best results with each particular field cage bias voltage. The trend line on each set of data shows that they are not only linear, but have a small slope.

on the resolution of the IC compared to the field cage (see section 2.3.4 for a more detailed explanation of how the coplanar anode and the field cage influence the electric field within the IC and how they interact with one another). In practical use the coplanar anode should be held at a voltage that is negative compared to the anode pads and thus serves as a focal plane, directing the ionized electrons, which are already moving under the influence of the field cage, onto the anode strips. This was simulated using GARFIELD in order to see the effect of the particle beam being offset by even several millimetres (figure 2.16). GARFIELD uses Monte Carlo methods to calculate the path of each electron individually.

The coplanar bias voltage was adjusted with varying field cage bias voltages and beam species. When the coplanar bias voltage was set to a bias over half of that of the field cage bias voltage it lost its ability to properly focus the electrons onto the anodes pads as the electric field generated by the field cage began interfering with the electric field generated by the coplanar anode (see figure 4.18, which shows that the energy resolution as a function of the coplanar bias voltage changes drastically when the bias voltage gets below a critical lower threshold value). A high coplanar bias voltage also has the effect of distorting the gradient made by the field cage, which is complex and would require further simulations to understand fully. Beyond the extreme regimes of a small or large bias, the electric field created by the coplanar anode was shown to have only a minor effect on the overall energy resolution of the IC, as it rose quite gradually at values near the minimum before blowing up at either extreme, even as the field cage bias was varied between -400 V and -600 V. This causes the curve of energy resolution as a function of coplanar bias to behave somewhat quadratically, with a distinct minimum and sharp rises once the values for bias voltage get too low or too high. This effect was measured using both the ^{40}Ar and ^{18}O beams. Interestingly, the optimal value of the coplanar bias was found to be species dependent.

It is also interesting to note the relationship between best resolution with the coplanar
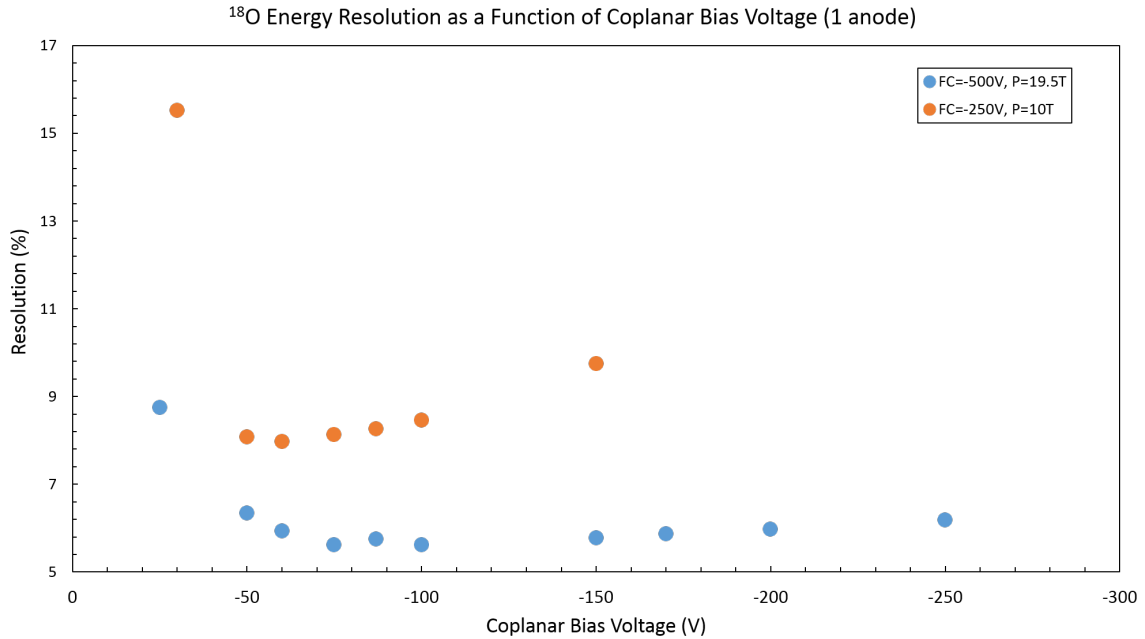
Figure 4.18: This data was taken with an ^{18}O beam at 5.72A MeV and measures the effect of the coplanar bias voltage on the energy resolution of the IC. As one can see, in the extreme regimes of very high (the voltage applied to the coplanar anode is comparable to that applied to the field cage) and very low (the voltage applied to the coplanar anode is too low to properly focus the electrons onto the anode strips) coplanar bias voltage with respect to the field cage voltage the resolution is very poor compared to the minimum and the values immediately surrounding it, wherein there is little change in the energy resolution. The blue data set represents an isobutane gas pressure of 10 Torr, which is why overall their resolution is appreciably lower than the the orange set, which represents a gas pressure of 19.5 Torr.

bias and the field cage bias voltage. Though they follow very similar patterns, the highest field cage has been shown to produce a slightly better energy resolution overall. The change, however, is so small that in practice it would be unnoticeable (see section 4.6). The energy resolution of the IC plotted as a function of coplanar bias voltage is shown in figures 4.18 (^{18}O) and 4.19 (^{40}Ar). One can see that the values are beam specific, but follow similar trends, with higher pressures allowing for a much more gradual increase near the minimum.
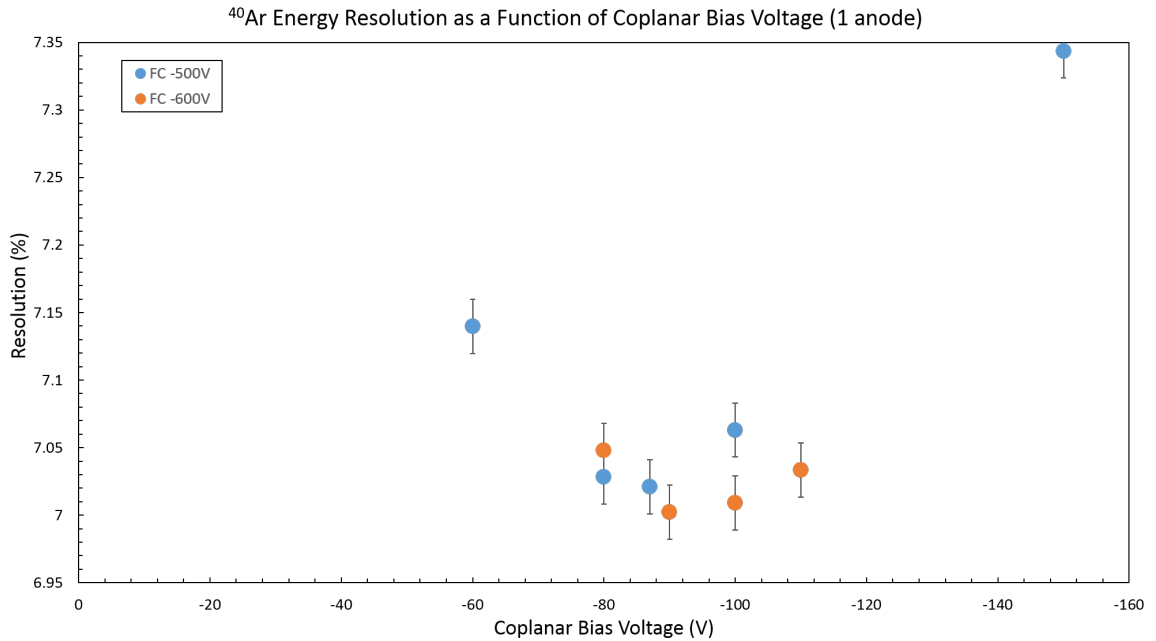
Figure 4.19: This data was taken with an ^{40}Ar beam at 7A MeV with a gas pressure of 19.5 Torr, and measures the effect of the coplanar bias voltage on the energy resolution of the IC. As one can see, in the extreme regimes of very high (the voltage applied to the coplanar anode is comparable to that applied to the field cage) and very low (the voltage applied to the coplanar anode is too low to properly focus the electrons onto the anode strips) coplanar bias voltage with respect to the field cage bias voltage, the resolution is very poor compared to the minimum and the values immediately surrounding it, wherein there is little change in the energy resolution. The orange data set represents a field cage bias of -600 V, whereas the blue set represents a field cage bias of -500 V. This was done in order to show that the varying the field cage voltage has little effect on the overall energy resolution.

4.6 Field cage bias to coplanar bias voltage ratio

The optimal field cage bias to coplanar bias voltage ratio (FC/C) was studied under various conditions. It was determined that the optimal ratio, which changes as a function of gas pressure, is species independent. In GARFIELD simulations run on the IC prior to our studies, the optimal ratio of field cage to coplanar anode was shown to be approximately 3 at 7.5 Torr. The measured optimal ratio varied with the gas pressure. This is based on the physical principle that the resolution varies as function of $\sqrt{n}$ (where n is the number of particles ionized). Therefore, if the pressure is halved so too is n, which follows from $PV = nRT$ (see equation 4.8 and section 4.10). For both species used (^{18}O and ^{40}Ar) the optimal ratio of FC/C was roughly the same at the same pressure (see figure 4.20); the optimal ratio of FC/C for 19.5 Torr was ≈ 5.7, whereas for 10 Torr was ≈ 4. As $5.7 \approx 4\sqrt{2}$ and $19.5/2 \approx 10$, this follows from the effect of halving n. Essentially, if $FC/C = \gamma\sqrt{P}$, where γ is a proportionality factor, then using 19.5 Torr and the optimal $FC/C = 5.7$, $\gamma \approx 1.29$ and with 10 Torr FC/C with the same γ is 4, in agreement with the observation. This is also close to but not in exact agreement with the GARFIELD result; the small deviation is likely caused by GARFIELD only using mock geometry of a single section.

The optimal ratio of FC/C, independent of field cage and coplanar bias or anode configuration, always had the same minimum value and roughly followed the same trends as when the coplanar anode was varied and plotted against energy resolution. When the FC/C ratio is plotted against energy resolution, as seen in figure 4.21, the minimum value, independent of field cage bias, is between 5.5 and 5.8. Likely the reason that the minima do not perfectly match is due to the slightly different bias voltage ratios that were plotted (unfortunately we did not ensure the same ratios were used for different species and pressures) and not due to an actual physical difference. In future experiments, this should
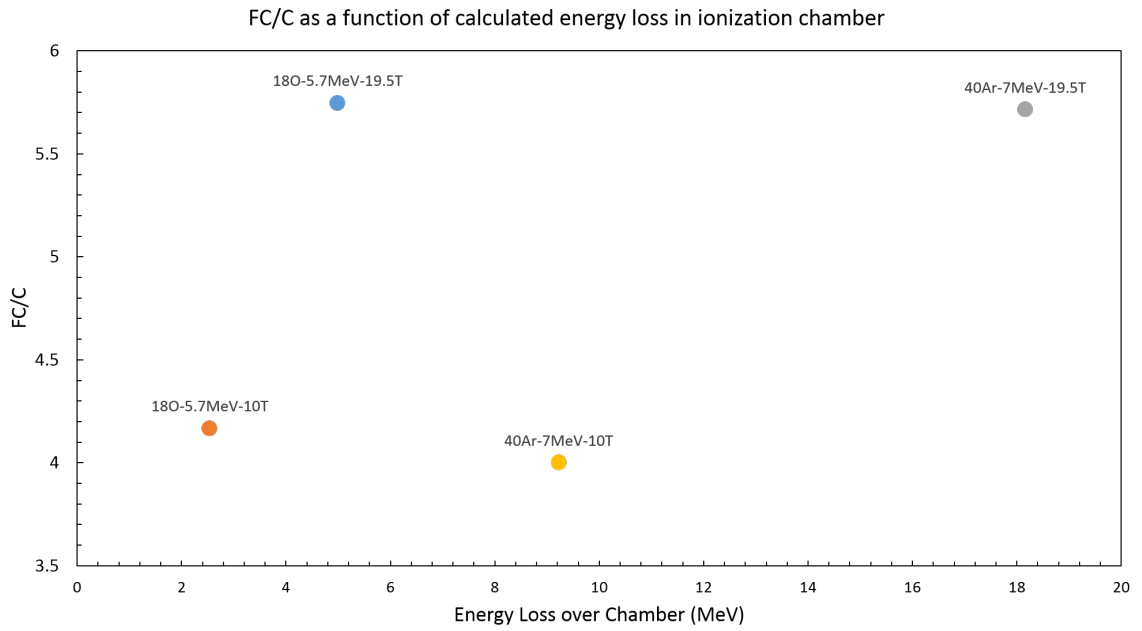
Figure 4.20: Optimal FC/C as a function of calculated energy loss in the IC. For either beam species (^{18}O and ^{40}Ar) the ratio was roughly the same: $FC/C \approx 5.7$ for 19.5 Torr and $FC/C \approx 4$ for 10 Torr. Thus the optimal ratio varies only with the gas pressure in the IC and not the beam species, despite the optimal coplanar and field cage voltages being dependent on the type of ions within the particle beam.
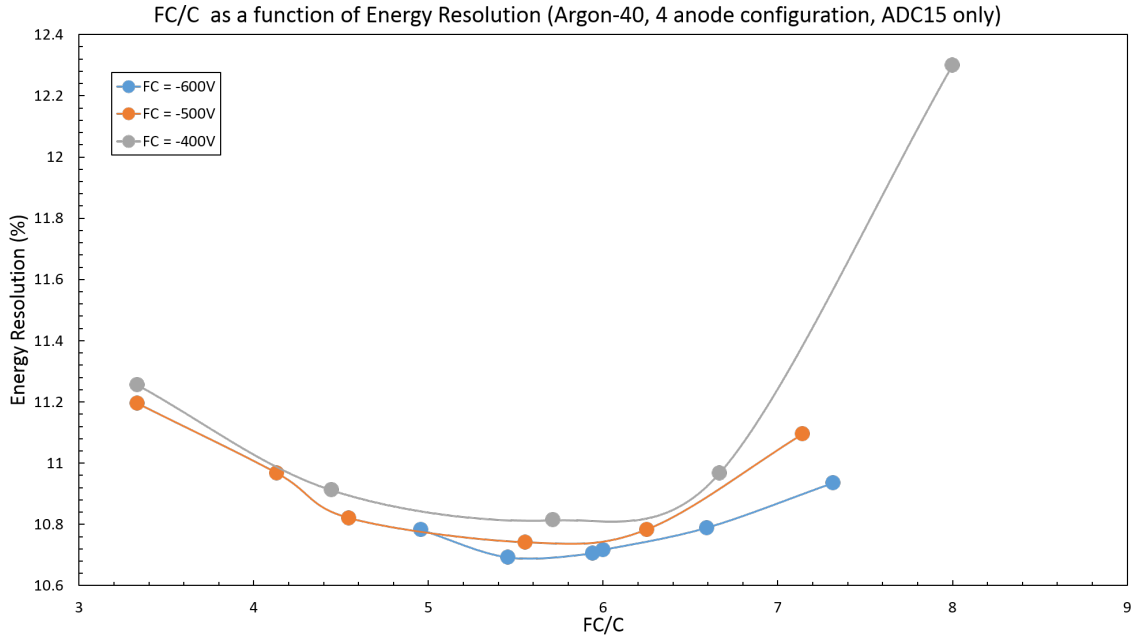
Figure 4.21: FC/C is plotted against energy resolution for a single anode out of a 4 anode configuration. Here, the blue data set represents an field cage value of -600 V, the orange data set represents an field cage value of -500 V, and the grey data set represents an field cage value of -400 V. The minimum of each set of points is between 5.5 and 5.8.

be measured exactly.

As stated in section 4.3, there is a discrepancy between the signals from the outer two anodes (01 and 15) and the signals from the 14 inner anodes. In order to test whether or not this was an effect of the field inside the chamber or another process altogether, the signal produced by the outer anodes was scaled to the signal produced by the middle anode, anode 07 (it should be noted that this was done with an eight anode configuration as opposed to a 16 anode configuration, which would have been ideal for this test; there was no 16 anode data taken during these studies). This scaling factor was then plotted as a function of the ratio FC/C. If the line produced in the plot was not flat, it would suggest that the electric field inside the chamber, which is produced by a combination of the electric fields created by field cage bias and the coplanar anode bias voltages, is having an effect on the outer
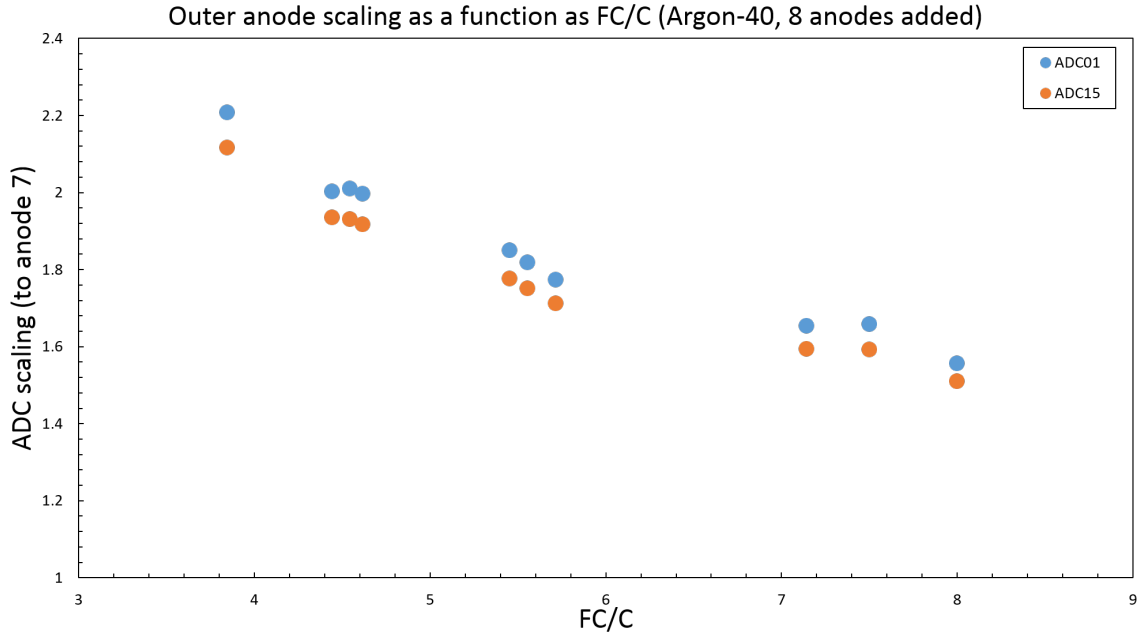
Figure 4.22: The scaling factor of the signal produced by the outer anodes (01 and 15) to anode 07 is plotted as a function of FC/C. As there is a general trend that is not flat, it shows that the electric field within the IC, created by the interaction between the field cage and the coplanar anode, are affecting the electron collection at the fringes. The blue data set are the points from anode 01 while the orange data set are the points from anode 15, which have a slight gain difference, but show that is this effect is acting roughly symmetrically on both sides of the anode strip in the IC.

anode's ability to collect electrons. This plot is shown in figure 4.22. It indicates that there is indeed a fringe effect in the electric field created by the interaction of the field cage and coplanar anode that is affecting the electron collection (and thus pulse amplitude) at the outer anodes when compared the inner anodes.

4.7 ^{18}O contamination

The ^{40}Ar beam was run immediately after beam of ^{18}O, which, from the ion source used, led to a contamination of ^{18}O. This is significant due to the purpose of the IC, which
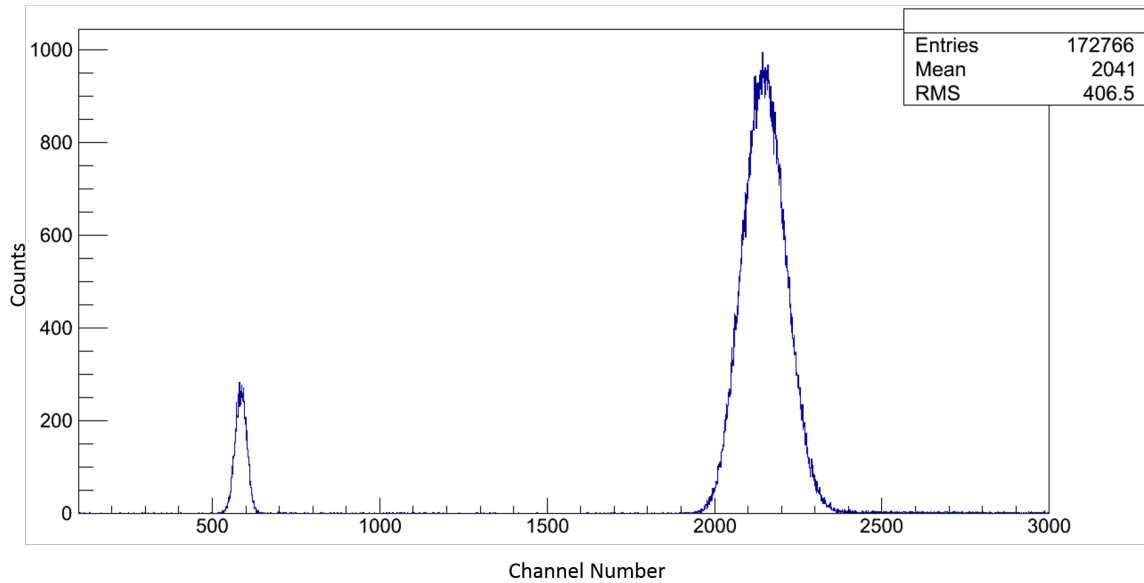
Figure 4.23: Taken at a single anode configuration with optimal IC settings, the small peak on the left is the contamination of ^{18}O whereas the large peak on the right is ^{40}Ar. The separation of these two peaks is a good indicator, along with the energy resolution, of the ability of the IC to determine the Z value of contaminants in the beam.

is to isobarically filter isotopes of similar Z values, as it allowed for a study with multiple ions in the particle beam. The spectrum in figure 4.23 shows the small amount of ^{18}O contamination (left) in the main ^{40}Ar beam (right).

From spectra like that shown in the figure 4.23, the separation between the two peaks can be calculated, which along with the energy resolution, is a good indicator of the how well the IC will function when used to filter isobars of similar Z values. Here, at an energy of 7A MeV, ^{18}O has lost 4.4 MeV across the chamber, whereas the ^{18}Ar has lost 19.32 MeV (according to the energy loss calculations, which are shown in appendix A). These losses correspond to peak mean values at channels (after pedestal subtraction) 563 and 2128, respectively. The separation between the two peaks is thus 1565 channels. Given that the energy resolution of the ^{18}O peak is on the order of 5%, this result is promising.

Therefore, assuming spacing based on Z^2 between each successive nuclide, there should be no problems distinguishing isobars.

Calculated using LISE++, at a pressure of 19.5 Torr, a beam of ^{18}O at 6A MeV loses 4.8 MeV in the IC after passing through 900nm Mylar entrance windows whereas a beam of ^{18}F at 6A MeV loses 6.0 MeV in the IC after passing through the same entrance window. These isobars have a difference of 25% in energy lost within the IC, which should be easily resolvable at a 5% energy resolution. ^{40}Ar, with its current 7% energy resolution, at 6A MeV loses 21.1 MeV across the chamber after passing through the 900 nm entrance window at a pressure of 19.5 Torr, whereas its adjacent isobar ^{40}K loses 23.1 MeV across the chamber under the same conditions. This is a difference of 9.2%, which may be distinguishable. The 7% energy resolution of argon can likely be reduced, as well (see section 4.8).

In order to verify these calculations one can look at the ratio of the ^{40}Ar to ^{18}O contamination in the 7A MeV beam and compare that to the ratio of energy loss calculated by LISE++ (shown in appendix A). While the measured ratio of ^{40}Ar/^{18}O peak potions is ≈ 3.65, the calculated ratio is ≈ 4.25. This discrepancy may stem from a number of causes, including the charge collection problems in the outer anodes or the unknown broadening contributors which may be causing the peaks to shift.

4.8   ADC gate width

Many factors contributed to finding the optimal efficiency settings of the IC, one of which was the width of the ADC gate used while taking data. The gate width affected the signal in two ways: as it widened it caused an appreciable high-energy shift in the peak position of the pulse output from the IC (figure 4.24) and larger gate widths were causally

related to the size of a second, non-physical peak, which did not correspond to the peak due to pileup (figure 4.25), and whose integral counts grew as a function of the width of the ADC gate. It was discovered that both these effects were products of the particular ADC being used, the peak sensing Mesytec MADC-32. Strangely, if two pulses of nearly identical height enter the gate while it is open, the ADC has a tendency to combine the pulses together in some unknown manner, which causes it to output both the physical peak produced by the radiation and a second, higher energy non-physical peak. The smaller, nonphysical peak in figure shown 4.25, was ruled not to be pileup due to its position relative to the main physical peak (the pileup peak should be at twice the energy level, which this was not). This was especially clear as it grew as a function of the beam rate, as is shown in section 4.8.1 (in figure 4.25 all variables are held except for a widening ADC gate, which was changed in order to increase the prominence of the second peak). This phenomenon was tested with the pulser, the ^{241}Am alpha source and the ^{40}Ar and ^{18}O beams and found to be independent of beam species and a sole property of the ADC.

The main problem introduced by the combination of peaks within the gate by the ADC is a more severe rate dependence: while ^{18}O produces a distribution that has a small enough energy resolution for the second peak created by the ADC to be distinguishable from the physical peak, as in figure 4.25, with a heavier beam (like ^{40}Ar) that deposits considerably more energy in the IC, the distribution is broader, which results in, at high rates, the physical and nonphysical distributions, interfering with one another. This in turn causes a deviation in the expected normal distribution caused by an asymmetric, high energy broadening. The results of this broadening are shown in figure 4.26, in which the same effect that causes the double peak seen in figure 4.25 is shown only to broaden the energy distribution produced by ^{40}Ar. This broadening due to the electronics, along with increased energy straggling, is a contributing factor to why ^{40}Ar has been shown to have a significantly poorer energy

resolution than ^{18}O (about 7% for ^{40}Ar in ideal cases, as opposed to 5% for ^{18}O) despite depositing more energy in the IC. Something important to be noted about the ADC gate width is that the MADC-32 is used to generate the gate for all of the detectors on IRIS. This means that despite the desire to have the smallest gate possible in order to avoid getting two pulses in the gate at the same time and the subsequent peak-adding problem therein, there is a minimum gate width that will accept all the signals necessary. This minimum was chosen to be 1 μs. In order to avoid signals from other detectors falling outside the gate, however, the ADC gate was set to 2 μs for the majority of these experiments. This problem with the ADC adds a rate dependence to the IC that would otherwise not exist.

4.8.1 Rate dependence

In order to test how the IC performs under extreme beam rates (both high and low), spectra were examined over four orders of magnitude of count rates within the IC, from roughly 10^1 counts per second to 10^5 counts per second. With the alpha source being the lowest, at about 10 counts per second, and the beams of ^{18}O and ^{40}Ar being controllable with much higher average rates. At low rates ($<$ 5000 counts per second) the IC functions ideally and the spectra do not show any indications of pileup. At high rates ($>$ 5000), however, pileup becomes an increasingly large factor. Figure 4.27 shows a comparison between the spectra in the IC with the bias voltage of the field cage and coplanar anode and ADC gate width held constant (at 2 μs), but a changing beam count rate. Figure 4.27(d), especially, shows 20000 counts per second being an non-ideal case for the IC. This would suggest that beam rates below 5000 counts per second are preferred. This is only looking at a single anode, and as the chamber is multi-sampling with 16 independent anodes, cases of pileup can be reduced. It should be noted, however, that pileup does not appear to be considerably affecting the distribution produced by ^{40}Ar as even in the most extreme cases,
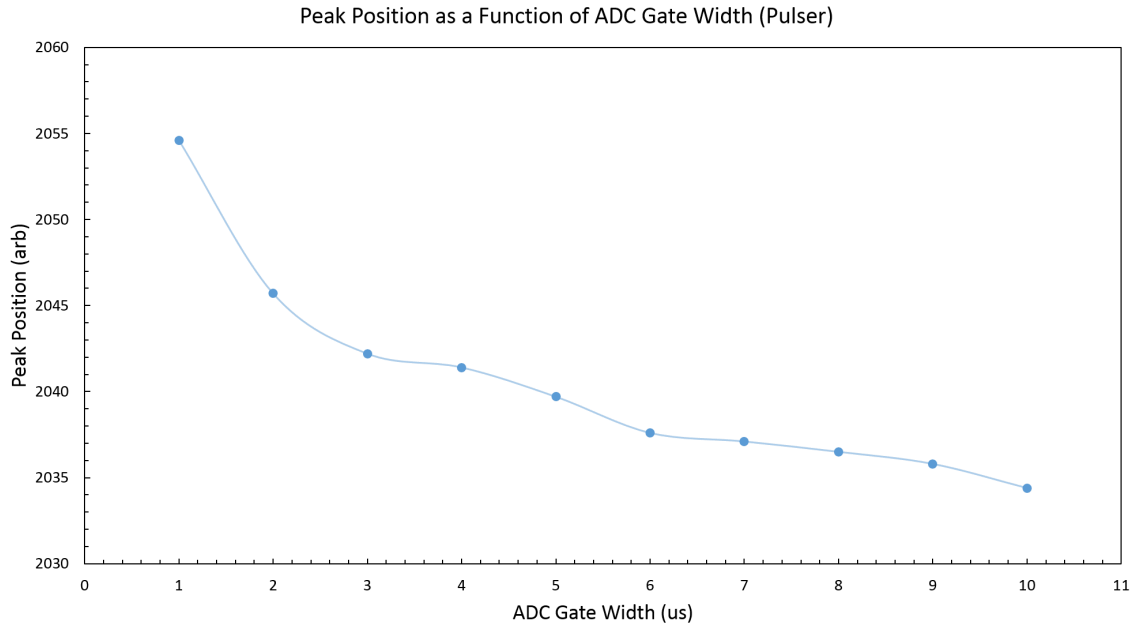
Figure 4.24: Using a pulser in order to eliminate any sources of uncertainty in charge collection, the ADC gate width was shown to effect the peak position of distributions produced. This is solely due to the electronics and has no physical cause. The reason that this is known to be caused only by the electronics is that the pulser has no interaction with the physics of the IC; it pulses the preamplifiers directly, bypassing the anodes or anything related to charge collection. Shown here, a single ADC channel is being pulsed with the only changing variable between runs being the width of the ADC gate (from 1 μs to 10 μs in 1 μs intervals). Given that the MADC-32 is a peak sensing ADC, there should be no change in peak position, regardless of whether or not multiple peaks fall within the gate while it is open. Since using a larger gate creates a higher chance of two pulses being in the gate at the same time, however, the shift in pulse amplitude output by the preamplifiers makes sense (given that the ADC combines pulses together when two of them fall in the gate at the same time). From this, one can easily discern why this would cause a broadening effect in an already broad peak, such as ^{40}Ar assuming that the distributions fall within a few percent of each other. In order to allow for multiple pulses to fall within the gate at any given time, the pulser was set to send pulses at a random time, as opposed to regular intervals.
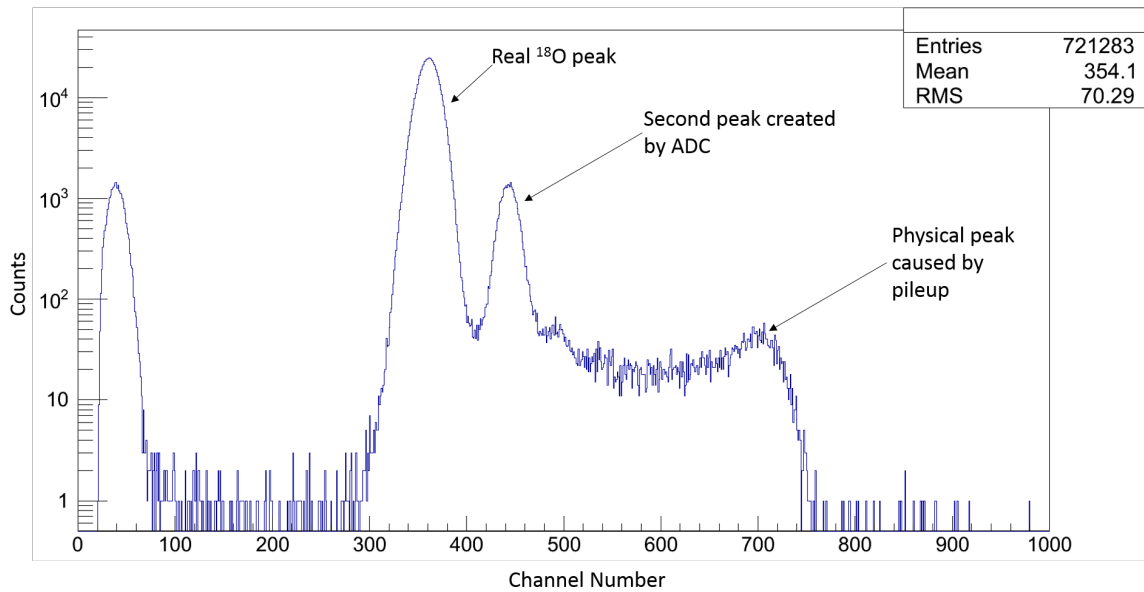
Figure 4.25: Shown on a log scale, the large peak (left) is the actual signal produced by ^{18}O while the smaller peak directly to its right is a nonphysical peak, which is an effect of the MADC-32 and the gate width used. The peak caused by pile-up, which should be centered around twice the mean value of the real peak, is shown at roughly channel 700, thus showing that the second peak, which is produced by something nonphysical is caused by the way in which the ADC handles two pulses in its gate at the same time. This data was taken using a 10μs gate width.
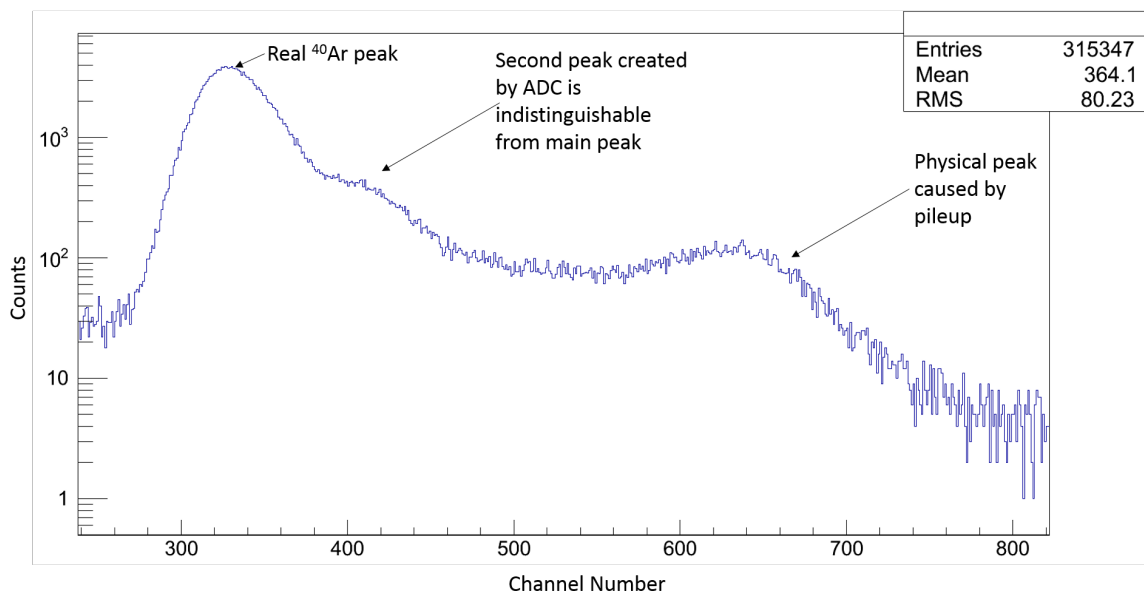
Figure 4.26: An ^{40}Ar signal, shown on a log scale, in which the main, physical distribution is broadened by overlapping with a second, non-physical distribution created by the ADC. This is clearly distinguishable from the physical second peak caused by pileup, which lies at roughly double the channel position of the true peak.
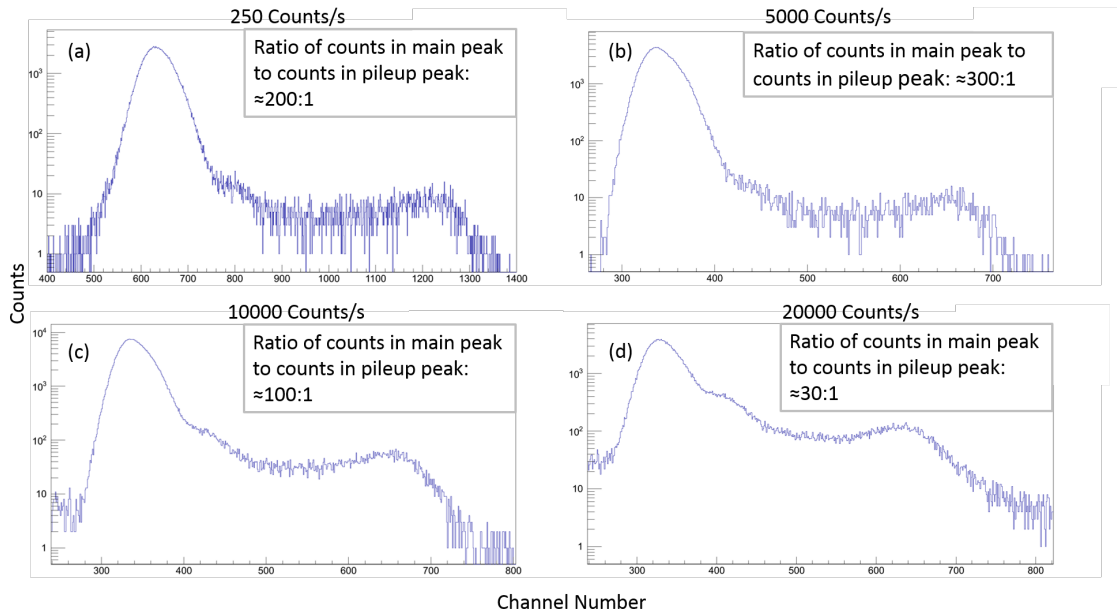
Figure 4.27: Showing the changing in the spectra produced by the IC with beam rates over three orders of magnitude, from 250 counts per second (a) to 20000 counts per second (d) in the IC. All of these spectra were taken at a gate width of 2 μs and a constant field cage and coplanar bias voltage. In figure (b) broadening of the peak is beginning to take hold and its Gaussian shape has begun to skew, especially when compared to (a). (c) and (d), however, are showing both major signs of pileup and peak broadening due to reasons stated in section 4.8. The peak due to pileup is the hump at twice the channel number of the main peak whereas the nonphysical peak produced by the ADC is much harder to distinguish as it is close enough to the main physical distribution to be within the limits of the energy resolution of IC for ^{40}Ar.

the integral counts in the pileup distribution and tail are less than 5% of those in the main peak. The asymmetric broadening that begins in figure 4.27(b) and grows throughout (c) and (d) is likely caused by the ADC peak addition outlined in the previous section. This becomes an increasingly large factor as the beam rate increases, with the 250 counts/second showing no signs of asymmetry. If the MADC-32 continues to be used, further study is necessary in order to mitigate this problem in future experiments.
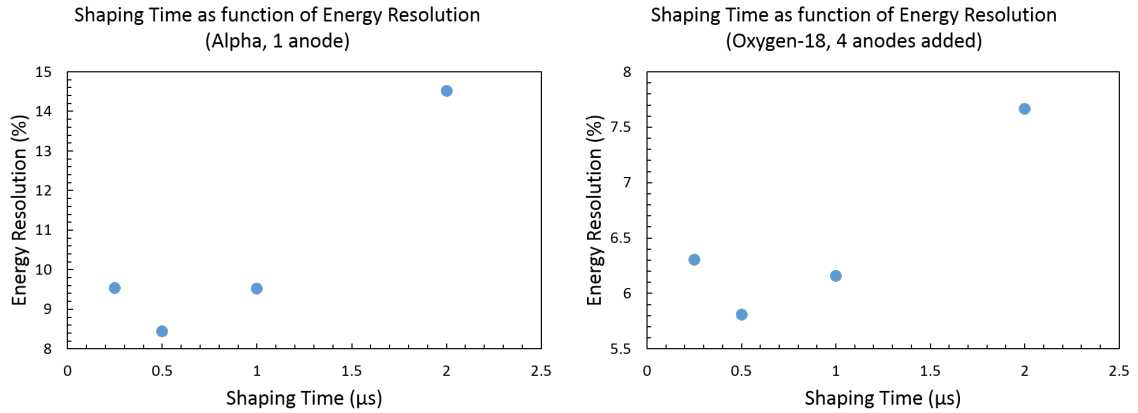
Figure 4.28: The effect of shaping time on the energy resolution of the IC was measured using various beam species. A minimum in the energy resolution was found consistently at 0.5 μs. Shown here, the optimal shaping time is independent of species, as one would expect. Though here only ^{18}O and the ^{241}Am alpha source are shown, ^{40}Ar exhibited the same trend.

4.9 Shaping time

After the signal is collected by the anodes and travels through the preamplifiers, it is sent through a Mesytec MSCF-16 shaping amplifier. This shaping amplifier can operate with four different shaping time settings: 0.25 μs, 0.5 μs, 1 μs, and 2 μs. Each of these were studied with the ^{241}Am alpha source and the ^{40}Ar and ^{18}O beams. This was done in order to observe the effect that shaping time had on the overall energy resolution of the detector. As shown in figure 4.28, the shaping time was shown to have a large effect on the overall energy resolution of the IC (as it changed by over 6% depending on the shaping time used) and was shown to have a consistent minimum at 0.5 μs across various beam species and energies thus making the optimal shaping time setting 0.5 μs.

4.10 Effects of gas pressure on IC signal and energy resolution

The IRIS IC is capable of operating in various gas pressure regimes. As it is designed only for particle identification and to take the least amount of energy out of the beam possible in order to do so, this is a necessary operating condition. Therefore, depending on the beam species and energy, different gas pressures may be required to achieve the desired results. Depending on the beam species, the pressure can be lowered to reduce energy loss; the minimum pressure is thus dictated by physics (that is to say, how much ionization is possible at a given gas pressure with a particular beam species) and noise conditions, and not the design of chamber itself. The maximum pressure of the IC, however, is governed by the strength both the entrance and exit windows, the regulations of the gas flow system, and most importantly, the energy loss in the IC caused by higher gas densities and more subsequent ionization. Thus the IC was operated with isobutane gas pressures of 19.5 Torr and 10 Torr. The effect of gas pressure on the signal strength is fairly straightforward: the effective resolution as it relates to pressure is governed by a proportionality factor of $\sqrt{n}$ (where n is the number of electrons collected by an anode), which means that if one is to half the pressure, the resolution will change by a factor of $\sqrt{2}$. This is shown simply in equation 4.8:

$$PV = nRT$$
$$\therefore (\tfrac{1}{2}P)V = (\tfrac{1}{2}n)RT \tag{4.8}$$
$$\longrightarrow \xi = \frac{2.35}{\sqrt{n}} = \frac{2.35}{\sqrt{\frac{1}{2}}}.$$

Experimentally, this proved true and this relationship is shown in the plot in figure 4.29, where the blue data set represents the energy resolution calculated from signals at 19.5 Torr
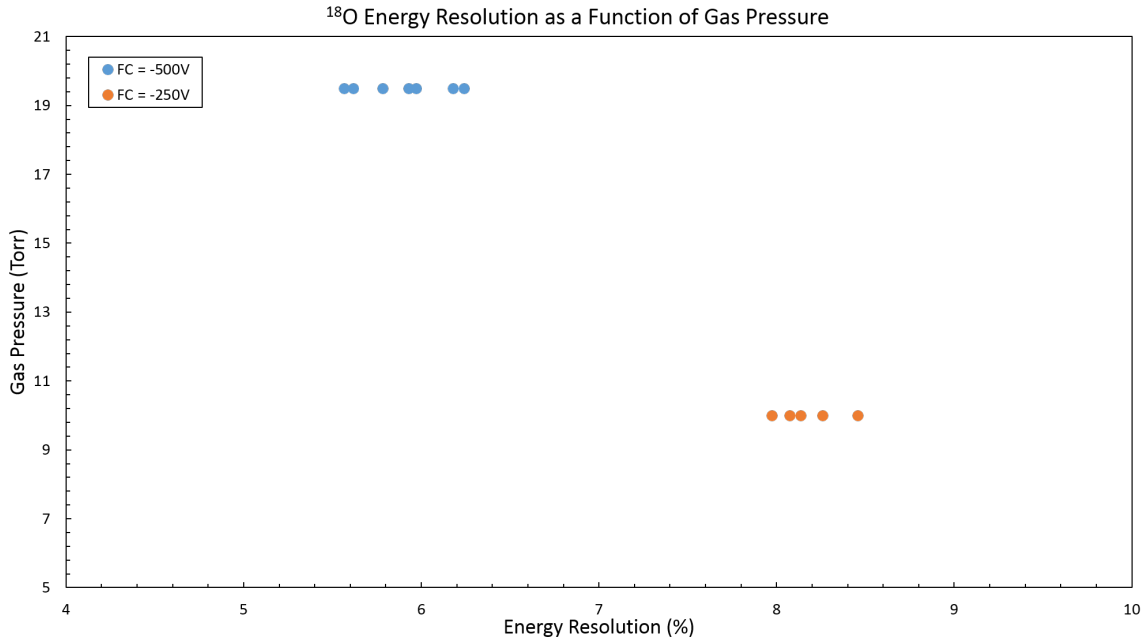
Figure 4.29: As expected, the energy resolution changed with the square of the ratio of pressures ($\sqrt{n}$). Shown in blue are data taken at 19.5 Torr where the energy resolution clusters around 6% and in orange are data taken at 10 Torr, which clusters between 8% and 9%. This is a difference of approximately $\sqrt{2}$. This data was taken using an ^{18}O beam at 5.72*A* MeV.

and the orange set is taken from signals at 10 Torr. The blue data set is clustered between 5.5% and 6% while the orange data set is clustered between 8% and 9%. The quotient of the average of these clusters is approximately $\sqrt{2}$, as expected.

Between 19.5 Torr and 10 Torr the peak position was roughly halved (by channel number), as would be expected, as the signal should change linearly as a function of pressure given that n has halved. This is shown in figure 4.30 where the peak positions of two sets of data are plotted as a function of pressure. The average peak position of those plotted at 19.5 Torr is 636 ± 38, while the average of those plotted at 10 Torr is 298 ± 22. Though this is not exactly half, one should not expect it to be as these points are not taken at directly half the field cage and coplanar bias voltages and 10 is not exactly half of 19.5.
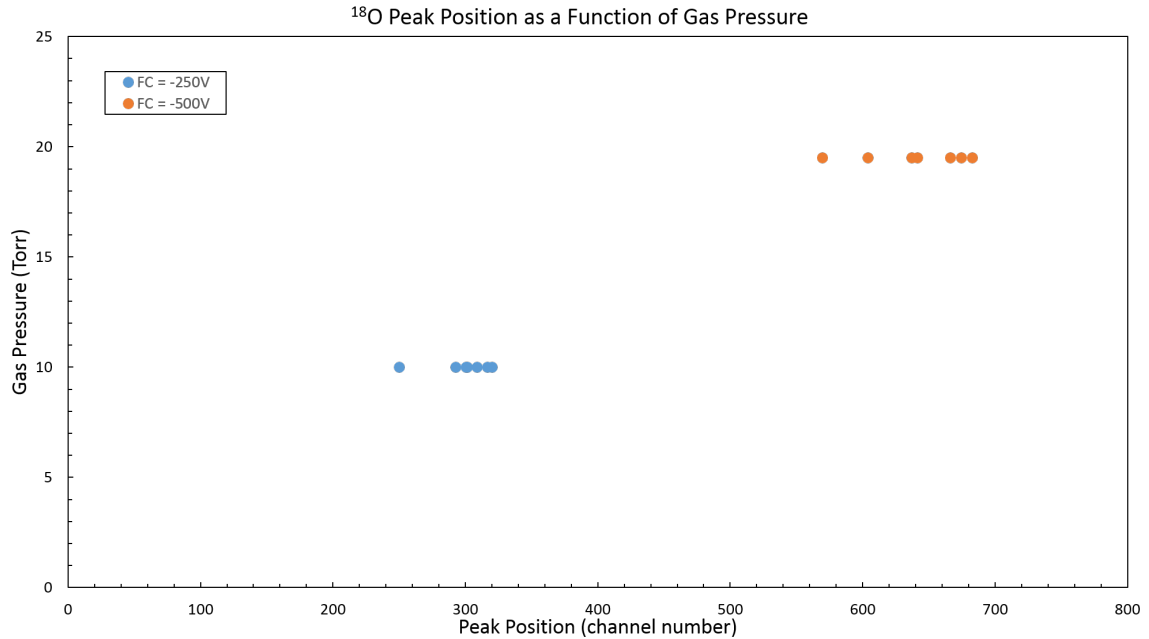
Figure 4.30: The peak position changes as a function of pressure. Shown here are the pedestal subtracted values where the orange data set (at 19.5 Torr) is plotted alongside the blue data set (10 Torr). The blue data set is at roughly half the value of the orange set, which is at half the pressure, as expected.

Regardless, the ratio of $(636 \pm 38)/(298 \pm 22)$ is equal to the ratio of $19.5/10$, within uncertainty.

4.11 SRIM beam profile simulations

As a simple test of how much the IC affected the particle beam profile, some basic simulations were run using SRIM (Ziegler 2013). This was done in order to check if any of the beam was not passing through both the entrance and exit windows. Given that the windows are 6 mm in diameter and the beam spot is about 3 mm across, it appears, from these simulations that a vast majority of particles are passing through the chamber with their trajectories largely unaltered. The results of these simulations are shown in figure
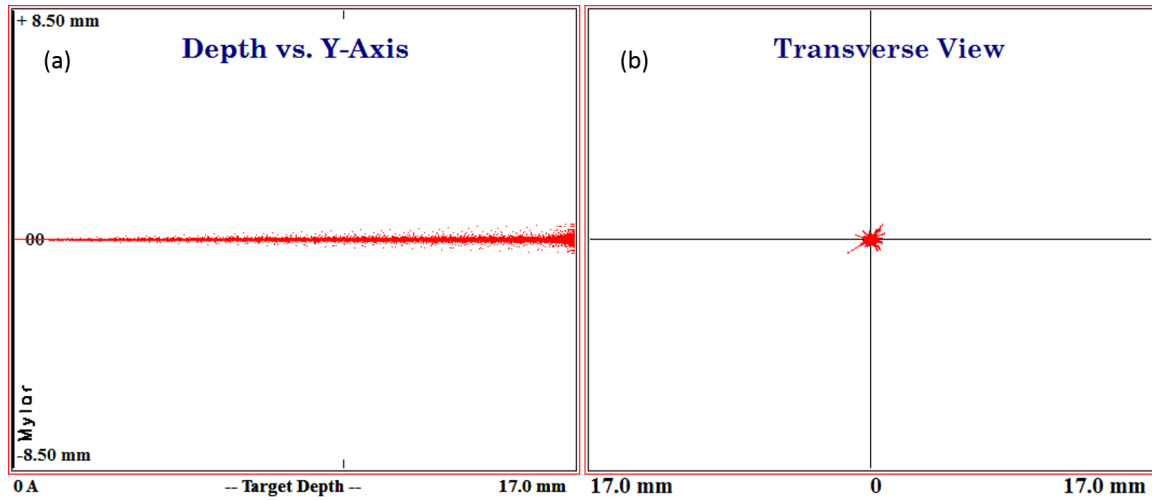
Figure 4.31: Figure (a) shows the deflection of the beam (represented by the red lines) as it passes through the chamber, while figure (b) shows the same simulation from a transverse perspective (looking directly at the beam). From these simulations, the deflection and dispersion of the beam as it passes through the IC are shown to be negligible.

4.31, where the red lines represent a single particle from the beam. 10^5 particles were run in this simulation and the maximum deflection was less than a millimetre.

Chapter 5

Discussion and Conclusions

5.1   IRIS IC design

The particular design choices behind the IRIS IC are integral to its operation, especially its anode strip and coplanar anode. The pertinent question surrounding the design choices behind IRIS are: whether or not they allow for sufficient energy resolution, and if the IC can make adequate measurements with the minimal amounts of energy deposited in it. The question of whether or not the design allows for adequate energy resolution in order to determine beam contaminants with $Z = \pm 1$ from the desired nuclide has been experimentally verified under the operating conditions of the studies conducted. With heavier ions, however, the energy resolution will likely become worse and more study is needed in these regimes. ^{40}Ar, for example, had an optimal energy resolution of 6.5%. Thus from the knowledge available, it is likely that the IRIS IC should adequately be able to isobarically filter the particle beams studied to a resolution of $Z = \pm 1$.

The answer to the final question, as to whether or not the energy loss in the chamber is sufficient for the chamber to make adequate measurements, is fairly straightforward:

currently with the Mylar windows, which will be replaced with much thinner silicon-nitride windows that allow for less energy loss in the beam overall, the energy loss in the chamber is more than sufficient to make the measurements necessary and it is not great enough so as to affect the physics at the target. In this respect, the design of the IC has proven highly effective.

5.2 ADC and shaper

The electronics used for signal processing on the IC have been shown to have a fairly large impact on the overall energy resolution that can be achieved in signals from the IC. The shaping time was shown to cause a variation by over 6% in the overall energy resolution depending on which time was selected, and the width of the ADC gate had an effect on both peak position and energy resolution. The cause of the ADC's impact on the signal from the IC has been discovered (see section 4.8), but it is important to note that though the smallest gate possible is desirable from a the perspective of the IC, because that same gate is used for all detectors in IRIS 2 μs appears to be ideal. The peak addition problem, however, may cause problems with heavier beams and higher beam rates unless another ADC is considered as the gate cannot be set much smaller than 1 μs due to the 0.5 μs shaping time. As the second peak created by the ADC appears to be within the threshold of the energy resolution of these heavier beams, which have a larger FWHM value due to energy straggling (for more information see section 4.2 and figure 4.26), the reduction in energy resolution may get worse with heavier ions. Further study, however, is needed in order to verify this. With a 2 μs, gate, however, the shaper's optimal setting of 0.5 μs can be used without a problem.

5.3 Effects of the field cage and coplanar anode on energy resolution

In and around the optimal range of operation for the IRIS IC, neither the field cage nor the coplanar anode bias had a significant impact on the overall energy resolution achieved. What is interesting is that the GARFIELD simulations run before the IC was experimentally tested showed an optimal field cage to coplanar bias voltage ratio of 3 at 7.5 Torr. Extrapolating from the experimental results presented in Chapter 4, however, indicates the optimal ratio is closer to 3.5 for a pressure of 7.5 Torr. This discrepancy is likely due to the mock geometry used in the GARFIELD simulations. Using these measured points, future experiments will not require optimization of voltage ratio, for as long as the gas pressure is known the ratio can be calculated by equation 4.8. Given that at 19.5 Torr the optimal FC/C is approximately 5.7 and at 10 Torr it is approximately 4. Therefore, a conclusion from this optimization study has provided an experimentally verified prescription to find the optimal voltage settings for the ratio of FC/C.

Individually, neither the field cage nor the coplanar anode contributed significantly to the energy resolution unless at extremes of the ratio of the two. The field cage was not tested at a low enough value to see when it would be begin to have a major effect by notably reducing the energy resolution. The coplanar anode, however, was run at extremes in order to observe its effects. The minimum coplanar anode bias voltage that can be used before causing a significant drop in energy resolution is about -60 V, and the maximum, which is determined by the field cage bias, is about 2:1 field cage to coplanar bias. This has broad implications on the operations of the IC as the field cage and coplanar bias voltages must be adjusted 1:1 in accordance with the change in pressure so as to ensure no sparks or other problems occur. As the IC will be operated at -500V in a 19.5 Torr environment, this

means that the chamber will not allow for pressures lower than 5 Torr, as that would force the field cage to operate at -125 V meaning the coplanar anode would have to operate at less than -60 V, which would result in a drastic loss in energy resolution. This can be corrected for by adjusting the maximum field cage bias voltage at that pressure, as tests have shown that at 3.75 Torr in isobutane, the field cage be biased up to -900 V before sparking in the high voltage connectors occurs. Though this ultra-low operating pressure is unlikely, for very heavy ion beams, it may be necessary to go to pressures within this regime in order to reduce energy loss. Further study is needed in order to see exactly how low one will have to go in order to compensate for the high Z values in heavy ion beams, especially once the Si_3Ni_4 windows are installed.

Most important to note is how well the coplanar anode and field cage, combined, worked to achieve the energy resolutions necessary for particle identification. The results here lend great credence to the future of the IC and to systems like this being used for similar purposes.

5.4 Outer anodes and FC/C ratio

The collection of ionized electrons throughout the IC is not uniform across the anode strip as there appear to be fringe effects associated with the electric field (produced by the interaction between the field cage and coplanar anode) that have an effect on the outer two anodes (00 and 15). This was verified by measuring the change in the signal in the outer anodes as a function of field cage to coplanar anode bias voltage ratio (see section 4.3.2). The full effects that the electric fields created by the coplanar anode and the field cage bias have on the collection at these fringe points, however, has yet to be determined and simulations as well as further experimentation are necessary in order to observe the full

extent of this problem. Current measurements have the outer anodes varying a between 2.2 and 1.6 times scaling factor to anode 07, depending on the field cage to coplanar anode voltage ratio (see figure 4.22). Ideally, this would be reduced to close to one. It should be noted, however, that the collection problems at these outermost anodes has little effect on the overall operation of the IC, and though a solution is important, it is not necessary for near optimal functioning of the IC.

5.5 Pressure relation to energy loss

As stated in section 5.3, the lower limits on gas pressure in the IC may serve to be an issue in future experiments (this is, however, an unlikely scenario, as it even with heavy ion beams it will not likely be necessary to operate the IC at or below 5 Torr). In the experiments run for this study, the pressure was adjusted between 19.5 Torr to 10 Torr, however, which was shown to have a major impact on the signal produced, as expected. Though a likely minimal pressure can be associated with the field cage and coplanar anode voltage, another pertinent question may be how low one can keep the pressure while maintaining a large enough signal to noise ratio. As the minimum energy necessary to produce a viable signal is about 0.13 MeV per anode, which for a beam of ^{18}O at $6A$ MeV is approximately 10 Torr, this suggests that, from energy loss calculations done with LISE++, for light ions the operation threshold will likely be closer to 20 Torr, depending on the specific ion chosen. Ideally the IC would always be configured in a 16 anode setup as it gives the highest energy resolution, reduces pile-up, gives the most data points across the chamber, and allows for each individual anode to be examined, and allows one to see reactions in the IC more readily. Yet, with lighter ion beams, especially at higher energies ($> 5A$ MeV) an eight anode configuration may be the ideal condition under which to operate the IC. For heavy

ions ($Z > 18$), however, the regime in which IRIS was specifically designed to operate, the IC should perform adequate isobaric filtration in a 16 anode configuration down to 10 Torr. Further study is necessary in these regimes in order to experimentally verify the extremes of the operating conditions for the IC.

5.6 Multi-anode configurations

The multi-anode system of the IRIS IC proved very useful for signal readouts. All symmetric anode configurations were tested, from one to 16 anodes. Other than the apparent collection issues at the outer anodes, which are likely due to fringe electric field effects, individually, the anodes performed well under a variety of conditions within the IC. The multi-anode design proved effective for its purposes, which were both to improve resolution over the addition of multiple additions, likely due to improved capacitance matching to preamplifiers for particular anode sections, as well as the reduction of pileup. The resolution was shown to improve nearly linearly as a function of the number of anodes used, which suggests that for future use, the maximum number of anodes available should be used in order to achieve the maximum energy resolution. It also allowed for energy loss tracking across the length of the chamber, which could be useful in future experiments. Taking measurements for which the IC was designed, the multi-anode design works exceptionally well and would be a recommended system for future designs of ionization chambers with similar purposes.

5.7 Final remarks

Studies on the IRIS IC have been successful in proving that both its design and functional purpose have merit. As with any new technology, however, the IC has presented

issues that must be solved in order to ensure the highest standards of operation in future experiments. The design goal of the IRIS IC is to isobarically filter ions with $Z = \pm 1$, which according to the measurements and calculations done over the course of these studies looks to be possible. In order to calculate the theoretical effects that energy straggling (likely the dominant cause of broadening in isotopes with a higher Z) may have on heavier isotopes in the IC one must first do an exact energy calibration. The current IC, with the charge collection issues does not allow for a simple energy calibration as it is unknown exactly how much energy is being collected by anodes. Thus extrapolating from the current measured data to a heavier ion of $Z = 30$ with optimal values of shaping time, ADC gate width, and field cage and coplanar anode bias voltage, an energy resolution of $\approx 8\%$ is predicted. As an example, ^{71}Zn should deposit 40.4 MeV in the IC and ^{71}Ga should deposit 42.5 MeV in the IC at 19.5 Torr and a beam energy of 7*A* MeV. This is a difference of 5%. Assuming an 8% energy resolution at $Z = 30$, these peaks should not be distinguishable (this assumption stems from the difference in energy resolution between oxygen ($Z = 8$) and argon ($Z = 18$), which are 5% and 7%, respectively). Therefore, for these ions, and perhaps significantly heavier, it does not appear possible to distinguish $Z = \pm 1$. For very heavy ions, $Z = \pm 2$ may be the best possible resolution. More study is needed in these areas, however, before conclusions of that nature can be made.

Suffice to say, the IRIS IC works well within expectations. The coplanar anode design has proven to be extremely effective in both eliminating possible microphonics and giving a very precise energy resolution, which is unprecedented at these pressures. The energy straggling in ^{18}O was small as there was little broadening in the peak. In ^{40}Ar, however, it was more significant, especially when considering that the ADC caused a second peak which was partially indistinguishable from the main, physical peak. Despite the energy straggling and ADC issues, however, ^{40}Ar was still on the order of 7%, which is low enough

to distinguish adjacent isobars. If the ADC problem is to be fixed, the percent energy resolution may be reduced further.

The noise conditions within the IC were low enough to allow for the ^{241}Am alpha particles to be detected in an eight anode configuration, which likely means that any nuclei used for experimental purposes will be above the noise with 16 anodes at 19.5 Torr (and likely 10 Torr as well). Though a few experiments and studies must be carried out to fully understand some of the precise intricacies of the IC, the current design, from the stand point of the knowledge gained from this work, is highly recommended for ionization chambers of this kind. With the IC working as well as it does, the IRIS facility looks to have a bright future, which should in turn lead to a much greater understanding of some of the fundamental principles behind nuclear interactions.

Appendix A

Tables

Table A.1: Energy loss in the IC at 19.5 Torr using LISE++

Beam Species	^{241}Am Alpha		^{18}O		^{40}Ar	
Initial A MeV	1.3715		5.7		7	
Initial Total Energy (MeV)		5.486		102.9168		280
	E Lost (MeV)	E Remaining (MeV)	E Lost (MeV)	E Remaining (MeV)	E Lost (MeV)	E Remaining (MeV)
Entrance Window	0.10062	5.38538	0.51215	102.40465	1.866	278.134
Window - Anode (5.25mm)	0.072815	5.312565	0.35466	102.04999	0.58458	277.54942
Anode 1 (9.5mm)	0.060757	5.251808	0.29366	101.75633	1.0598	276.48962
Anode 1 gap (0.5mm)	0.0032131	5.2485949	0.015473	101.740857	0.055848	276.433772
Anode 2	0.061335	5.1872599	0.29432	101.446537	1.0624	275.371372
Anode 2 gap	0.0032435	5.1840164	0.015508	101.431029	0.055988	275.315384
Anode 3	0.061913	5.1221034	0.29498	101.136049	1.0651	274.250284
Anode 3 gap	0.0032739	5.1188295	0.015542	101.120507	0.056128	274.194156
Anode 4	0.062491	5.0563385	0.29563	100.824877	1.0678	273.126356
Anode 4 gap	0.0033044	5.0530341	0.015577	100.8093	0.056267	273.070089
Anode 5	0.062685	4.9903491	0.29629	100.51301	1.0704	271.999689
Anode 5 gap	0.0032365	4.9871126	0.015611	100.497399	0.056407	271.943282
Anode 6	0.061915	4.9251976	0.29694	100.200459	1.0731	270.870182
Anode 6 gap	0.0032803	4.9219173	0.015646	100.184813	0.056547	270.813635
Anode 7	0.062748	4.8591693	0.2976	99.887213	1.0757	269.737935
Anode 7 gap	0.0033243	4.855845	0.01568	99.871533	0.056688	269.681247
Anode 8	0.063583	4.792262	0.29825	99.573283	1.0783	268.602947
Anode 8 gap	0.0033684	4.7888936	0.015715	99.557568	0.056828	268.546119
Anode 9	0.064422	4.7244716	0.29891	99.258658	1.0811	267.465019
Anode 9 gap	0.0034127	4.7210589	0.015749	99.242909	0.056968	267.408051
Anode 10	0.065264	4.6557949	0.29923	98.943679	1.0836	266.324451
Anode 10 gap	0.0034571	4.6523378	0.015681	98.927998	0.057108	266.267343
Anode 11	0.066066	4.5862718	0.29834	98.629658	1.0864	265.180943
Anode 11 gap	0.0035016	4.5827702	0.015723	98.613935	0.057248	265.123695
Anode 12	0.066911	4.5158592	0.29913	98.314805	1.089	264.034695
Anode 12 gap	0.0035462	4.512313	0.015765	98.29904	0.057388	263.977307
Anode 13	0.067801	4.444512	0.29993	97.99911	1.0917	262.885607
Anode 13 gap	0.0035909	4.4409211	0.015806	97.983304	0.057528	262.828079
Anode 14	0.06865	4.3722711	0.30072	97.682584	1.0944	261.733679
Anode 14 gap	0.0036356	4.3686355	0.015848	97.666736	0.057668	261.676011
Anode 15	0.0695	4.2991355	0.30152	97.365216	1.097	260.579011
Anode 15 gap	0.0036804	4.2954551	0.01589	97.349326	0.057808	260.521203
Anode 16	0.070352	4.2251031	0.30231	97.047016	1.0988	259.422403
Anode - Window	0.086244	4.1388591	0.36697	96.680046	0.60718	258.815223
Exit Window	0.12166	4.0171991	0.53308	96.146966	1.9465	256.868723
Total Energy Loss	1.4688009	26.77362195%	6.769834	6.577967834%	23.131277	8.261170357%

Table A.2: Energy loss in the IC at 10 Torr using LISE++

Beam Species	^{18}O		^{40}Ar	
Initial A MeV	5.7		7	
Initial Total Energy (MeV)		102.9168		280
	E Lost (MeV)	E Remaining (MeV)	E Lost (MeV)	E Remaining (MeV)
Entrance Window	0.51215	102.40465	1.866	278.134
Window - Anode (5.25mm)	0.082524	102.322126	0.29969	277.83431
Anode 1 (9.5mm)	0.14946	102.172666	0.54281	277.2915
Anode 1 gap (0.5mm)	0.0078706	102.1647954	0.028588	277.262912
Anode 2	0.14963	102.0151654	0.54351	276.719402
Anode 2 gap	0.0078796	102.0072858	0.028624	276.690778
Anode 3	0.14979	101.8574958	0.54421	276.146568
Anode 3 gap	0.0078886	101.8496072	0.028661	276.117907
Anode 4	0.14997	101.6996372	0.54491	275.572997
Anode 4 gap	0.0078976	101.6917396	0.028698	275.544299
Anode 5	0.15014	101.5415996	0.54561	274.998689
Anode 5 gap	0.0079066	101.533693	0.028735	274.969954
Anode 6	0.15031	101.383383	0.54631	274.423644
Anode 6 gap	0.0079155	101.3754675	0.028771	274.394873
Anode 7	0.015048	101.3604195	0.54701	273.847863
Anode 7 gap	0.0079168	101.3525027	0.028808	273.819055
Anode 8	0.15051	101.2019927	0.54771	273.271345
Anode 8 gap	0.0079258	101.1940669	0.028845	273.2425
Anode 9	0.15068	101.0433869	0.54841	272.69409
Anode 9 gap	0.0079348	101.0354521	0.028882	272.665208
Anode 10	0.15085	100.8846021	0.54911	272.116098
Anode 10 gap	0.0079438	100.8766583	0.028919	272.087179
Anode 11	0.15102	100.7256383	0.54981	271.537369
Anode 11 gap	0.0079528	100.7176855	0.028956	271.508413
Anode 12	0.15119	100.5664955	0.55051	270.957903
Anode 12 gap	0.0079618	100.5585337	0.028992	270.928911
Anode 13	0.15136	100.4071737	0.55121	270.377701
Anode 13 gap	0.0079707	100.399203	0.029029	270.348672
Anode 14	0.15123	100.247973	0.5519	269.796772
Anode 14 gap	0.0079797	100.2399933	0.029066	269.767706
Anode 15	0.1517	100.0882933	0.5526	269.215106
Anode 15 gap	0.0079887	100.0803046	0.029103	269.186003
Anode 16	0.15187	99.9284346	0.5533	268.632703
Anode - Window	0.083998	99.8444366	0.30606	268.326643
Exit Window	0.52325	99.3211866	1.9128	266.413843
Total Energy Loss	3.5956134	3.493708899%	13.586157	4.852198929%

Table A.3: Selected Gaussian fits and associated parameters

Name	μ	$\Delta\mu$	σ	$\Delta\sigma$	χ^2	NDoF	Reduced χ^2
Sample	650.4	0.1	16.12	0.04	551.4	244	2.259836066
Poor Fit	640.6	0.2	30.93	0.13	6.92E+04	700	98.82857143
Coplanar Extreme	666.3	0.5	16.04	0.26	28.11	32	0.8784375
Pulser Noise	1483	0	2.482	0.009	15.74	18	0.874444444
Alpha Source Lost in Noise	27.29	0.13	3.638	0.084	21.01	8	2.62625
Added Anodes - 40Ar (4)	2443	0.1	69.02	0.1	3154	853	3.697538101
Added Anodes - 18O (1)	674.6	0	16.46	0.03	1457	297	4.905723906
Field Cage Bias - 40Ar (-400)	2140	0.1	63.78	0.09	4427	620	7.140322581
Field Cage Bias - 40Ar (-500)	2128	0.2	63.11	0.11	964.3	387	2.491731266
Field Cage Bias - 40Ar (-600)	202	0.1	66.56	0.09	3674	694	5.293948127
Field Cage Bias - 18O (-400)	679.1	0	16.36	0.03	993.3	221	4.494570136
Field Cage Bias - 18O (-500)	696.6	0	16.46	0.03	1198	265	4.520754717
Field Cage Bias - 18O (-600)	698.2	0	16.7	0	926.7	243	3.813580247
CA - 18O, FC = -250V, P = 10T	342.1	0	11.73	0.02	1717	195	8.805128205

Appendix B

Select glossary

1. θ - The polar angle of a scattered particle in a spherical coordinate system.

2. ϕ - The azimuthal angle of a scattered particle in a spherical coordinate system.

3. A(b,c)D reaction - A reaction in which particle A collides with target b to produce the reaction products c and D. For example the stripping ^{11}Li(p,d)^{10}Li reaction is such that a ^{11}Li nucleus collides with a proton, which strips off a neutron from ^{11}Li to produce a deuteron and ^{10}Li.

4. ADC - Analog to digital converter.

5. ADC gate - The electronic "gate" that opens under certain trigger conditions. Once this gate is open, the ADC will process signals within it.

6. ^{241}Am - Americium-241. The radioactive isotope of americium used to produce the 5.487 MeV alpha source for offline testing in this work.

7. ^{40}Ar - Argon-40. The stable isotope of argon, containing 18 protons and 22 neutrons, which was used as one the stable beams in this work.

8. CA - Coplanar anode. The negatively biased focal plane used to get force ionized electrons onto the anode strip. For more information see section 2.3.4.2.

9. CsI(Tl) - Thallium doped cesium iodide that was the inorganic scintillator crystal used for detecting the energy of the light charge particle reaction products.

10. DAQ - Data acquisition system. The last stage in signal processing wherein the final digitized signal is acquired and stored.

11. E/P - Electric field divided by pressure. The ratio of electric field to gas pressure in a gas chamber.

12. $E - \Delta E$ - Two annular detectors, one of which is a silicon detector (ΔE), and the other a CsI scintillator detector (E). These detector system is used to measure scattering angle and energy of the light reaction products in IRIS.

13. FC - Field cage. The part of the IC responsible for creating the electric field gradient that accelerates the electrons toward the anode pads. For more information see section 2.3.4.1.

14. FC/C - The ratio of the field cage bias voltage to the coplanar bias voltage. This ratio is used for a number of measurements. For more information see section 4.6.

15. FWHM - Full width at half maximum. The number that represents the width of a curve (on the abscissa) at half its maximum height (on the ordinate).

16. G10 - Also known as Fiberglass Micarta or Garolite, G10 is a high quality insulator used mainly for separating electrical components.

17. GARFIELD - A drift chamber simulation program developed by CERN.

18. IC - Ionization chamber. A gas-filled detector used for a myriad of applications in nuclear and particle physics. IRIS uses an IC for particle identification. For more information see sections 1.3 and 2.3.

19. IRIS - The ISAC charged particle reaction spectroscopy station. A new experimental facility in the ISAC II hall at TRIUMF.

20. IRIS IC - The ionization chamber used on IRIS for isobaric tagging of particles in the beam before they reach the reaction target.

21. ISAC - Isotope Separator and ACcelerator. Part of the rare isotope division at TRIUMF, ISAC houses several experimental facilities. ISAC consists of the ISAC-I and ISAC-II accelerator sections and associated experimental stations.

22. ISAC-II - The superconducting linear accelerator for re-accelerating the ISOL beam (together with the associated various experimental beamlines in the experimental hall). Here, among others, the IRIS facility is housed.

23. LISE++ - A program for performing simulations and calculations of various aspects nuclear and particle physics experiments. Developed by O. B. Tarasov and D. Bazin.

24. MBq - Mega Becquerel. A Becquerel is an SI unit defined as one nucleus decay per second.

25. Mylar - Biaxially-oriented polyethylene terephthalate or BoPET is a polyester film used in many nuclear physics applications. It often goes by its well-known trade names: Mylar or Melinex. It was used as the material for the entrance and exit windows of the IRIS IC in this work.

26. N - Neutron number. The number of neutrons in an atomic nucleus.

27. n - The number of ionizable atoms in the IC. This varies as a function of pressure based on $PV = nRT$.

28. N/Z - The ratio of neutrons to protons in the nucleus of an atom. For example, ^{18}O has a value of N=10 and Z=8, therefore N/Z=1.25

29. ^{18}O - Oxygen-18. The stable isotope of oxygen used as one of the stable beams in this work.

30. Q - The charge of a particular atom. Equal to the number of protons it has when fully stripped.

31. Q value - The amount of energy released or absorbed in a reaction. $Q = E(\text{reactants}) - E(\text{products})$.

32. ROOT - A programming language developed by CERN specifically for nuclear and particle physics applications. It is an object oriented language based off C++.

33. S3 - Model name of the silicon detector used in IRIS to detect the heavy reaction products..

34. Shaping amplifier - An amplifier used for signal processing (in the case of the IRIS IC it comes directly after the preamplifiers), which both amplifies the voltage of the signal and shapes it into a semi-Gaussian.

35. SHT - Solid hydrogen target.

36. Si_3Ni_4 - Silicon nitride. Due its crystalline structure, silicon nitride is ideal for applications that require high strength with small amounts. Plans are in place to use Si_3Ni_4 entrance and exit windows at 30 nm or 50 nm on the IRIS IC to replace the Mylar windows currently in use.

37. SRIM - The Stopping and Range of Ions in Matter. A program that calculates the interaction of a particle beam through various materials. Developed by James F. Ziegler.

38. SSB - Silicon Surface Barrier detector. Used on the IRIS IC for offline testing with alpha particles.

39. Transverse diffusion - The random movement of ionized electrons from an area of high concentration to one of low concentration. In the IRIS IC, this is aided by the field cage in order to force the electrons in a particular direction.

40. Transverse diffusion versus E/P curve - The plot showing the effects of a changing electric field on the transverse diffusion of electrons in an ionizable medium at varying pressures. Isobutane shows a broad minimum in this curve, meaning that increasing the electric field above a point does little to affect the transverse diffusion.

41. TRIUMF - Tri-University Meson Facility. Canada's national nuclear and particle physics laboratory, which is housed in Vancouver, British Columbia. It is home the world largest cyclotron at 500 MeV. This work was conducted in the ISAC-II experimental hall at TRIUMF.

42. XA MeV - X MeV per nucleon. TRIUMF uses this as a measurement of the total kinetic energy of the ions it accelerates. For example, ^{18}O at 5.7A MeV, with its 18 nucleons, has a total of $5.7 \times 18 = 102.6$ MeV.

43. YY1 - Model name of the silicon detector used in IRIS for detecting the light target-like reaction products. Eight YY1 detectors combine to create the annular ΔE detector.

44. Z - The number of protons in a nuclide.

Bibliography

Alejandro Sonzogni, B. N. L. 2013, Chart of Nuclides, http://www.nndc.bnl.gov/chart/

Bazin, D., Benenson, W., Brown, B., et al. 1998, Physical Review C, 57, 2156

Becquerel, H. 1901, Nature, 63, 396

Casten, R. & Sherrill, B. M. 2000, Progress in Particle and Nuclear Physics, 45, S171

CERN. 2010, GARFIELD, http://garfield.web.cern.ch/garfield/

CREMAT. 2013, Charge sensitive preamplifiers, http://www.cremat.com/

Dobrovolsky, A., Alkhazov, G., Andronenko, M., et al. 2006, Nuclear Physics A, 766, 1

Dunlap, R. A. 2004, An introduction to the physics of nuclei and particles (Thomson Brooks/Cole)

Frisch, O. 1944, BR-49, 65

Gumplinger, P. 2013, private communication

Hagen, G., Hjorth-Jensen, M., Jansen, G., Machleidt, R., & Papenbrock, T. 2012, Physical Review Letters, 108, 242501

Heyde, K. 2004, Basic ideas and concepts in nuclear physics: an introductory approach (Taylor & Francis)

Kanungo, R. 2004, Nuclear Physics A, 734, 337

Kanungo, R., Nociforo, C., Prochazka, A., et al. 2009, Physical review letters, 102, 152501

Knoll, G. F. 2010, Radiation Detection and Measurement (Wiley)

Lagoyannis, A., Auger, F., Musumarra, A., et al. 2001, Physics Letters B, 518, 27

Mesytec. 2013a, MADC-32 anolog to digital converter, http://www.mesytec.com/datasheets/MADC-32.pdf

Mesytec. 2013b, MSCF-16 shaping amplifier, http://www.mesytec.com/mscf.html

Price, W. J. & Price, W. J. 1964, Nuclear radiation detection, Vol. 126 (McGraw-Hill New York)

Rossi, B. B. & Staub, H. H. 1949, Ionization chambers and counters: experimental techniques (McGraw-Hill New Yew)

Rutherford, E. 1911, Phil. Mag, 21, 1911

Satchler, G. R. 1983, Direct nuclear reactions (Clarendon press Oxford)

Sheffer, G. 2013, private communication

Sherrill, B. & Morrissey, D. 2004, The Euroschool Lectures on Physics with Exotic Beams, Vol. I Lecture Notes in Physics (Springer)

Shultz, G. 1976, Thesis (Universite de Strasbourg)

Tanihata, I. 1996, Journal of Physics G: Nuclear and Particle Physics, 22, 157

Tanihata, I. 2001, Nuclear Physics A, 682, 114

Tanihata, I., Hamagaki, H., Hashimoto, O., et al. 1985, Physical Review Letters, 55, 2676

Tarasov, O. & Bazin, D. 2008, Nuclear Instruments and Methods in Physics Research Section B: Beam Interactions with Materials and Atoms, 266, 4657

Veselsky, M. & Souliotis, G. 2011, Nuclear Physics A, 872, 1

Wilkinson, D. H. 1950, Ionization chambers and counters (University Press Cambridge)

Ziegler, J. 2013, SRIM, http://www.srim.org/